

1

2

3

4

# Search for supersymmetry in pp collisions with all-hadronic final states using the $\alpha_T$ variable with the CMS detector at the LHC

5

6

Bryn Mathias  
Imperial College London

7

Supervisor: Dr Alex Tapper

**Abstract**

1

2

This is a thesis.

DRAFT

# Declaration

There are many like it.

Author

## Preface

<sup>1</sup>

<sup>2</sup>

Something witty.

DRAFT

## Acknowledgements

<sup>1</sup>

<sup>2</sup>

Thanks.

# Contents

2	<b>1</b>	<b>Introduction</b>	9
3	<b>2</b>	<b>Theory</b>	10
4	2.1	The Constrained Minimal Super Symmetric Model	10
5	<b>3</b>	<b>The CMS detector</b>	11
6	3.1	The Silicon Tracker	12
7	3.2	The Electromagnetic Calorimeter (ECAL)	13
8	3.3	The Hadronic Calorimeter (HCAL)	14
9	3.4	The The Compact Muon Solenoid (C.M.S) Super-Conducting Solenoid	16
10	3.5	The C.M.S Muon system.	16
11	3.6	The Level One Trigger System.	17
12	3.7	The High Level Trigger System.	18
13	<b>4</b>	<b>Level One Calorimeter Trigger</b>	19
14	4.1	Level-1 Trigger Jet Algorithm [34]	20
15	4.2	Level-1 Trigger Performance	22
16	4.3	Level-1 Trigger Pile-up Mitigation	30
17	4.3.1	Effect on trigger efficiency	32
18	4.3.2	Summary	34
19	<b>5</b>	<b>Motivating the <math>\alpha_T</math> Analysis</b>	36
20	5.1	The Problem	36
21	<b>6</b>	<b>Reconstruction and Event selection</b>	38
22	6.1	The $\alpha_T$ variable.	38
23	6.2	Event selection	39
24	6.2.1	Preselection of hadronic objects	40
25	6.2.2	Electrons	42
26	6.2.3	Muons	42

1	6.2.4	Photons . . . . .	44
2	6.3	Common Analysis cuts . . . . .	44
3	6.4	High Level triggers for the $\alpha_T$ analysis . . . . .	47
4	6.4.1	Trigger efficiency measurement . . . . .	48
5	6.5	Extension to higher analysis dimensions. B-tagging . . . . .	53
6	<b>7</b>	<b>Background Prediction</b>	<b>61</b>
7	7.1	Electro-Weak Background Prediciton . . . . .	61
8	7.2	Estimating the residual QCD background component.[6] . . . . .	69
9	7.3	Systematic uncertainties on the electro-weak background model. . . . .	71
10	7.3.1	Motivating the combined systematic on the translation factors . . . . .	74
11	7.4	Likelihood model . . . . .	74
12	7.5	Final Results . . . . .	78
13	<b>8</b>	<b>Interpretation</b>	<b>84</b>
14	8.1	Signal Models . . . . .	84
15	8.2	Signal Efficiency . . . . .	85
16	8.2.1	Constrained Minimal SuperSymmetric Model (CMSSM) . . . . .	85
17	8.2.2	Simplified Models . . . . .	85
18	8.3	Uncertainty on Signal Efficiency . . . . .	86
19	8.4	Choice of Parton Density Function (PDF) set at generator level. . . . .	87
20	8.5	Effects of Jet Energy Scale Variations on Signal Efficiency . . . . .	89
21	8.6	Systematic Uncertainty on Signal Yield from Cleaning Filters and Object Vetoess . . . . .	89
22	8.7	Interpretation in terms of new physics models. . . . .	90
24	<b>9</b>	<b>Conclusion</b>	<b>95</b>
25	<b>Bibliography</b>		<b>96</b>
26	1	Additional information on triggers . . . . .	100
27	2	Addition information on background estimation methods . . . . .	104
28	2.1	Determination of $k_{QCD}$ . . . . .	104
29	3	Closure tests and systematic uncertainties . . . . .	105
30	3.1	Defining muon samples without an $\alpha_T$ requirement . . . . .	105
31	3.2	Closure tests for inclusive analysis . . . . .	106
32	3.3	Closure tests for b-tag analysis . . . . .	107
33	3.4	Closure tests concerning pile-up . . . . .	109

---

1	4	Signal efficiency . . . . .	110
2	4.1	CMSSM . . . . .	110
3	4.2	T1 . . . . .	111
4	4.3	T2 . . . . .	112
5	4.4	T2tt . . . . .	113
6	4.5	T2bb . . . . .	114
7	4.6	T1tttt . . . . .	115
8	4.7	T1bbbb . . . . .	116
9	4.8	Signal contamination for T1tttt . . . . .	117
10	5	Experimental systematic uncertainties on signal efficiency times acceptance	118
11	5.1	Systematics due to jet energy scale uncertainties . . . . .	118
12	5.2	Systematics due to the MHT/MET cut . . . . .	123
13	5.3	Systematics due to the dead ECAL cut . . . . .	127
14	5.4	Systematics due to the lepton and photon vetoes . . . . .	128
15			

# Chapter 1

## <sup>1</sup> Introduction

<sup>2</sup> **The accelerator and detectors** The Large Hadron Collider (LHC) [14] is a proton-  
<sup>3</sup> proton collider which is situated in the Large Electron Positron (LEP) tunnel approxi-  
<sup>4</sup> mately 100 m under the franco-swiss border. Design center of mass energy is 14 TeV  
<sup>5</sup> with an instantaneous luminosity of  $1 \times 10^{34} \text{ cm}^{-2} \text{s}^{-1}$ . However during 2011 the center of  
<sup>6</sup> mass energy was 7 TeV and the maximum luminosity was  $5 \times 10^{33} \text{ cm}^{-2} \text{s}^{-1}$ . To achieve  
<sup>7</sup> this high energy and high beam current the LHC uses superconducting niobium-titanium  
<sup>8</sup> magnets, cooled to a temperature of 1.8 Kelvin, that produce a maximum field strength  
<sup>9</sup> of 8.36 Tesla.

<sup>10</sup> we might well need some more stuff about the LHC its self in here!

<sup>11</sup> Situated around the LHC ring are four detectors, two general detectors ATLAS [10]  
<sup>12</sup> and CMS (see Chapter 3 for a detailed discussion of the CMS detector) [27][44] which  
<sup>13</sup> are designed to measure the Standard Model (S.M) to high precision and search for new  
<sup>14</sup> physics. The LHC beauty experiment [37] is designed to study at previously unattainable  
<sup>15</sup> precision the decays of heavy quark flavors, both to measure the S.M couplings and to  
<sup>16</sup> search for beyond the S.M (BSM) physical processes. Finally the ALICE [11] experiment  
<sup>17</sup> is designed to run when the LHC is running in it's secondary mode where rather than  
<sup>18</sup> proton bunches, lead ions are collided, in an effort to study the quark-gluon plasma.

<sup>19</sup> **New physics** Whilst the theory of the S.M and of new physics models will be discussed  
<sup>20</sup> in chapter 2 it is prudent to discuss the observable features of these models with regard  
<sup>21</sup> to design requirements for the general purpose detectors.

# Chapter 2

## <sup>1</sup> Theory

### <sup>2</sup> 2.1 The Constrained Minimal Super Symmetric <sup>3</sup> Model

# Chapter 3

## 1 The CMS detector

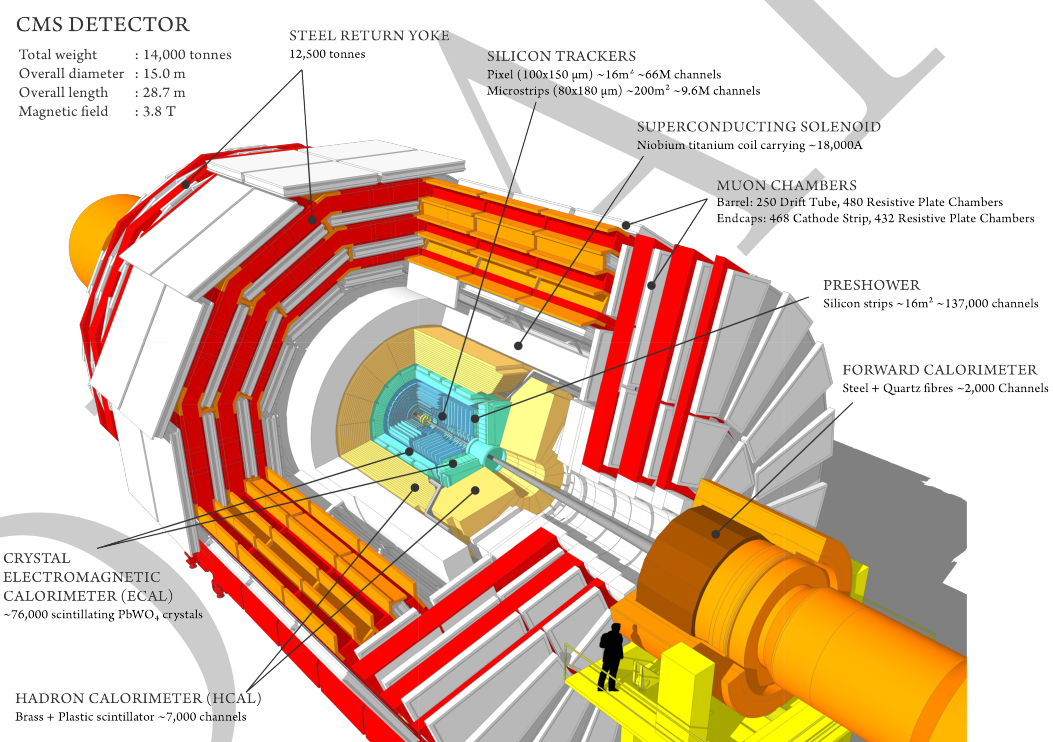
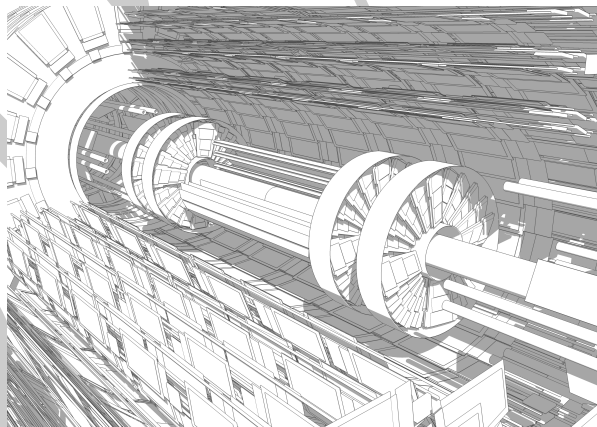


Figure 3.1: A perspective view of the C.M.S detector[1].

2 The C.M.S detector was designed and built to study proton-proton interactions at  
3 the Large Hadron Collider (L.H.C) with the aim of discovering the Higgs boson and  
4 searching for beyond the standard model physics signals. The detector is constructed  
5 in a traditional onion layer design with high precision tracking detectors nearest the  
6 interaction point and high energy resolution calorimetric detectors in the outer layers.  
7 Due to the predicted presence of missing energy  $\cancel{E}_T$  in new physics models, energy  
8 measurement over the full  $\eta$  range is required. As allured to in the name the possibilities

1 of the new physics models containing muons and the clean Higgs decay  $H \rightarrow ZZ \rightarrow \mu\mu\mu\mu$ ,  
 2 the detector was built with accurately reconstructing muons with  $p_T$  of 1 TeV, due to  
 3 the prevalence of lepton signals and the ability to distinguish these leptons from the large  
 4 amount of hadronic fragmentation caused by smashing two protons together at a centre  
 5 of mass energy of 14 TeV the C.M.S Electromagnetic calorimeter was also designed to  
 6 have precise energy measurement and fine grain spatial resolution, this design feature  
 7 was also necessitated by the Higgs decay channel  $H \rightarrow \gamma\gamma$ . The other new feature of  
 8 C.M.S is the use silicon detectors through out for particle tracking these give precise  
 9 track reconstruction abilities and the associated fine grain resolution in both position and  
 10 momentum. All the sub-detectors save the muon system are contained with in the barrel  
 11 of a 4 T superconducting solenoid. This magnet provides the particle track bending  
 12 required for momentum and lepton charge measurement. In this section the key detector  
 13 elements and their design parameters are discussed in Section 6 the construction of offline  
 14 physics objects is discussed.

### 15 3.1 The Silicon Tracker



**Figure 3.2:** The C.M.S tracking system, pixel detectors are situated at the centre of the detector closest to the interaction point, surrounded by layers of silicon strip detectors[1].

16 The design goal for the C.M.S tracking system was to produce a system that can  
 17 precisely and efficiently measure the trajectories of charged particles produced in L.H.C  
 18 collisions. The tracking system surrounds the collision point and has a length of 5.8 m  
 19 and a diameter of 2.5 m. At full the instantaneous L.H.C luminosity of  $10^{34} \text{ cm}^{-2} \text{ s}^{-1}$  an  
 20 average of 1000 charged particles from more than 20 proton-proton interactions will be

1 produced per 25 ns bunch crossing. This imposes the requirements of high granularity  
2 so that the individual particles and their trajectories can be distinguished and a fast  
3 response so that the hits can be assigned to the correct bunch crossing. The technical  
4 implications of these requirements imply both a large amount of on-detector electronics  
5 and their associated cooling equipment. This large amount of tracker material increases  
6 the multiple scattering, bremsstrahlung, photon conversion and nuclear interactions of  
7 the particles which are traversing the tracking system, this in turn limits the position  
8 and energy resolution of the calorimeter systems. A compromise between the material  
9 budget of the tracking system, the desired features and the requirement for the tracking  
10 system to have an expected life time of 10 years in a high radiation environment, this  
11 was to construct the tracking system using only solid state silicon detector technology.

12 The C.M.S tracking system is formed of a pixel detector with three layers situated  
13 between 4.4 cm and 10.2 cm of the interaction point and a silicon strip tracker with 10  
14 barrel layers extending outwards to a radius of 1.1 m from the interaction point. The  
15 barrel layers of both the pixel and strip detectors are complimented by layers of either  
16 pixel or strip disks which extend the acceptance of the tracker to  $|\eta| < 2.5$ . The resulting  
17 structure is that of a detector with  $200 \text{ m}^2$  of active silicon which makes the C.M.S  
18 tracker the largest detector of it's type ever constructed.

19 The individual pixels that comprise the pixel detector are  $100 \times 150 \mu\text{m}^2$  which  
20 corresponds to an occupancy of around  $10^{-4}$  per bunch crossing. The detector cell size  
21 for the Microstrip detectors at a radius between 20-55 cm is  $10 \text{ cm} \times 180 \mu\text{m}$  which leads  
22 to an average occupancy of 2-3%, further out the minimum cell size is increased to  $25 \text{ cm}$   
23  $\times 180 \mu\text{m}$  with an occupancy of around 1%. The tracker performance is extensively  
24 documented in [29].

## 25 **3.2 The Electromagnetic Calorimeter (ECAL).**

26 The C.M.S electromagnetic calorimeter is a hermetic homogeneous calorimeter con-  
27 structed from lead tungstate ( $\text{PbWO}_4$ ) crystals. The ECAL is split into two parts, a  
28 barrel covering  $|\eta| < 1.479$  read out by avalanche photodiodes and the two end-caps  
29 covering  $1.479 < |\eta| < 3.0$ , read out by vacuum photo-triodes.

30 Lead tungstate crystals were chosen because of their short radiation length  $X_0 =$   
31  $0.89 \text{ cm}$ , fast scintillation and radiation hardness. During the research and development

<sup>1</sup> program it was shown that radiation damage does not affect the scintillation method or  
<sup>2</sup> the uniformity of the emitted light yield along the crystal, it only effects the transparency  
<sup>3</sup> through the creation of colour centres. This will be monitored throughout the lifetime of  
<sup>4</sup> the ECAL via a light injection system[39].

<sup>5</sup> The barrel crystals have a front face of  $22 \times 22 \text{ mm}^2$ , this corresponds to the Moliere  
<sup>6</sup> radius of  $\approx 22 \text{ mm}$ ; with a length of 230 mm giving a each crystal length of  $25.8X_0$  where  
<sup>7</sup>  $X_0$  is amount of material required for 68% of an electromagnetically interacting particle's  
<sup>8</sup> energy to be radiated in the form of bremsstrahlung or pair production whilst traversing  
<sup>9</sup> that material. They are arranged in 36 super-modules, forming two half barrels. The  
<sup>10</sup> crystal axes are skewed at  $3^\circ$  with respect to the vertex and each covers  $1^\circ$  in  $\phi$  &  $\eta$

<sup>11</sup> The End cap crystals are arranged in two semi-circular ‘Dees’, groups of  $5 \times 5$  crystals  
<sup>12</sup> are canter-levered on a aluminium backing plate. The crystals are again skewed with  
<sup>13</sup> regard to the interaction vertex, however they are arranged in an  $x - y$  grid rather than  
<sup>14</sup> a  $\phi - \eta$  grid. The crystal dimensions are different to the barrel, in that the cross section  
<sup>15</sup> is  $28.6 \times 28.6 \text{ mm}^2$ , with a length of 220 mm corresponding to 24.7 radiation lengths

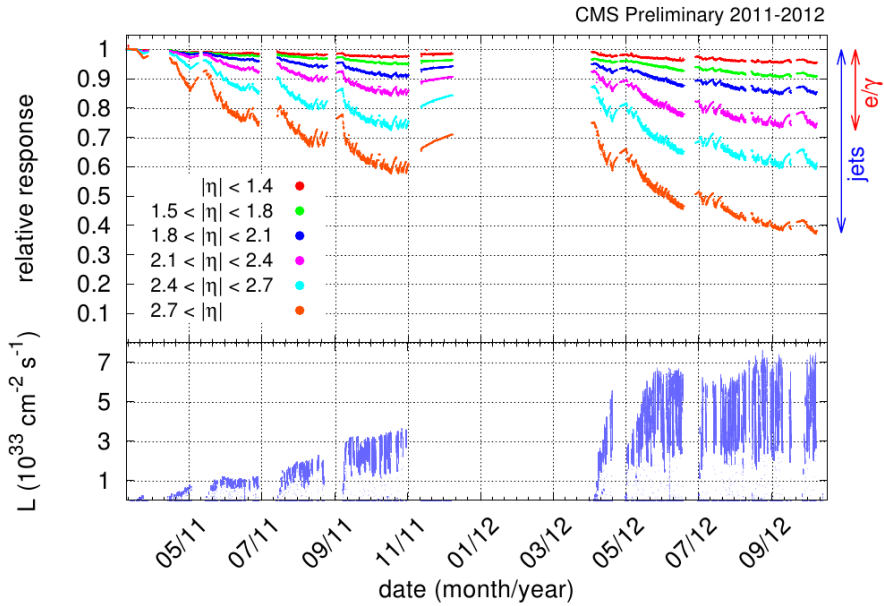
<sup>16</sup> The crystals are read out with avalanche photo-diodes in the barrel region which  
<sup>17</sup> covers  $|\eta| < 1.479$  and with vacuum photo-triodes in the end cap region which covers  
<sup>18</sup>  $1.479 < |\eta| < 3.0$ .

<sup>19</sup> In addition to the ECAL there is a pre-shower detector situated at  $1.653 < |\eta| < 2.6$ ,  
<sup>20</sup> this provides identification of elections against minimum ionising particles and improves  
<sup>21</sup> the position measurement of electrons and photons in the ECAL endcaps.

<sup>22</sup> Figure 3.3 shows the change in response of the ECAL during running, due to the  
<sup>23</sup> formation of colour centres, this response is measured using laser light at 440 nm and is  
<sup>24</sup> used to correct the energies recorded in data during each run to form a uniform response.

### <sup>25</sup> 3.3 The Hadronic Calorimeter (HCAL).

<sup>26</sup> The design of the C.M.S HCAL is constrained by the size requirements of fitting the  
<sup>27</sup> tracking system, ECAL and HCAL inside the solenoid magnet. The HCAL is situated  
<sup>28</sup> between the ECAL which ends at a radius of 1.77 m and the solenoid which starts at a  
<sup>29</sup> radius of 2.95 m. This constraint limits the amount of material which can be put in place  
<sup>30</sup> to fully contain the hadronic showers. To overcome this an outer lay of instrumentation  
<sup>31</sup> is placed outside of the magnet and cryogenic system to catch the hadronic tails. The full



**Figure 3.3:** Relative response to laser light (440 nm) measured by the ECAL laser monitoring system, averaged over all crystals in bins of pseudo-rapidity, for the 2011 and 2012 data taking periods. The response change observed in the ECAL channels is of the order of a few percent in the barrel, while it reaches up to 25% in the most forward endcap regions used for electron and photon reconstruction. The response change is up to 60% in channels closest to the beam pipe. These measurements are used to correct the physics data.  
The bottom plot shows the instantaneous LHC luminosity delivered during this time period.[7]

1 containment of the hadronic objects is necessary for precise missing energy measurement,  
 2 which is a key discriminatory feature for new physics models with undetectable final  
 3 state particles.

4 The hadronic calorimeter is split in to three sub detectors, the hadronic barrel (HB)  
 5  $|\eta| < 1.3$ , hadronic endcaps (HE)  $1.3 < |\eta| < 3.0$  and a forward calorimeter (HF)  
 6  $3.0 < |\eta| < 5.5$ .

7 The HB and HE are comprised of layered tiles of brass absorber plates interspaced  
 8 with scintillator plates which are read out by wave length shifting fibres. The total  
 9 absorber thickness varies between 5.2 and 10.6 interaction lengths, the ECAL adds  
 10 approximately one extra interaction length. The scintillators are segmented in to towers  
 11 of area  $\Delta\eta \times \Delta\phi = 0.087 \times 0.087$  in the barrel and  $\Delta\eta \times \Delta\phi = 0.17 \times 0.17$  in the end  
 12 caps. The light produced and in the scintillators is merged in the wavelength shifting  
 13 fibres and then read out using hybrid photo-diodes. The HF is constructed from radiation

1 hard quartz fibres, this enables the detector to survive in the very forward regions of the  
2 detector where unprecedented levels of radiation are experienced.

3 The hadronic outer (HO) which is situated outside the solenoid used the solenoid  
4 coils as an extra absorber adding extra interaction lengths in the barrel region ensuring  
5 full containment of hadronic showers. The HO is constructed from layers of scintillator  
6 tiles, the light from which is then merged in the wavelength shifting fibres and read out  
7 using hybrid photo-diodes.

### 8 **3.4 The C.M.S Super-Conducting Solenoid**

9 The requirement for precise muon momentum measurements for muons with  $p_T > 1$  TeV  
10 infers the requirement of large bending power, this requirement forces the choice of a  
11 superconducting magnet. The C.M.S magnet is 13 m long, has an inner diameter of 6 m  
12 and provides a 4 T magnetic field, which gives a bending power of 12 Tm before the muon  
13 bending angle is measured by the muon system. The bore of the solenoid contains the  
14 tracking and calorimeter systems. The magnet is constructed from Niobium-Titanium  
15 superconductor embedded in an aluminium stabiliser is coiled in four layers resulting in  
16 220 t of cold mass. This is then cooled to around 4 K using liquid helium and a current  
17 of  $\approx 20$  kA is applied to generate the magnetic field.

### 18 **3.5 The C.M.S Muon system.**

19 The C.M.S muon system is designed to provide accurate muon  $p_T$  measurements  
20 ( $\sqrt{p_T}/p_T < 0.1$ ) for muons over a large  $p_T$  range. Due to the cylindrical nature of  
21 the solenoid, the muon system is also designed to be cylindrical. The muon system has  
22 three purposes the first is the identification of muons, secondly the momentum measure-  
23 ment of these muons and thirdly to provide information to the trigger system. The muon  
24 system uses three types of gaseous detectors for particle tracking and identification, in  
25 the barrel region where the magnetic field is uniform, drift chambers (DT) are used, these  
26 cover the region  $|\eta| < 1.2$  and are interspaced between the layers of the magnetic flux  
27 return plates. In the end cap regions where the muon and background rates are higher  
28 and the magnetic field is non-uniform, cathode strip chambers (CSC) are used due  
29 to their fast response, radiation hardness and fine grain segmentation, the CSC's cover

<sup>1</sup>  $0.9 < |\eta| < 2.4$ . Due to the initial uncertainty on the background rates and the 25 ns  
<sup>2</sup> bunch crossing intervals expected when the L.H.C is running under design conditions a  
<sup>3</sup> complementary dedicated muon triggering system consisting of resistive plate chambers  
<sup>4</sup> (RCP) was added in the range  $|\eta| < 1.6$ , the RCPs provide a fast, independent and fine  
<sup>5</sup> grain system for which to trigger on muon objects in the harshest of running conditions.

<sup>6</sup> Due to multiple scattering and the shear quantity of detector material before the first  
<sup>7</sup> muon station momentum measurement using the muon system only is accurate to a level  
<sup>8</sup> of  $\approx 10\%$  below 200 GeV and accurate to a level of 15 – 40%,  $|\eta|$  dependant for 1 TeV  
<sup>9</sup> muons, when including the tracker information in the muon momentum measurement  
<sup>10</sup> the resolution is improved to  $\approx 1\%$  below 200 GeV and to about 5% for 1 TeV muons.

### <sup>11</sup> 3.6 The Level One Trigger System.

<sup>12</sup> The C.M.S trigger system is designed in two levels, the first, the Level-1 trigger is built  
<sup>13</sup> using custom electronics and is designed to reduce the input rate of 40 million events  
<sup>14</sup> per second to a manageable rate of 100 thousand events per second. Information from  
<sup>15</sup> the calorimeter and muon systems only are considered as the time required to read out  
<sup>16</sup> the tracking information is prohibitive at this level. Two separate trigger systems, one  
<sup>17</sup> performing triggering on the calorimeter system, the other performing triggering on  
<sup>18</sup> the muon systems are employed. For a detailed discussion of the calorimeter triggering  
<sup>19</sup> algorithms and their performance see Chapter 4. The information from these two sub  
<sup>20</sup> triggers is passed to the global trigger, where the decision to accept the event or not  
<sup>21</sup> is made. The muon trigger considers information from each of the DT, CSC and RCP  
<sup>22</sup> muon systems. Tracks are created from the hits in each of the sub systems and fitted,  
<sup>23</sup> the muon momentum is then calculated from the radius of curvature of these muons,  
<sup>24</sup> the four highest  $p_T$  muon candidates are then passed to the global trigger. Electron and  
<sup>25</sup> photon candidates are created by the regional calorimeter trigger, which is in turn read  
<sup>26</sup> out by the global calorimeter trigger (GCT), the GCT creates jet candidates, energy and  
<sup>27</sup> missing energy sums, the four highest  $E_T$  jet candidates of each type (central, tau and  
<sup>28</sup> forward), the energy sums and the electron/photon candidates are then passed to the  
<sup>29</sup> global trigger where the final trigger decisions are made. These decisions can require  
<sup>30</sup> information from a single detector or can require cross objects such as the requirement  
<sup>31</sup> of an energy sum value and a muon.

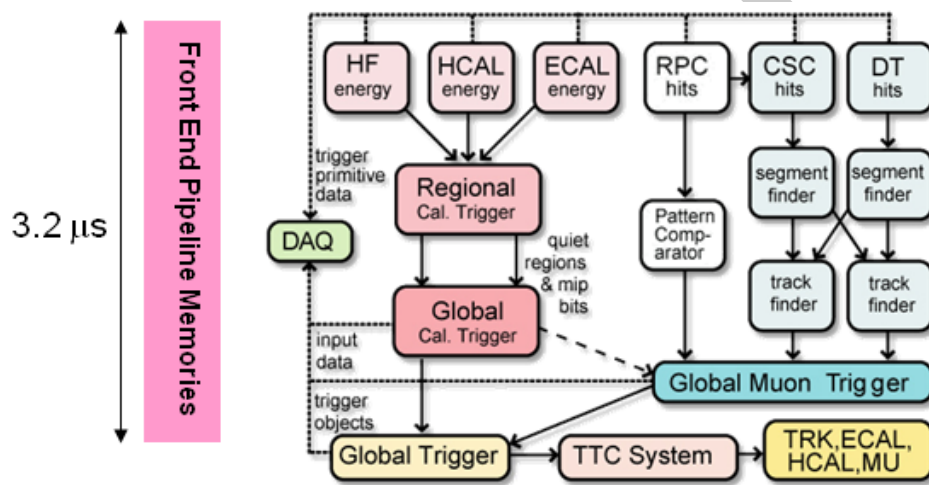
## **3.7 The High Level Trigger System.**

The high level trigger system is constructed from off the shelf components. The system is composed of two sets of machines, the first are the Event Builder (EB) units, these build raw data in to regional chunks from the data read out at the front end of the detector when a Level-1 accept is received, this is then combined and transmitted to the event filter cluster. The EB units transfer the data to the Event Filter (EF) units via a standard TCP/IP gigabit ethernet link. The task of the HLT EF units is to run complex reconstruction algorithms using combined detector information to reduce the data rate accepted by the Level-1 trigger to a manageable rate, the original design anticipated an output rate of 100 events per second, however in 2012 running 1000 events per second were stored, half of this rate was assigned to the prompt reconstruction work flow, the other half was stored for reconstruction during the long shut down of the L.H.C in 2013-2015.

The EF farm is formed from standard rack-mounted pc units with a total of approximately 1000 computing cores operating at a clock frequency of around 2 GHz. Upon receiving an event, each unit performs the C.M.S reconstruction, the same software is used as for offline analysis meaning that the objects used for trigger decisions are as close in performance to the offline objects as possible, this increases the over all trigger efficiency. Trigger chains are designed so that full event reconstruction can be performed, however when constructing a trigger that requires full tracking reconstruction steps are made so that if a given requirement is failed at a lower stage of the reconstruction then time is not wasted performing the full reconstruction. The EF farm is connected to a large (several hundred terabyte) storage area net work, this acts as a temporary storage area for the events accepted by the HLT before the events are transferred to the tier-zero reconstruction farm which is located at the central CERN site.

# Chapter 4

## <sup>1</sup> Level One Calorimeter Trigger



**Figure 4.1:** The CMS Level-1 Trigger system.

<sup>2</sup> The CMS Level-1 trigger system[20] is a pipelined dead-timeless system based on  
<sup>3</sup> custom-built electronics. The Level-1 trigger is a combination of several sub systems,  
<sup>4</sup> which are interconnected as depicted in Figure 4.1.

<sup>5</sup> Coarse grain information from the electro-magnetic, hadronic and forward calorimeters  
<sup>6</sup> is processed by the Regional Calorimeter Trigger (RCT), this is then passed to the Global  
<sup>7</sup> Calorimeter Trigger (GCT) where the coarse grain information is clustered into physics  
<sup>8</sup> objects, these objects are then passed to the Global Trigger where the Level-1 accept  
<sup>9</sup> decision is made. Due to the limited size of the pipe line this Level-1 accept must be  
<sup>10</sup> issued within  $4.0 \mu\text{s}$ .

<sup>1</sup> The objects passed from the GCT to the GT include electro-magnetic objects, both  
<sup>2</sup> electrons and photons as due to the lack of tracking information at the Level-1 trigger  
<sup>3</sup> these objects are indistinguishable, jets and energy sums.

<sup>4</sup> The RCT generates up to 72 isolated and non-isolated electro-magnetic objects, these  
<sup>5</sup> are sorted by rank, which is equivalent to transverse energy  $E_T$ . The four highest ranked  
<sup>6</sup> electro-magnetic objects are then passed via the GCT to the GT at an equivalent data  
<sup>7</sup> rate of  $29 \text{ Gbs}^{-1}$  per type.

<sup>8</sup> Hadronic objects undergo two clustering steps. First the transverse energy sums of  
<sup>9</sup> the ECAL and corresponding HCAL towers are calculated, the towers are then summed  
<sup>10</sup> in to  $4 \times 4$  trigger regions, these are passed to the GCT at a data rate of  $172.8 \text{ Gbs}^{-1}$ .  
<sup>11</sup> These trigger regions are clustered in to jet candidates by the GCT and ranked. The jets  
<sup>12</sup> are then sub-divided in the categories depending on their pseudo-rapidity and the result  
<sup>13</sup> of  $\tau$  identification.

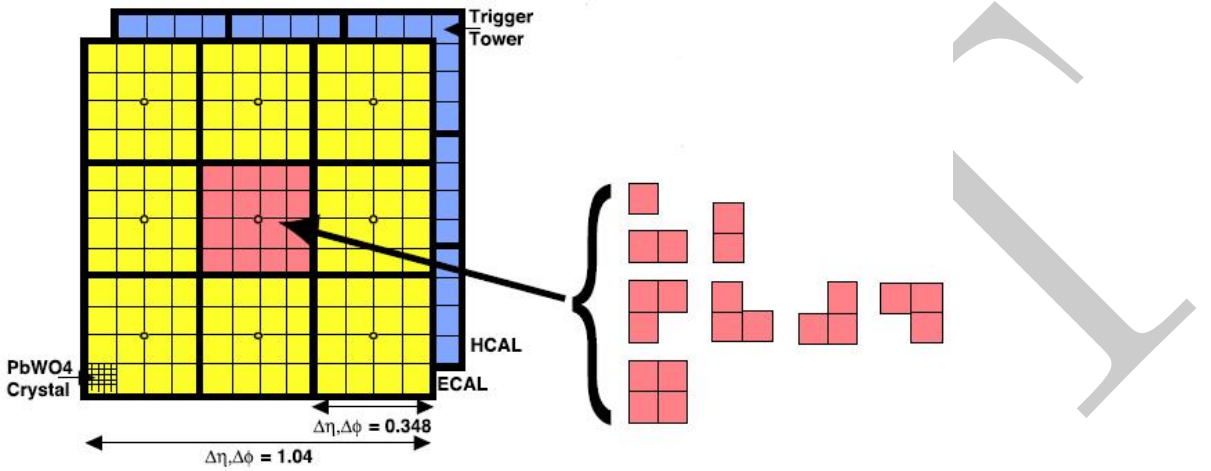
<sup>14</sup> Energy sums come in two forms, the total transverse energy  $E_T$  which is the scalar  
<sup>15</sup> sum of all transverse energies and the total jet transverse energy  $H_T$  which is calculated  
<sup>16</sup> as the scalar sum of all jets above some programmable threshold.

<sup>17</sup> The missing energy equivalents of these  $E_T$  and  $H_T$  are formed from the negative  
<sup>18</sup> vector sum of the objects considered for the transverse sums.

## <sup>19</sup> 4.1 Level-1 Trigger Jet Algorithm [34]

<sup>20</sup> The CMS detector can be un-rolled in the  $\phi$  direction to form a rectangular grid of the  
<sup>21</sup> 396 calorimeter regions, connected along the  $\phi$  edge. The rectangle is formed from 18  
<sup>22</sup>  $\phi$  divisions (from  $-180^\circ < \phi \leq 180^\circ$ ) and 22  $\eta$  divisions (from  $-5 < \eta < 5$ ). Each  $\phi$   
<sup>23</sup> division corresponds to  $20^\circ$ . The  $\eta$  divisions correspond to  $\Delta\eta = 0.5$  in the forward  
<sup>24</sup> calorimeters and to  $\Delta\eta \approx 0.348$  in the barrel. A pictorial representation of this can be  
<sup>25</sup> seen in figure 4.3.

<sup>26</sup> A jet candidate is created if the sum of the ECAL and HCAL energies of the central  
<sup>27</sup> calorimeter region has an energy deposit larger than all of its neighbours, as shown in  
<sup>28</sup> figure 4.2. The jet is centred at this region where  $p_T^{central} > p_T^{surrounding}$  and the transverse  
<sup>29</sup> energies of the surrounding regions are summed in to the central region. The jet is then  
<sup>30</sup> classified as a  $\tau$  jet if  $|\eta| < 3.0$  and none of the  $\tau$  veto bits are set. If any  $\tau$  vetoes are set  
<sup>31</sup> the jet is classified as a central jet. The jet is classified as forward if  $3.0 < |\eta| < 5.0$



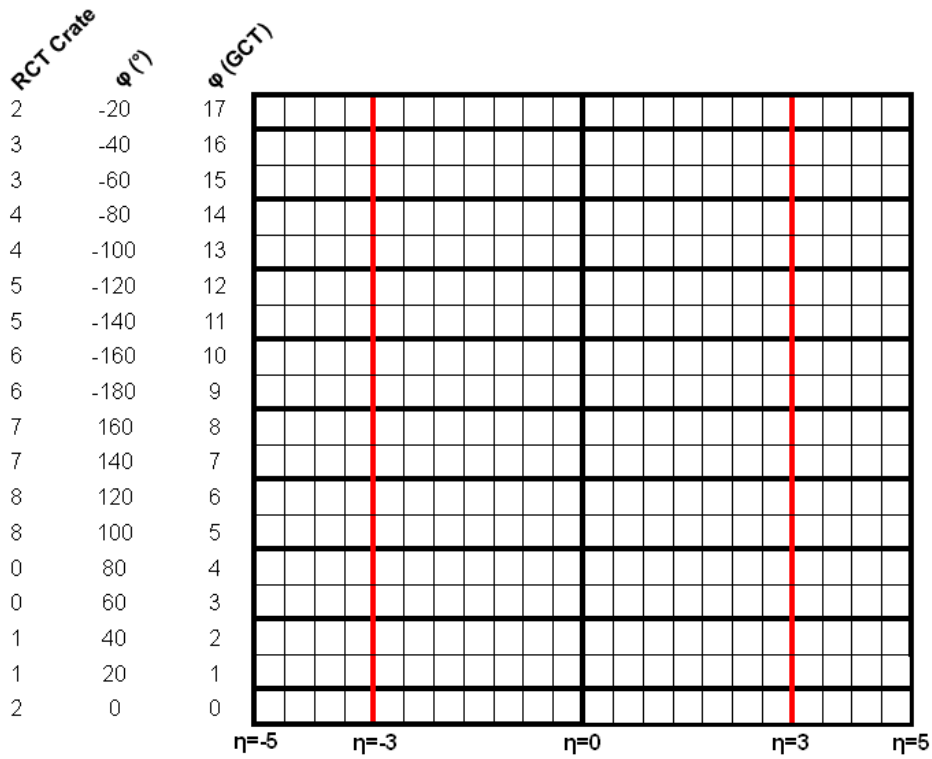
**Figure 4.2:** The  $3 \times 3$  jet-finder window at Level-1. Each cell represents a trigger tower, which is the sum of the HCAL and ECAL transverse energies. The  $\tau$ -jet veto patterns are shown to the right.

1     The  $\tau$ -vetoes are set by the RCT depending on whether or not the energy depositions  
 2    in up to four contiguous trigger towers are below a programmable fraction of the regional  
 3     $E_T$  as shown in Figure 4.2.

4     It is possible to apply separate jet energy corrections to each of the sub categories of  
 5    GCT jets, however at current the same  $E_T$  and  $\eta$  dependant corrections are used for all  
 6    three jet types.

7     In order to reduce the total data duplicated and shared between the jet finders  
 8    the GCT employs a pre-clustering algorithm, which involves 18 jet finders operating  
 9    simultaneously over the whole detector. These jet finders then only share information  
 10   with neighbouring regions when the clustered jets are found. Figure 4.3 shows the  
 11   boundaries between which the jet finders operate, these map naturally on to one RCT  
 12   crate per jet finder. A maximum of 3 jets can be found on each of the  $\phi$  strips acted  
 13   on by the jet finders, this gives a maximum of 108 jets per event. In order to preserve  
 14   continuity across the  $\eta = 0$  boundary, the two adjacent trigger regions are shared between  
 15   the jet finders.

16    An example of the jet finding is shown in Figure 4.4. The first step is to create a  $2 \times 3$   
 17   mini cluster around any local maxima found in the  $12 \times 2$  strip. Equality statements  
 18   are imposed so that the energy of the central cell is greater than its neighbours in some  
 19   directions and greater than or equal to the neighbours other directions to enforce a gap  
 20   of at least one trigger region in both  $\eta$  and  $\phi$  between the centres of the clustered jets.

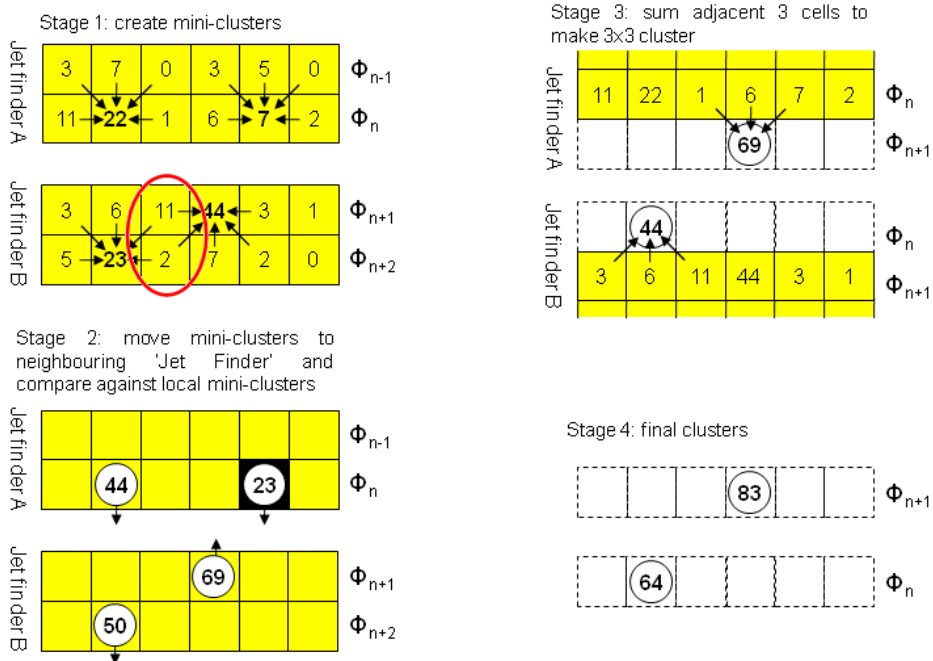


**Figure 4.3:** The calorimeter map that the  $3 \times 3$  jet-finder operates over is made up for 396 calorimeter regions, each jet finder is mapped on to an RCT crate which is composed of an  $11 \times 2$  strip of these regions. RCT crate labels are shown for negative  $\eta$  only.

1 In the second step the jet finder transfers the three largest mini clusters on a given  
 2  $\phi$  strip to the closest  $\phi$  strip on the neighbouring jet finder. These are then compared  
 3 against the existing mini clusters in that  $\phi$  strip, those that are adjacent or diagonally  
 4 adjacent to a larger mini cluster are removed. The inequality statements are then  
 5 reimposed to prevent problems with clusters having the same energies. In the final stages  
 6 the mini clusters have their three adjacent regions summed in to produce a  $3 \times 3$  jet  
 7 cluster. Finally the four highest ranked jets are corrected and passed to the GT.

## 8 4.2 Level-1 Trigger Performance

9 During the start of data taking in 2010, no Jet Energy Corrections (JEC's) were applied  
 10 in the Level-1 trigger. This gave a relatively slow turn on in terms of offline hadronic  
 11 objects. During the winter shut down of the LHC between the 2010 and 2011 running  
 12 periods a set of Level-1 JEC's were developed. These corrections used a piecewise cubic



**Figure 4.4:** The Level-1 jet clustering method, six cells in  $\eta$  are shown. An example of overlapping jets is shown

1 form for the interpolation function used to correct the jet energy dependant on it's  
 2 uncorrected  $E_T$  and  $\eta$  values. However as can be seen in Figure 4.5 these corrections  
 3 were only applied to jets with a raw energy below 130 GeV, the secondary lobe shows  
 4 those objects that do not have their energy corrected.

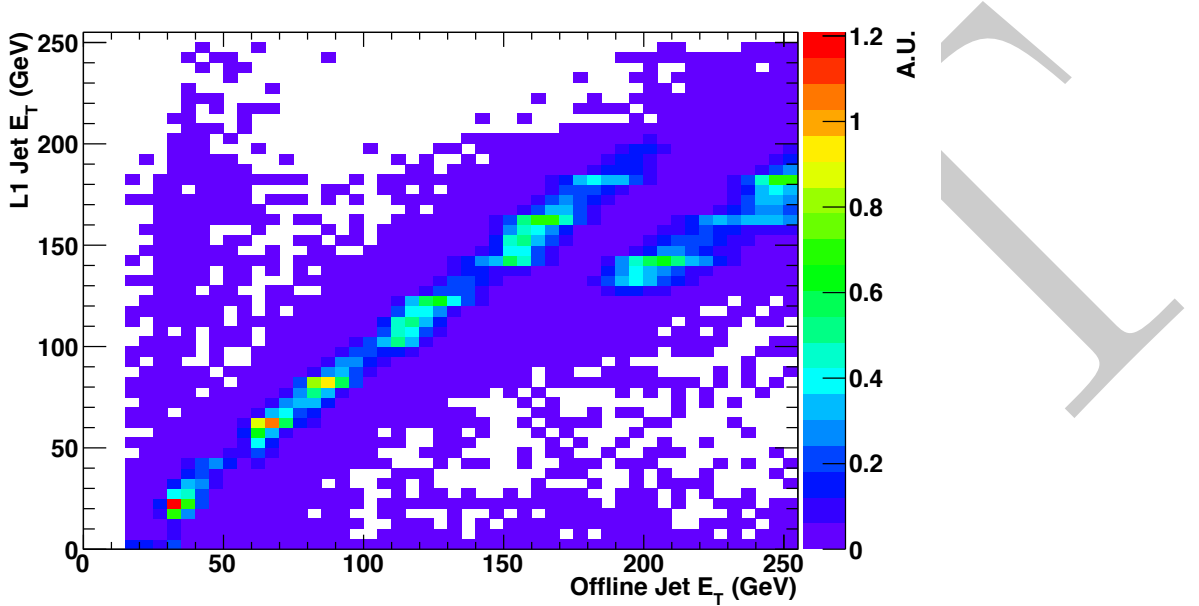
5 To overcome this a new set of corrections were derived using a well established tool  
 6 for producing offline corrections,

7 **REFERENCE TO tapper-001 here**

8 using the same functional form that was derived for correcting particle flow jets.

9 **REFERENCE TO PF HERE**

10 In this section we discuss the performance of both sets of Level-1 JEC's and the  
 11 performance of the energy sum triggers  $H_T$ ,  $\cancel{H}_T$ , and  $\cancel{E}_T$ , the performance of which are  
 12 not effected by the application of jet energy corrections at the Level-1 trigger due to the  
 13 quantities being built from the internal GCT jets before they pass though the corrections  
 14 look up table. The performance is studied under both low pile up conditions where the  
 15 mean peak pile up  $\langle PU \rangle$  is 16 primary vertices and under high pile up conditions  
 16 where  $\langle PU \rangle$  is 36 primary vertices.

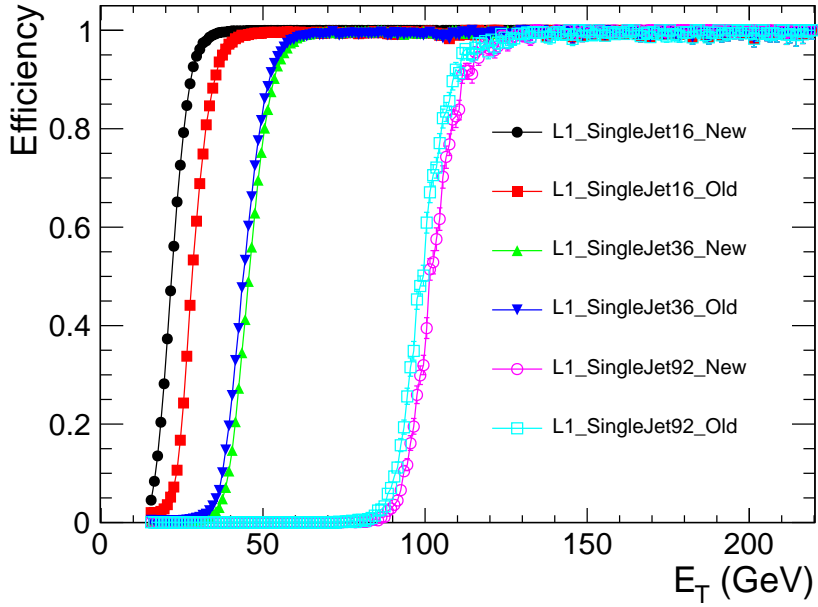


**Figure 4.5:** Correlation between offline corrected jet energy and Level-1 corrected jet energy for matched jets. The discontinuity shows where the Level-1 jet corrections do not alter the raw energy of the jet.

1 To measure the performance of the Level-1 single jet triggers we assume that the  
 2 leading offline corrected anti- $k_t(0.5)$  calorimeter jet is the jet that triggered the event.  
 3 We then match this offline jet to the closest Level-1 jet in  $\Delta R$ , where for there to be a  
 4 match  $\Delta R < 0.5$  is required. For this match central,  $\tau$  and forward jets are considered.  
 5 Events where the recorded Level-1 energy is set to the overflow bit, meaning they have  
 6 more than 254 GeV of  $E_T$  measured at Level-1 are ignored.

7 To collect an unbiased sample in which to measure the performance, two methods  
 8 are used; the first is to require a Minimum Bias trigger, which is triggered by beam  
 9 induced activity in the CMS detector. However due to the nature of these collisions the  
 10 number of events with high energy interactions is low and the prescale applied to this  
 11 trigger further reduces the sample size. However this method does produce the least bias.  
 12 The second method is to trigger an object that does not deposit significant energy in the  
 13 calorimeter systems, in this case we choose the muon trigger with the lowest un prescaled  
 14  $p_T$  threshold. The muon trigger is chosen with some loose isolation requirements to  
 15 make sure it does not overlap with a jet, causing a discrepancy in the measure of the  
 16 calorimetric energy. The sample has a higher number of events due to the large amount  
 17 of bandwidth given to the single object muon triggers in CMS. The use of a muon trigger

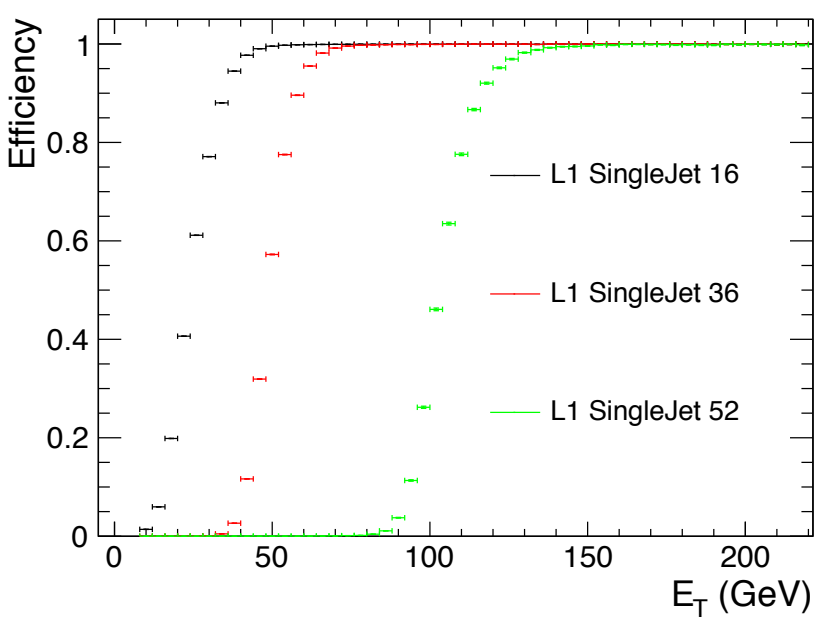
- 1 also serves to increase the precision of the measurement of the Level-1 missing energy  
 2 trigger as the muons are not seen by the calorimeter system the  $\cancel{E}_T$  sample is enriched.



**Figure 4.6:** Comparison of the performance of L1\_SingleJet16, L1\_SingleJet36 and L1\_SingleJet92, when using the piecewise cubic corrections and using the new correction scheme. The difference in performance of the two is negligible above 36GeV.

- 3 Figure 4.6 shows the performance of the piecewise cubic corrections (PWC) and the  
 4 performance of the new corrections. The data was taken with the PWC enabled in the  
 5 GCT hardware. The updated corrections were emulated in the bitwise reproduction  
 6 of the GCT. This made an event by event comparison possible. At low  $E_T$  the new  
 7 corrections turn on before the PWC corrections, if the new corrections were applied on  
 8 with no change to the trigger menu, the Level-1 trigger rate would rise. At a threshold of  
 9 36 GeV and higher the performance of the two correction schemes is very similar. Due to  
 10 the small change in observed performance and the ability to correct raw energies above  
 11 130 GeV, the new corrections were deployed online at the start of Run2011B and are  
 12 still online at the end of data taking in 2012.

- 13 The performance of the updated corrections was then measured with data taken with  
 14 the corrections applied in the GCT hardware. The reference sample was taken with the  
 15 HLT\_IsoMu24\_v\* high level muon trigger. The performance of three example triggers is  
 16 shown in Figure 4.7. The data collected and represented in Figure 4.7 has a peak mean pile  
 17 up ( $< PU >$ ) of 16 interactions, this is higher than the  $< PU >$  of approximately 8-10



**Figure 4.7:** Performance measurements of L1\_SingleJet16, L1\_SingleJet36 and L1\_SingleJet92, when using the new correction scheme deployed in the GCT hardware. The performance is slightly worse than that of the emulated triggers due to a change in pile up conditions between the two data taking periods.

present in Run2011A, on which the previous comparison was performed. The observed difference in the performance of the Level-1 single jet triggers as a function of pile up is a case of concern when data taking is underway at the LHC's design luminosity, where  $\langle PU \rangle$  is  $>36$  at an instantaneous luminosity of  $1 \times 10^{34} \text{ cm}^{-27} \text{ s}^{-1}$ .

The instantaneous luminosity in 2012 was predicted to be  $5 \times 10^{33} \text{ cm}^{-27} \text{ s}^{-1}$ , with  $\langle PU \rangle \approx 32$ . In order to study the effect on the trigger rate and efficiency a high pile up, low instantaneous luminosity, LHC fill was taken in 2011.

The Level-1 single jet performance was studied in this run in terms of two offline object definitions. The first was the standard anti- $k_t(0.5)$  calorimeter jet reconstruction, the second was a set of anti- $k_t(0.5)$  calorimeter jets which were corrected for pile up using the fastjet correction algorithm,

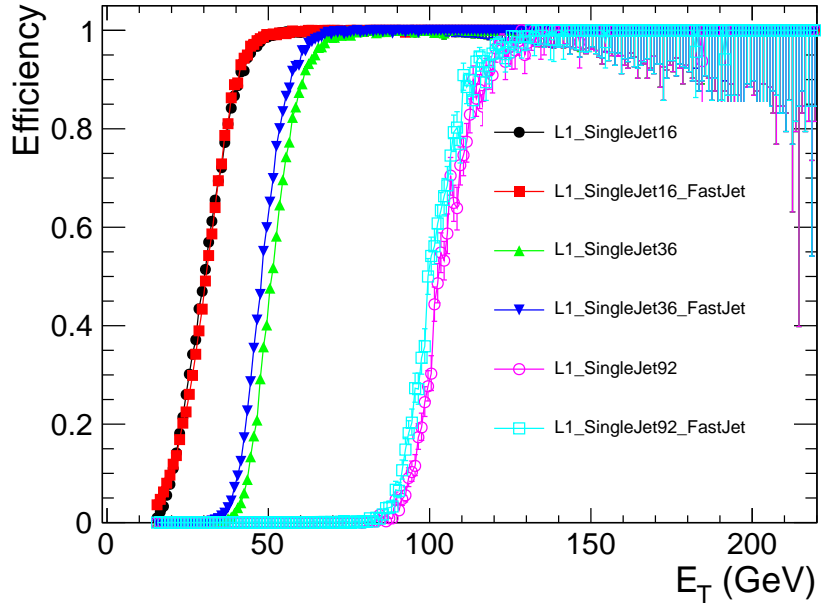
cite fast jet

which is further detailed in Section 6.2.1. The fast-jet corrections remove the energy deposited by the secondary interactions from the objects which are expected to come from the primary hard interaction, thus removing energy from the offline jets. The effect

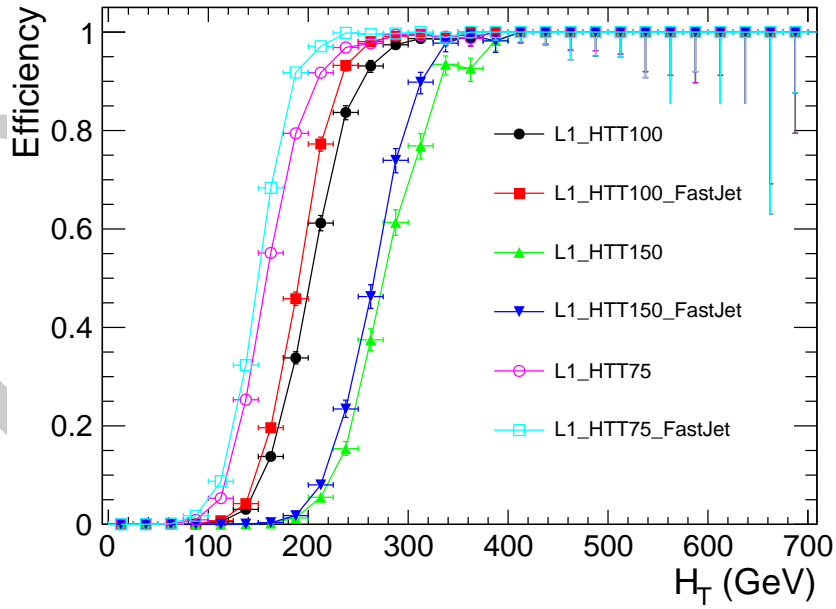
of these pile up corrections on the Level-1 trigger performance is first studied under conditions with  $\langle PU \rangle$  of 16, the performance of which has already been measured with respect to non pile up corrected offline objects, as a sanity check. The results are shown in Figure 4.8 , the performance is measured with respect to HLT\_IsoMu24\_v\*, in terms of both pile up corrected and standard offline objects. As expected the performance in the two cases is very similar. The same comparison is shown for  $H_T$  in Figure 4.9, where the effect of the fastjet corrections is more pronounced due to the sum over jets. The difference between the turn on points for the two offline quantities is on the order of 10 GeV under low pile up conditions.

Due to the high pile up fill being a specialised fill with low instantaneous luminosity, the high level trigger paths were disabled, instead Level-1 trigger pass though paths were utilised to take the data. The Level-1 single muon pass though trigger is used to collect the reference sample. Otherwise the same analysis method is common between the two data sets. Figure 4.10 shows the difference in turn on for three example Level-1 single jet triggers when using standard calorimeter jets and fastjet corrected calorimeter jets. In the high pile up conditions the switch to offline jets that are corrected for pile up shifts the turn on point to lower values of  $E_T$ , the magnitude of this effect reduces as the Level-1 trigger trigger threshold raises. This implies that the same offline performance as seen in the low pile up conditions can be achieved by using the pile up corrected offline objects and raising the Level-1 single jet trigger thresholds.

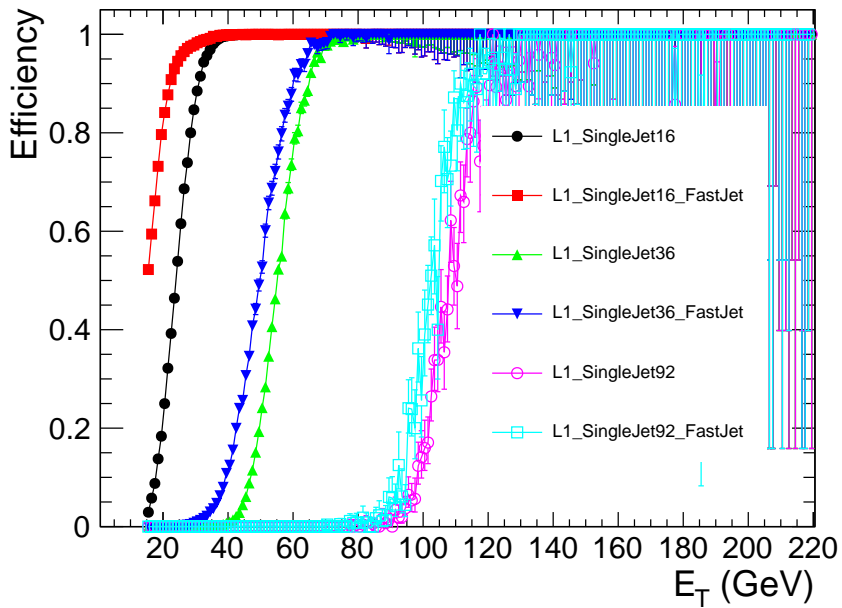
Figure 4.11 shows the same high pile up comparison, but for the Level-1  $H_T$  triggers. Due to the size of the sample the precision of this measurement is low. However the same trend of a shift to lower  $H_T$  values of the turn on point of the Level-1 triggers when using pile up corrected offline objects is observed. This again implies that the Level-1  $H_T$  trigger thresholds can be raised whilst preserving the same offline performance as during the low pile up conditions.



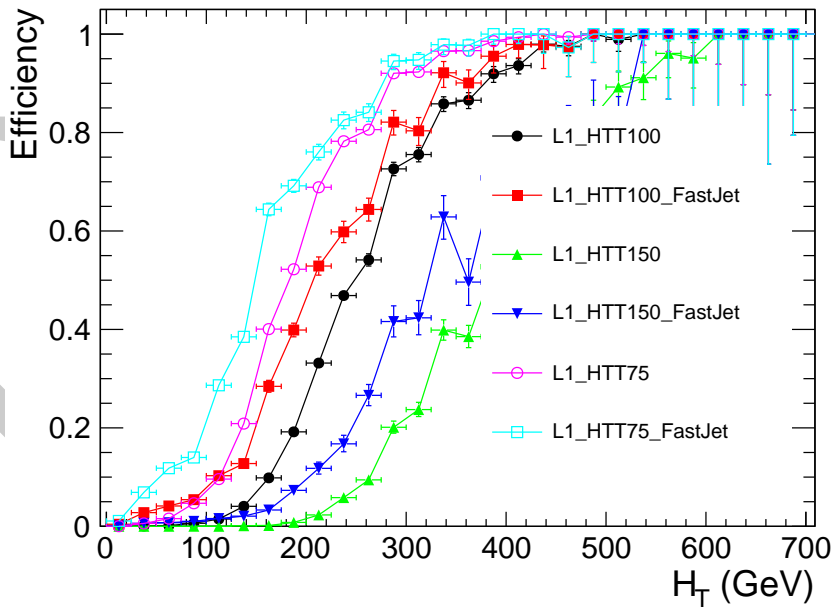
**Figure 4.8:** Comparison of the performance of L1\_SingleJet16, L1\_SingleJet36 and L1\_SingleJet92 triggers. Where  $\langle PU \rangle = 16$ . For two offline reconstruction methods, standard anti- $k_t(0.5)$  calorimeter jets and pile up corrected anti- $k_t(0.5)$  calorimeter jets.



**Figure 4.9:** Comparison of the performance of L1\_HTT75, L1\_HTT100 and L1\_HTT150 triggers. Where  $\langle PU \rangle = 16$ . For two offline reconstruction methods, standard anti- $k_t(0.5)$  calorimeter jets and pile up corrected anti- $k_t(0.5)$  calorimeter jets.



**Figure 4.10:** Comparison of the performance of L1\_SingleJet16, L1\_SingleJet36 and L1\_SingleJet92 triggers. Where  $\langle PU \rangle = 36$ . For two offline reconstruction methods, standard anti- $k_t(0.5)$  calorimeter jets and pile up corrected anti- $k_t(0.5)$  calorimeter jets.



**Figure 4.11:** Comparison of the performance of L1\_HTT75, L1\_HTT100 and L1\_HTT150 triggers. Where  $\langle PU \rangle = 36$ . For two offline reconstruction methods, standard anti- $k_t(0.5)$  calorimeter jets and pile up corrected anti- $k_t(0.5)$  calorimeter jets.

## 4.3 Level-1 Trigger Pile-up Mitigation

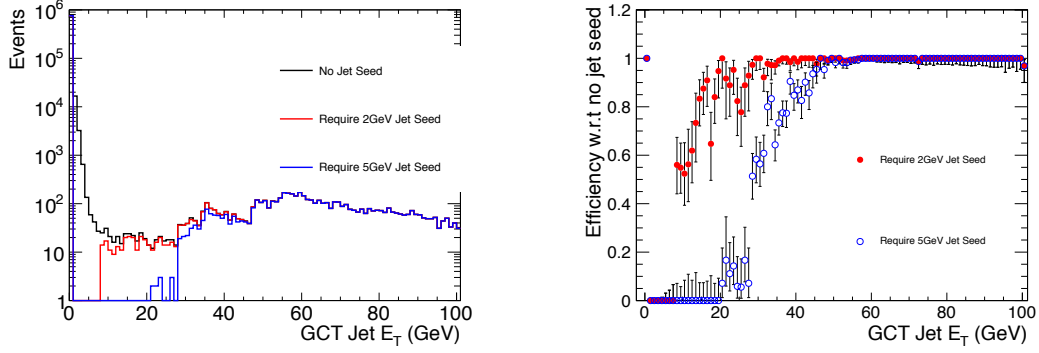
Whilst we have seen that the offline performance of the Level-1 hadronic triggers can be maintained when raising the trigger thresholds to deal with increased rate, when switching to pile up corrected offline objects. Figure 4.14 shows the trigger cross section as a function of instantaneous luminosity for the L1\_HTT150 trigger, which requires  $H_T > 150$  GeV. However beyond a certain point raising thresholds causes a loss of performance. In this section we look at a method to reduce the effects of pile up hadronic Level-1 triggers, by making an addition to the Level-1 jet finding algorithm.

In Section 4.1 the Level-1 jet clustering algorithm was described. The proposed change was to add a requirement that the seeding region has a direct energy threshold, in addition to the equality relations that are set up. The effects of applying a 2 GeV or a 5 GeV threshold are studied. This threshold is on the raw, uncorrected energy of the trigger towers and effects all Level-1 jets. The impact will be seen in the Level-1 jet triggers which use corrected energy and Level-1  $H_T$  and  $\cancel{H}_T$  which are formed from uncorrected jets. The aim is to remove the events which are accepted due to pile up, but not to remove physics events.

The triggers most effected by this change are the energy sum triggers as they sum many jets of low threshold, whereas the single object triggers are already cutting on high  $E_T$  objects.

Figure 4.12(a) shows the internal GCT uncorrected jet energy spectrum in high pile up conditions, taken with the L1\_SingleMu pass though triggers. The three histograms are for; no application of jet seed threshold in black, where there are many low  $E_T$  jets; In red a 2 GeV seed requirement is made, the effect is to cut out all jets below 2 GeV and cut out jets with an energy up to approximately 35 GeV of uncorrected energy; The blue histogram shows the jet energy spectrum after applying a 5 GeV seed threshold, the effect is to remove all jets below 5 GeV and to cut out jets with energy up to 55 GeV. Figure 4.12(b) shows the efficiency with respect to the no seed sample for the two test seed thresholds. The removal of jets in the low energy region of the  $E_T$  spectrum is where the advantage of applying a seed threshold is seen over simply raising the trigger thresholds, or raising the threshold of jets to be included in the Level-1  $H_T$  or  $\cancel{H}_T$  calculation.

To quantify the effects of the addition of the jet seed a low pile up sample, where the effects are expected to be small, is studied in terms of rate reduction and efficiency change. The dedicated high pile up fill is then studied in terms of rate reduction, due to



(a) GCT internal uncorrected jet  $E_T$  distributions for the same events with a 0, 2 or 5 GeV seed requirement.  
(b) Efficiency of applying a requirement of 2 or 5 GeV with respect to no requirement.

**Figure 4.12:** Effect of requiring a jet seed threshold on GCT internal jets.

the limited sample size of the high pile up fill the change in efficiency on this sample is not studied. However due to the addition of energy from the secondary pile up interactions the change in efficiency in the low pile up sample is the worse case scenario.

Table 4.1 details the rate reduction with respect to the 0 GeV seed threshold for seed thresholds of 2 GeV and 5 GeV for three example triggers, these are:

- L1\_SingleJet50, which requires at least one jet with  $E_T > 50$  GeV with in  $|\eta| < 3.0$ ;
- L1\_QuadJet38, which requires 4 jets with  $E_T > 38$  GeV with in  $|\eta| < 3.0$ ;
- L1\_HTT100, which requires that Level-1  $H_T > 100$  GeV.

The rate of L1\_SingleJet50 is not effected by the requirement of a 2 GeV seed threshold and is reduced by 15% when a 5 GeV seed requirement is made. The L1\_QuadJet38 trigger rate is reduced by the same amount as the single jet trigger, under low pile up conditions for both seed thresholds. L1\_HTT100 sees a 2% rate reduction when requiring a 2 GeV seed threshold and a 3% reduction in rate when requiring a 5 GeV seed.

Table 4.2 shows the rate reduction under high pile up conditions with respect to the 0 GeV seed threshold requirement, for the same three example triggers as in the low pile up case. The rate of L1\_SingleJet50 is not reduced when making a 2 GeV seed requirement, when making a 5 GeV seed requirement the single jet 50 GeV rate is reduced by 30%. The rate of L1\_QuadJet38 is reduced by 30% when requiring a 2 GeV

**Table 4.1:** Summary of rate reduction during low pile up conditions.

Trigger	% rate reduction with a 2GeV requirement	% rate reduction with a 5GeV requirement
L1_HTT100	$3 \pm 11\%$	$3 \pm 11\%$
L1_QquadJet38	$0 \pm 0\%$	$15 + 6 - 8\%$
L1_Jet50	$0 + 0 - 12\%$	$15 + 9 - 15\%$

**Table 4.2:** Summary of rate reduction during high pile up conditions.

Trigger	% of rate taken with 2GeV requirement	% of rate taken with 5GeV requirement
L1_HTT100	$40 \pm 5.7\%$	$99 + / - 50\%$
L1_QquadJet38	$30 \pm 20\%$	$40 + 22 - 24\%$
L1_Jet50	$0 + 7 - 0\%$	$30 + 10 - 12\%$

- <sup>1</sup> seed and by 40% when requiring a 5 GeV seed. The rate of L1\_HTT100 is reduced by  
<sup>2</sup> 40% when requiring a 2 GeV seed threshold and when requiring a 5 GeV seed threshold  
<sup>3</sup> the rate is reduced by  $\approx 99\%$ , however the statistical error on this prediction is large.

#### <sup>4</sup> 4.3.1 Effect on trigger efficiency

- <sup>5</sup> Section 4.3 shows that requiring a jet seed threshold substantially reduces the trigger  
<sup>6</sup> acceptance rate at in high pile up conditions.

- <sup>7</sup> However the aim of requiring a jet seed is to reduce rate, but not at the cost of physics.  
<sup>8</sup> In this section we look at the effects of requiring a seed threshold, whilst requiring some  
<sup>9</sup> loose, generic offline selection on the hadronic objects.

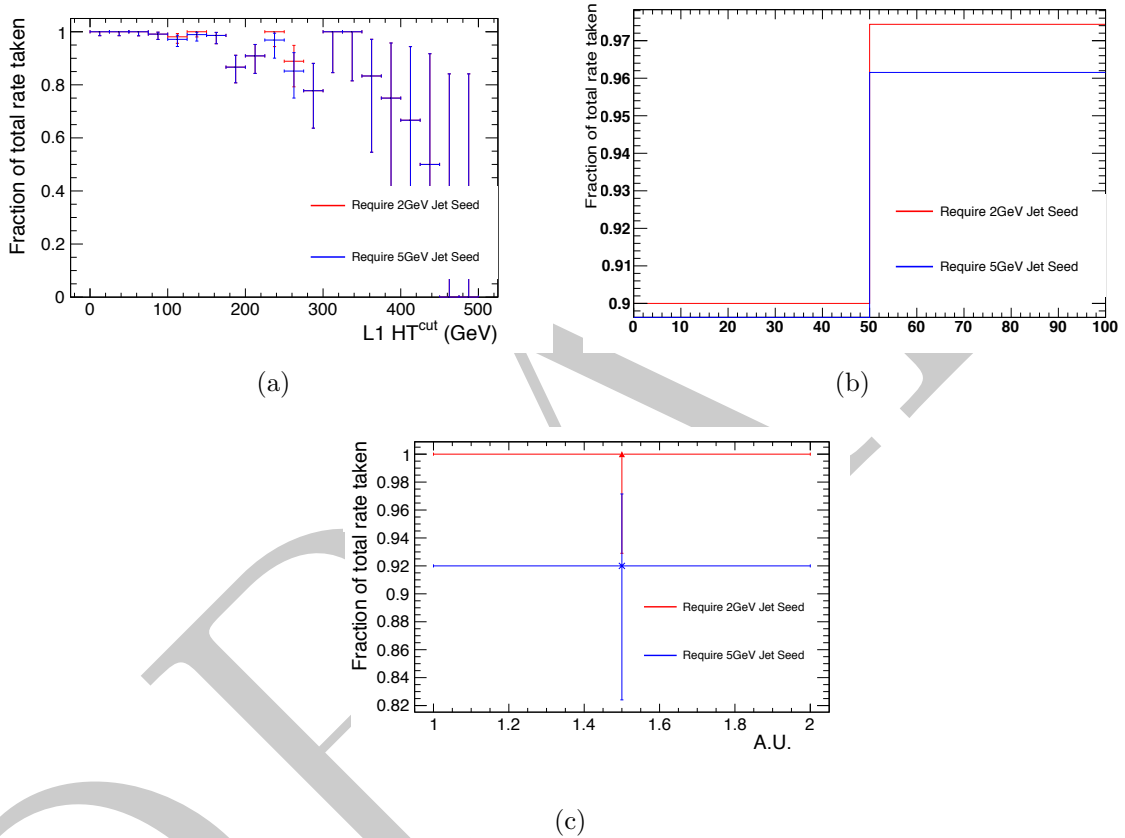
- <sup>10</sup> The change in efficiency is measured under low pile up conditions where the least  
<sup>11</sup> extra energy added to the event. This gives a worse case estimate of the effect of requiring  
<sup>12</sup> a jet seed on the offline efficiency.

- <sup>13</sup> Each offline reconstructed calorimeter jet must adhere to the following quality criteria:

- <sup>14</sup> • Pass loose calorimeter ID;

- <sup>15</sup> •  $p_T \geq 30$  GeV;

- 1     •  $|\eta| \leq 3.0$ ;
- 2     • Matched to a Level-1 jet with  $\Delta R \leq 0.5$ .
- 3     Where loose calorimeter ID is defined as; Electro-Magnetic fraction  $> 0.01$ , fraction of  
4     energy in the Hybrid Photo Diodes  $< 0.98$  and the number of n90hits  $> 1$ .



**Figure 4.13:** Efficiency reductions for various Level-1 algorithms when applying a 2 or 5 GeV seed tower requirement, in low pile up conditions. Figure (a) shows the efficiency reduction for  $H_T$  triggers at low pile up in cut steps of 25 GeV. Figure (b) shows the efficiency reduction for jets with  $|\eta| < 3$ . and  $p_T > 50$  GeV. Figure (c) show the efficiency reduction for a quad jet trigger, with jet  $|\eta| < 3$ . and  $p_T > 38$  GeV.

5     **Efficiency of  $H_T$  Triggers** Figure 4.13(a) shows the acceptance reduction after  
6     applying the two jet seed thresholds. The distribution is the cumulative number of events  
7     passing a cut of  $L1HT^{cut}$  in bins of 25 GeV. Due to  $H_T$  being the scalar sum of the  
8     jet  $p_T$ 's in the event the value of Level-1  $H_T$  is reduced as jets are removed from the  
9     calculation. To preserve efficiency the Level-1 trigger threshold will have to be reduced.  
10   When comparing to the high pile up rate reduction in table 4.2 it is shown that the trigger

<sup>1</sup> rate can be reduced by  $\approx 20\%$  when requiring a 2 GeV seed threshold and reduced by  
<sup>2</sup>  $\geq 99\%$  when requiring a 5 GeV seed threshold, for a trigger threshold of 100 100 GeV.

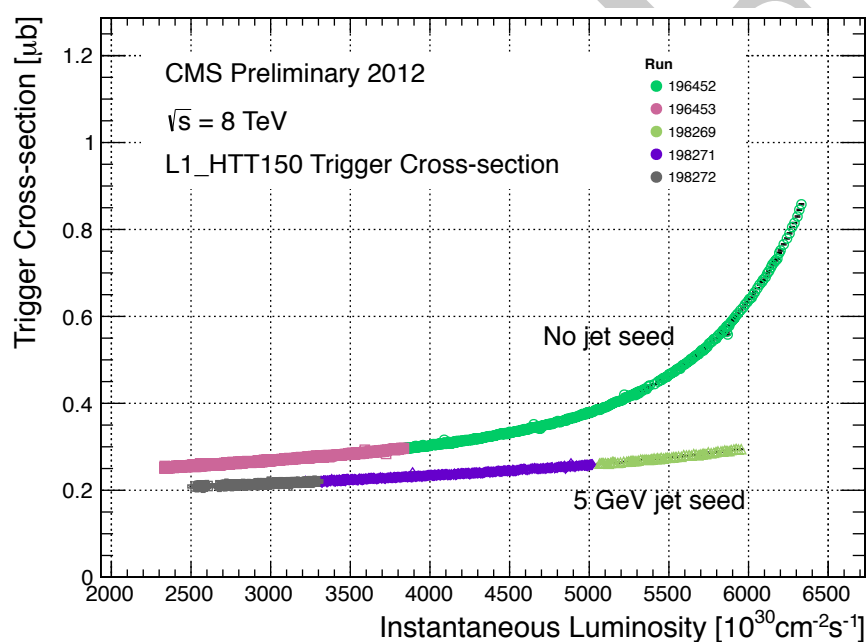
<sup>3</sup> **Efficiency of Jet Triggers** Figure 4.13(b) shows the change in acceptance of jets in  
<sup>4</sup> low pile up conditions when the two seed thresholds are required. The effect is on the  
<sup>5</sup> order of a few percent for each of the thresholds. Requiring a 2 GeV seed reduces the  
<sup>6</sup> efficiency for jets above 50 GeV by  $\approx 2.5\%$ , whilst requiring a 5GeVseed reduces the  
<sup>7</sup> efficiency of the same jets by  $\approx 4\%$ .

<sup>8</sup> **Efficiency of MultiJet Triggers** Figure 4.13(c) shows that the effect of requiring a  
<sup>9</sup> seed threshold of 2 GeV has no effect on the efficiency of the quad jet 38 GeV trigger  
<sup>10</sup> and requiring a seed threshold of 5 GeV reduces the efficiency of the quad jet 38 trigger  
<sup>11</sup> by 8%. The change in rate is dramatic in high pile up conditions where for a 2 GeV seed  
<sup>12</sup> threshold the rate is reduced by  $\approx 30\%$  and by  $\approx 40\%$  when requiring a 5 GeV seed.  
<sup>13</sup> However it is to be noted that the sample where this measurement has been made is of  
<sup>14</sup> limited size, inferring a reasonably large statistical uncertainty.

### <sup>15</sup> 4.3.2 Summary

<sup>16</sup> The effects of requiring a jet seed have been studied using the Level-1 trigger emulator on  
<sup>17</sup> high and low pile-up samples. The studies show that requiring a jet seed of 5GeVgreatly  
<sup>18</sup> reduces the rate of the  $H_T$  and Multi Jet triggers in high pile up conditions, whilst not  
<sup>19</sup> adversely effecting the data taking efficiency of these triggers.

<sup>20</sup> The cross section of L1.HTT150 has been measured with and with out the addition  
<sup>21</sup> of a jet seed threshold of 5 GeV as shown in Figure 4.14. Ideally the trigger cross section  
<sup>22</sup> would be independent of the instantaneous luminosity and pile up, Figure 4.14 shows  
<sup>23</sup> that the addition of a 5 GeV seed threshold reduces the dependance on instantaneous  
<sup>24</sup> luminosity of the trigger cross section.



**Figure 4.14:** Trigger cross section as a function of number of pile up interactions. Showing that applying a 5 GeV jet seed threshold dramatically reduces the dependance of cross section on the instantaneous luminosity.

# Chapter 5

## <sup>1</sup> Motivating the $\alpha_T$ Analysis

### <sup>2</sup> 5.1 The Problem

<sup>3</sup> If Supersymmetry or some other beyond the S.M theory is to provide a yet undiscovered  
<sup>4</sup> dark matter candidate the Lightest SUSY Particle (LSP), it is predicted that this  
<sup>5</sup> candidate will interact via the weak nuclear force only. This gives a decay topology  
<sup>6</sup> involving missing energy in the form of the dark matter particle escaping the detector.  
<sup>7</sup> Due to the nature of interactions at the L.H.C, these particles would be produced at the  
<sup>8</sup> end of a decay chain of heavy particles that interact strongly, giving a final topology  
<sup>9</sup> involving hadronic objects which are classified as jets for the purpose of analysis and  
<sup>10</sup> missing energy. There are several S.M processes that mimic this final state.

<sup>11</sup> By far the largest of these backgrounds comes from QCD multi jet events where  
<sup>12</sup> fake missing energy is introduced either from failures in reconstruction, or stochastic  
<sup>13</sup> fluctuations in the calorimeter systems.

<sup>14</sup> expand on this -  $E/\sqrt{E}$  has non gaussian tails. Figures of jets falling below  
threshold, missed jets etc. probably from some jet-met paper.

<sup>15</sup> However due to the theoretical errors on the QCD production cross section predicting  
<sup>16</sup> the number QCD background events from Montecarlo simulation is not possible. A  
<sup>17</sup> secondary QCD background also exists, where due to the requirement of a jet  $E_T$   
<sup>18</sup> threshold, multiple jets fall under threshold by a few GeV, this causes a balanced event  
<sup>19</sup> to look unbalanced as the jets under threshold are no longer considered. It is these  
<sup>20</sup> sources of QCD background that  $\alpha_T$  is designed to remove.

1 The second major background comes from S.M electro-weak decays and is irreducible  
2 as the final states involve real missing energy, from neutrinos. The electro-weak decays  
3 that form the back ground are  $W \rightarrow \tau\nu + \text{Jets}$ , where the  $\tau$  is reconstructed as a jet,  
4 or the lepton fails the identification required for the dedicated lepton vetoes,  $Z \rightarrow \nu\bar{\nu}$   
5 + Jets is completely irreducible. These are generally di-jet topologies. At higher jet  
6 multiplicities top quark production followed by semi-leptonic top decay accounts of the  
7 largest background. These backgrounds are predicted using a well understood control  
8 sample this is fully explained in Section 7.1.

9 The final background source is that introduced by detector failure or electronic noise  
10 induced by the movement of the L.H.C proton beam. Approximately 1% of the ECAL  
11 read out is not available in offline event reconstruction, this provides a source of fake  
12 missing energy.

# Chapter 6

## 1 Reconstruction and Event selection

2 **Declaration** In this chapter we discuss the main analysis performed as the subject  
3 of this thesis. For the theoretical motivations of this search please see Chapter 2. The  
4 analysis is based on the full 2011 data set which is made up of  $5 \text{ fb}^{-1}$  of 7 TeV data.  
5 However  $11.7 \text{ fb}^{-1}$  of the 2012 8 TeV is looked at to measure the performance of the  
6 upgraded  $\alpha_T$  HLT paths.

### 7 6.1 The $\alpha_T$ variable.

8  $\alpha_T$  is inspired by Ref [38] and was expanded to transverse multi jet topologies by members  
9 of the CMS collaboration in Refs [22, 23]. The purpose is to provide a variable that can  
10 be cut on to eliminate QCD from the final selection. To do this the inherent balance of  
11 the QCD system is exploited.

12 For di-jet systems  $\alpha_T$  is defined as:

$$\alpha_T = \frac{E_T^{j_2}}{M_T} \quad (6.1)$$

13 where  $E_T^{j_2}$  is the transverse energy of least energetic of the two jets and  $M_T$  is defined as:

$$M_T = \sqrt{\left(\sum_{i=1}^2 E_T^{j_i}\right)^2 - \left(\sum_{i=1}^2 p_x^{j_i}\right)^2 - \left(\sum_{i=1}^2 p_y^{j_i}\right)^2} \quad (6.2)$$

For a perfectly measured di-jet system with  $E_T^{j_1} = E_T^{j_2}$ , where the jets are opposite in  $\phi$   $\alpha_T = 0.5$ , for events with back to back jets where one is miss-measured  $\alpha_T < 0.5$ . However the majority of signals predict many jets in the final state.  $\alpha_T$  can be generalised to work with n-jets in the flowing way. The variables  $H_T$ ,  $\cancel{H}_T$  and  $\Delta H_T$  are constructed,

$$H_T = \sum_{i=0}^{n \text{ jets}} E_T^{jet_i}, \quad (6.3)$$

$$\cancel{H}_T = \left| \sum_{i=0}^{n \text{ jets}} \cancel{p}_T^{jet_i} \right|, \quad (6.4)$$

- <sup>1</sup> for jets above some predefined threshold  $E_T$  which is common for all jet based quantities.
- <sup>2</sup> The multi jet system is reduced to a pseudo di-jet system by forming two large jets. The
- <sup>3</sup> individual jet  $E_T$ 's are summed, with the final configuration being chosen to have the
- <sup>4</sup> minimum difference in energy ( $\Delta H_T$ ) between the pseudo jets. This simple clustering
- <sup>5</sup> criteria provides the best separation between miss-measured events and those with real
- <sup>6</sup>  $\cancel{E}_T$ .

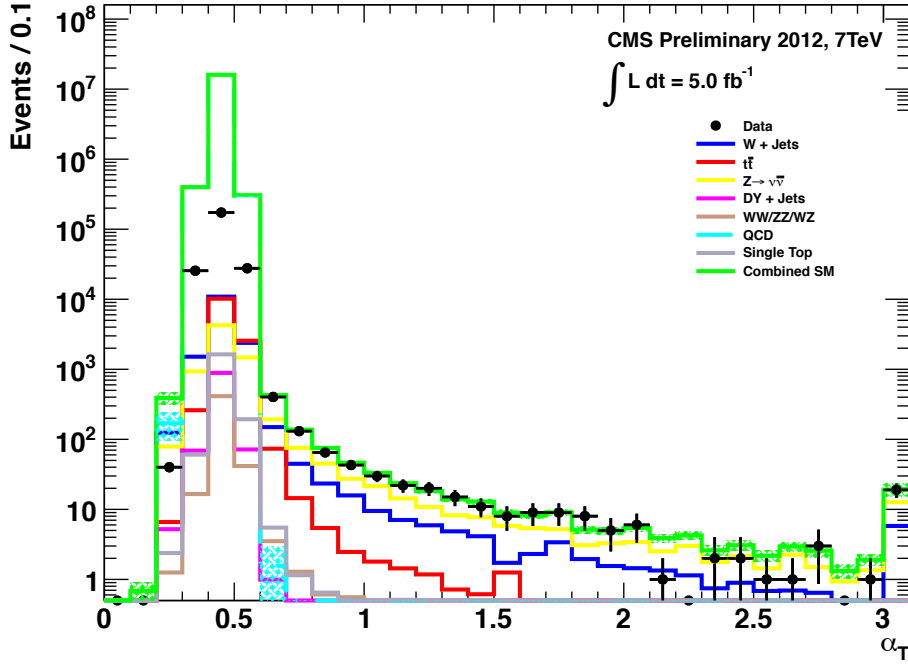
$\alpha_T$  is then defined as:

$$\alpha_T = \frac{H_T - \Delta H_T}{2\sqrt{H_T^2 - \cancel{H}_T^2}} \quad (6.5)$$

- <sup>7</sup> Figure 6.1 shows the  $\alpha_T$  distribution for both data and simulated background samples.
- <sup>8</sup> The QCD multi jet background is negligible above an  $\alpha_T$  value of 0.55, where as the
- <sup>9</sup> standard model processes which involve real  $\cancel{E}_T$  exist at all possible values of  $\alpha_T$ . Values
- <sup>10</sup> of  $\alpha_T$  in the range  $0.5 < \alpha_T < 0.55$  arise in multi jet QCD due to jets falling below
- <sup>11</sup> threshold or large stochastic fluctuations. It is to be noted that the discrepancy between
- <sup>12</sup> data and simulation for  $\alpha_T \leq 0.55$  is due to no trigger emulation being applied to the
- <sup>13</sup> simulated background samples.

## 6.2 Event selection

- <sup>15</sup> In order to select events for the hadronic signal sample and the muon and photon control
- <sup>16</sup> samples a common set of section cuts is defined. In this section the objects are defined
- <sup>17</sup> as are the flow of the analysis cuts and filters.

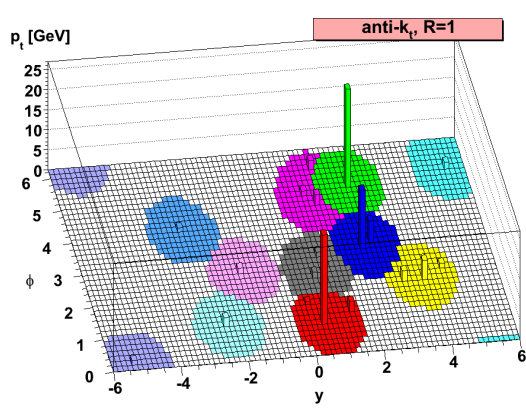


**Figure 6.1:**  $\alpha_T$  distribution for background and data for the region  $H_T > 375$  GeV. Trigger emulation is not applied in the simulated background which leads to the discrepancy in the region  $\alpha_T \leq 0.55$ . The QCD multi-jet background is reduced to less than one event.

### 6.2.1 Preselection of hadronic objects

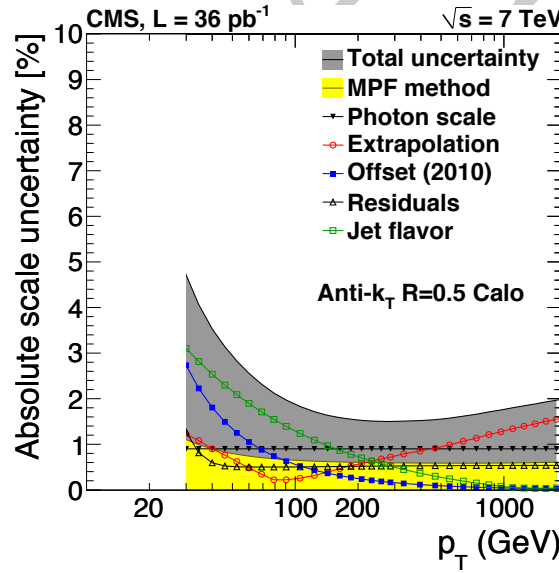
Hadronic showers are clustered into objects which from now on will be referred to as jets. These jets are formed from the energy deposits recorded in the calorimeter towers. Individual jets are clustered using the anti- $k_t(0.5)$  algorithm[17], for high  $p_T$  jets this produces cone like jets, for low  $p_T$  jets deviations from the circular geometry are allowed, as shown in Figure 6.2. C.M.S uses two complimentary reconstruction methods for creating jets, the first uses only calorimeter information, these jets are referred to as anti- $k_t(0.5)$ -Calorimeter jets, the second method adds information from the tracking system to improve the energy resolution and is not used in this analysis due to the requirements of using the same objects at both trigger level and offline to preserve data taking efficiency.

The jets have their raw energies corrected based on their position and momentum to establish a uniform relative response in  $\eta$  and a calibrated absolute response in transverse energy  $E_T$ , with an associated uncertainty of between 2% and 4% dependant on  $E_T$  and



**Figure 6.2:** Simulated hadronic objects clustered in to Jets using the anti- $k_t(0.5)$  jet clustering algorithm, note the high  $p_T$  green object which causes the low  $p_T$  jet in close proximity to be cut off.

- <sup>1</sup>  $\eta$ [18]. Figure 6.3 shows the absolute jet energy scale uncertainty as a function of the jet's  
<sup>2</sup>  $p_T$  for the jets considered in this analysis.



**Figure 6.3:** Absolute jet energy scale uncertainty as a function of jet  $p_T$  for anti- $k_t(0.5)$ -Calorimeter jets[30].

- <sup>3</sup> It is also possible to correct the raw energies of the jets for pile up. Pile up causes  
<sup>4</sup> energy from secondary interactions to be added to the event, for soft pile up interactions  
<sup>5</sup> this energy is distributed uniformly though out the detector. Two forms of pile up  
<sup>6</sup> corrections are used in C.M.S to correct the energies of calorimeter jets. The first is an  
<sup>7</sup> offset correction, the raw energy has a constant energy removed though out the detector

<sup>1</sup> based on the number of primary vertices in the event. The second method is to calculate  
<sup>2</sup> per event the average energy deposited in each calorimeter tower using the **FastJet**[[2](#), [3](#)]  
<sup>3</sup> jet clustering package, this quantity is referred to as  $\rho$  and is also used to correct the  
<sup>4</sup> isolation variables for electrons, muons and photons.

<sup>5</sup> The jets considered in the analysis are not corrected for pile up, each jet is required  
<sup>6</sup> to have  $E_T > 50$  GeV, the highest  $E_T$  jet in the events is required to be within tracker  
<sup>7</sup> acceptance ( $|\eta| < 2.5$ ) and the sub leading jet is required to have  $E_T > 100$  GeV. In the  
<sup>8</sup> lowest two offline  $H_T$  bins the jet thresholds are scaled to preserve the jet multiplicity,  
<sup>9</sup> for the bin  $275 \text{ GeV} < H_T < 325 \text{ GeV}$ , the jet threshold is  $36.6 \text{ GeV}$  and the sub leading  
<sup>10</sup> jet threshold is  $73.3 \text{ GeV}$ . In the bin  $325 \text{ GeV} < H_T < 375 \text{ GeV}$ , the jet threshold is  
<sup>11</sup>  $43.3 \text{ GeV}$  and the sub leading jet threshold is  $86.6 \text{ GeV}$ .

<sup>12</sup> The quantities  $H_T$  and  $\cancel{H}_T$  are then formed from these jets.

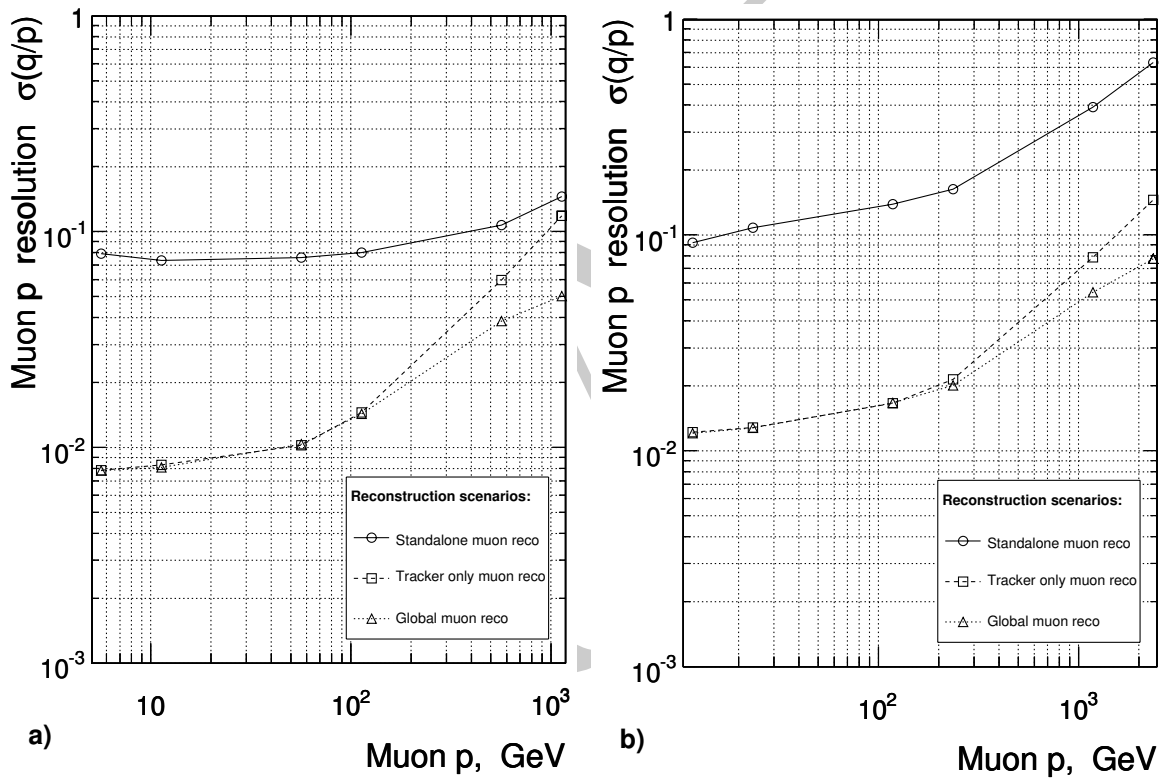
### <sup>13</sup> 6.2.2 Electrons

<sup>14</sup> Two complementary algorithms are used at the track seeding stage of the electron  
<sup>15</sup> reconstruction. Tracker driven seeding which is more suitable for low  $p_T$  ( $p_T < 5$  GeV)  
<sup>16</sup> electrons and ECAL driven seeding, which starts at the ECAL and works back towards  
<sup>17</sup> the interaction point. The ECAL driven seeding starts by creating superclusters[[28](#)]  
<sup>18</sup> which contain information on the lateral shower shape in the  $\eta$  direction of the electron  
<sup>19</sup> or photon shower and the spread of energy deposits in the  $\phi$  plane for electrons, due  
<sup>20</sup> to the radiation of photons by the electron in the C.M.S magnetic field. Track seeds  
<sup>21</sup> from inner tracking layers and electron track are then build from these track seeds. The  
<sup>22</sup> trajectories are reconstructed using a dedicated modeling of the electron energy loss and  
<sup>23</sup> fitted with a Gaussian Sum Filter[[9](#)]. For the purpose of the analysis an object is defined  
<sup>24</sup> as an electron if it has  $p_T > 10$  GeV,  $|\eta| < 2.5$  and passes “VBTF” working point 95  
<sup>25</sup> quality criteria[[24](#)]. Any event containing an identified electron is vetoed.

### <sup>26</sup> 6.2.3 Muons

<sup>27</sup> Muon reconstruction at C.M.S is designed to be regional meaning that the full recon-  
<sup>28</sup> struction sequence can be run at both the HLT and offline. Regional reconstruction only  
<sup>29</sup> performs the reconstruction in a small part of the detector meaning that the time taken  
<sup>30</sup> is short. As an example the amount of information required to reconstruct a muon in

the silicon tracker is less than one percent of the entire tracker read out. The regions which are reconstructed at the HLT are seeded by the muon candidates produced by the Level-1 trigger even if these muons did not cause the issue of the Level-1 accept. Global muon reconstruction uses information from both the stand alone muon system and from the silicon tracker and performs a fit to the individual detector hits. Figure 6.4 shows the muon  $p_T$  resolution for muons reconstructed using either the muon system only, the tracker only or the global muon reconstruction.



**Figure 6.4:** Resolution of  $(1/p)$  versus  $p$  for standalone, global and tracker-only reconstruction.  
a) Barrel,  $\eta = 0.5$ ; b) Endcap,  $\eta = 1.5$ .[28]

Signal events are vetoed if they contain a muon with  $p_T > 10$  GeV and  $|\eta| < 2.5$  that passes the “VBTF” working point 95 for muons [26]. Two separate muon control samples are defined, one requiring exactly one muon with  $p_T > 10$  GeV, the second requiring two muons, whose invariant mass sums to the Z mass.

### <sup>1</sup> 6.2.4 Photons

<sup>2</sup> Photons are reconstructed in the ECAL using the same methods as used to reconstruct  
<sup>3</sup> electrons. However an anti selection is performed on the tracking requirements. For  
<sup>4</sup> photons which do not convert in the tracker a supercluster energy deposit is required with  
<sup>5</sup> no associated electron track, for photons which undergo pair production in the tracker  
<sup>6</sup> material the tracks associated to the super clusters do not originate from the interaction  
<sup>7</sup> vertex, instead they appear in a layer of the tracker. For unconverted photons the ratio of  
<sup>8</sup> the energy deposited in the central ECAL crystal to the energy of the surrounding  $3 \times 3$   
<sup>9</sup> group of ECAL crystals is used as an identification variable. Signal events are vetoed if  
<sup>10</sup> they contain a photon with  $E_T > 25$  GeV,  $|\eta| < 2.5$  and that passes ID requirements[25].  
<sup>11</sup> A requirement of exactly one photon with  $E_T > 150$  GeV with in  $|\eta| < 1.45$  is made for  
<sup>12</sup> the photon control sample.

## <sup>13</sup> 6.3 Common Analysis cuts

- <sup>14</sup> • **Good run selection**, All detector subsystems on, C.M.S in “Physics Declared”  
<sup>15</sup> mode and all physics object groups have certified the runs and luminosity sections.  
<sup>16</sup> This removes any events where the sub-detectors were in an error state or events  
<sup>17</sup> from before the tracker was switched to high voltage mode.
- <sup>18</sup> • **P.K.A.M (Previously Known As Monsters) filter**, these events are caused  
<sup>19</sup> by beam-gas interactions close to C.M.S, which cause a shower of particles to enter  
<sup>20</sup> the pixel detector along the beam line, resulting in a large proportion of the pixel  
<sup>21</sup> detector to record hits.
- <sup>22</sup> • **Vertex Selection** requires at least one non-fake vertex with at least four associated  
<sup>23</sup> tracks, within a cylinder of radius 2 cm and length 48 cm, centred at  $Z = 0$  of the  
<sup>24</sup> C.M.S detector.
- <sup>25</sup> • **Hadronic barrel and end-cap noise filter**, this filter removes events where  
<sup>26</sup> strips of towers in the hadronic calorimeters record energy from electrical noise,  
<sup>27</sup> mimicking large, unbalanced energy deposits.
- <sup>28</sup> • **Vertex  $p_T/H_T > 0.1$** , removes events where the sum of the  $p_T$  of all tracks from  
<sup>29</sup> all good vertices is less than 10% of the energy deposited by jets in the calorimeters.

1 This cut is designed to remove events with tracking failure, which would otherwise  
 2 pass the calorimeter only event quality requirements.

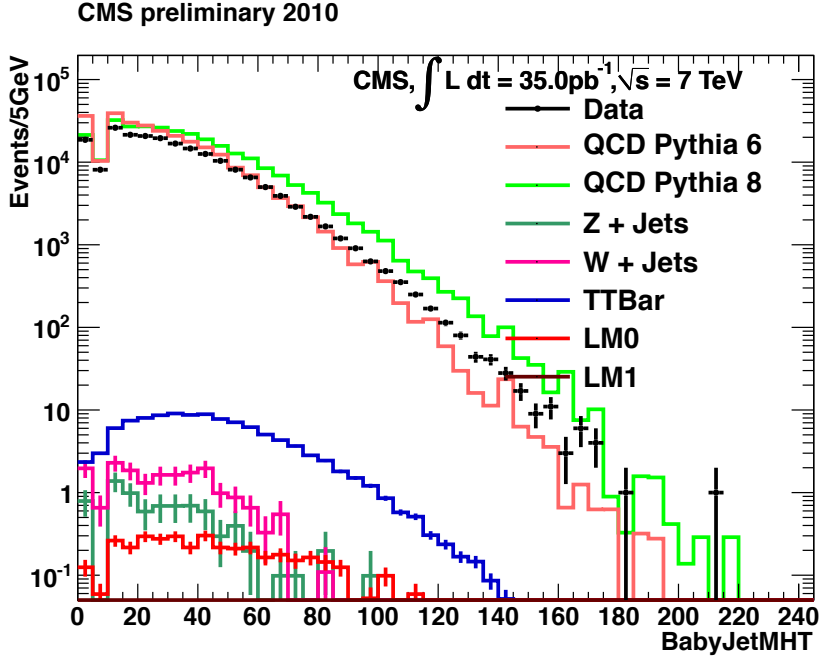
- **Masked ECAL channel filter:** Approximately 1% of the ECAL crystals are masked, or have read out failure. To avoid selecting events with large energy miss measurement, a topological cut was devised. The first step is to calculate  $\Delta\phi^*$  for each jet ( $\vec{j}$ ) in the event, where:

$$\Delta\phi^* = \Delta\phi(\vec{E}_T + \vec{j}, \vec{j}). \quad (6.6)$$

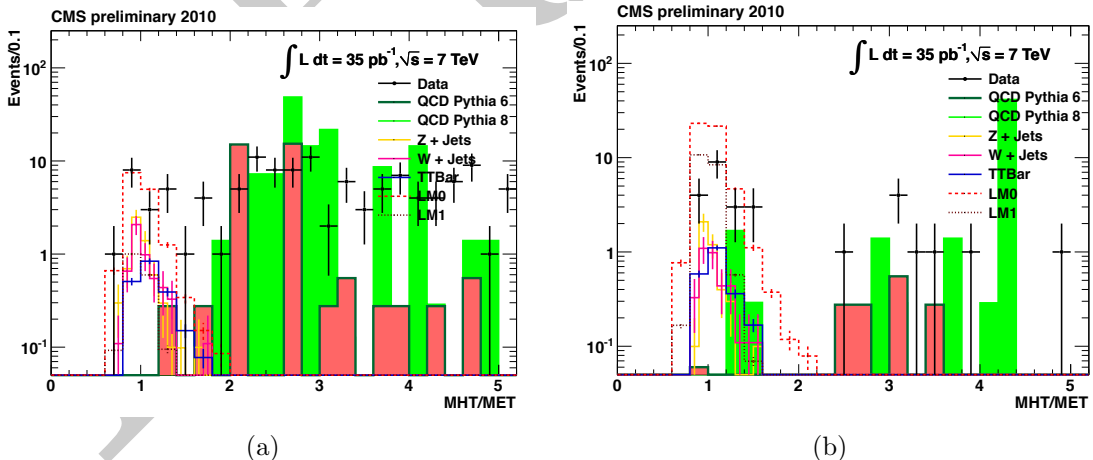
3 Which gives a measure of the miss measurement of a jet, if  $\Delta\phi^*$  is small, the missing  
 4 energy points along the jet in the  $\phi$  direction. By selecting the miss measured jet,  
 5 full position information is preserved. If any jet has  $\Delta\phi^* < 0.5$ , the number of  
 6 masked ECAL crystals with in  $\Delta R < 0.3$  are summed, if there are more than 10  
 7 masked crystals adjacent to the jet, the event is vetoed.

- **$R_{miss} < 1.25$ :** The total hadronic energy in an event is required to be greater than 275 GeV which is well above the transverse energy threshold of 50 GeV for each jet. However several jets falling below this threshold can sum to a significant quantity of ignored energy. This is shown in Figure 6.5, here the missing energy calculated from jets in the range  $10 \text{ GeV} < E_T < 50 \text{ GeV}$  is shown, whilst requiring that  $\cancel{E}_T < 20 \text{ GeV}$ . This shows that for a well balanced event the jets below threshold can carry greater than 100 GeV of ignored energy.  $R_{miss}$  is defined as  $\cancel{H}_T/\cancel{E}_T$  and can be used to single out events where the inclusion of lower momentum jets does significantly improve the balance of the event. Figure 6.6 shows for two  $H_T$  regions the  $R_{miss}$  distribution after the application of the full cut flow, including  $\alpha_T$ , QCD contamination is visible in the signal sample for  $R_{miss} > 1.25$ .

19 This cut flow and set of object definitions define the common selection, on top  
 20 of this an  $\alpha_T$  cut is applied, the passing events are then binned in 8  $H_T$  bins, these  
 21 are 275 GeV - 325 GeV, 325 GeV - 375 GeV, 375 GeV - 475 GeV, 475 GeV - 575 GeV,  
 22 575 GeV - 675 GeV, 675 GeV - 775 GeV, 875 GeV - 7 TeV. However the raw number of  
 23 events in the signal region is meaningless without an accurate background prediction, as  
 24 discussed earlier taking the background estimation from simulation is not viable due to  
 25 the requirement of high order theory calculations on the cross sections of S.M processes  
 26 involving jets, these have many divergencies due to the nature of QCD. Instead the  
 27 simulation is used to form a translation factor between two samples measured in data, a  
 28 control sample which closely mimics the S.M processes producing missing energy, but



**Figure 6.5:**  $\cancel{E}_T$  from jets with  $10 \text{ GeV} < E_T < 50 \text{ GeV}$  in events with  $H_T > 350 \text{ GeV}$  and  $\cancel{E}_T < 20 \text{ GeV}$  in  $35 \text{ pb}^{-1}$  of data.



**Figure 6.6:** (a)  $R_{miss}$  distribution for events in the  $250 \text{ GeV} < H_T < 350 \text{ GeV}$  region, where due to the low  $H_T$  requirement QCD contamination is enriched.  
(b)  $R_{miss}$  distribution for events in the  $H_T > 350 \text{ GeV}$  region, QCD contamination occurs at  $R_{miss} > 1.25$ .

<sup>1</sup> has a visible muon or photon in the final state. The background estimation methods  
<sup>2</sup> are described and the background predictions stated in Section 7.1. The next section  
<sup>3</sup> describes the triggers used to collect the data samples

## <sup>4</sup> 6.4 High Level triggers for the $\alpha_T$ analysis

<sup>5</sup> The CMS trigger system has been discussed in detail in Section 3.7 and Chapter 4,  
<sup>6</sup> however details of analysis specific trigger paths were not discussed. During 2011 the  
<sup>7</sup> first  $\alpha_T$  specific trigger was designed and deployed online. The trigger was then upgraded  
<sup>8</sup> for the higher luminosity and energy conditions of the 2012 data taking period.

<sup>9</sup> The trigger takes advantage of cutting on two variables,  $H_T$  and  $\alpha_T$  at low  $H_T$  a high  
<sup>10</sup>  $\alpha_T$  value cuts the trigger rate, where as at high  $H_T$  where the trigger rate is lower the  
<sup>11</sup>  $\alpha_T$  requirement can be loosened.

<sup>12</sup> Due to the scaling of jet thresholds in the lowest offline  $H_T$  bins as detailed in  
<sup>13</sup> Section 6.2 using a fixed jet threshold would cause inefficiency in the lowest offline  $H_T$   
<sup>14</sup> bins. To over come this the trigger level  $\alpha_T$  calculation is performed iteratively for all  
<sup>15</sup> jets above a predefined threshold. This raises the total number of accepted events whilst  
<sup>16</sup> adding the benefit of being efficient for any offline jet threshold above the minimum  
<sup>17</sup> trigger jet threshold.

<sup>18</sup> Due to concerns on the time taken to perform the  $\Delta H_T$  minimisation at the trigger  
<sup>19</sup> and time constraints enforced on trigger menu development, the first implementation  
<sup>20</sup> calculates  $\alpha_T$  for the first 3 jets. For higher jet multiplicities the variable  $\beta_T$  is calculated.

$$\beta_T = \frac{H_T}{2\sqrt{H_T^2 - \cancel{H}_T^2}} \quad (6.7)$$

this gives us the relation:

$$\alpha_T \leq \beta_T. \quad (6.8)$$

<sup>21</sup> The decision flow is shown in Figure 6.7 and explained in detail below.

<sup>22</sup> When a level one accept is issued the trigger bits that fired are checked, if the  
<sup>23</sup> event fires a L1 muon trigger it is passed to the HLT muon triggers where only muon

reconstruction is performed, reducing the reconstruction time. The  $\alpha_T$  triggers are seeded on the lowest threshold unprescaled L1  $H_T$  trigger, during 2011 this was L1\\_HTT100. Any events issuing a L1 accept and passing L1\\_HTT100 undergo calorimeter jet reconstruction, the reconstruction algorithm is detailed in Section 6.2.1.

Once the jets have been formed the trigger filter is entered. Initially the first two jets ranked by  $E_T$ , are considered,  $H_T$  and  $\alpha_T$  are calculated, if both pass the trigger thresholds the event is accepted and the full detector read out is performed. If either  $H_T$  or  $\alpha_T$  is below threshold, the next jet in  $E_T$  order is added, if the jet collection contains more than 3 jets then the  $\beta_T$  approximation is used. All jets in the event are added until either the event is accepted, or there are no more jets to be added above 40 GeV.

The effect of switching to the  $\beta_T$  approximation is to accept events that have missing energy due to miss-measurement, when calculating  $\alpha_T$  offline these events have values of  $\alpha_T < 0.5$ . This introduces an impurity to the trigger and costs rate for events that will not be considered in the offline analysis.

#### 6.4.1 Trigger efficiency measurement

The performance of the  $\alpha_T$  trigger suit is measured with respect to a sample collected using the muon system. This allows the measurement of efficiency of both the level one seed trigger and the higher level trigger at the same time as different sub-systems are used to collect the reference and the signal triggers. This is due to the exclusive use of calorimeter jets in the  $\alpha_T$  trigger, if more complicated reconstruction methods which produce an event hypothesis were used, muons would at HLT level only be considered as jets. Whereas during calorimeter only reconstruction, muons are not considered and the  $p_T$  of any muons in an event is viewed as missing energy.

The selection for the trigger efficiency measurement is the same as listed in Section 6.2 with the requirement of exactly one well identified muon with  $p_T > 45$  GeV, the sum of the  $\cancel{E}_T$  in the event and the muon must add to the W mass and finally the muon must be separated by at least 0.5 in  $\Delta R$  to the closest jet, to avoid the muon energy changing the energy of the jet offline when the cross cleaning is applied.

Due to the increase in luminosity over the running period the trigger thresholds were increased, to ensure constant rate though out the year and the trigger version numbers were increased each time the trigger menu was updated. The list of triggers considered and their reference triggers are listed in Tables 6.1 and 6.2.

1       The efficiency of each trigger version is measured in the required  $H_T$  bins, the total  
2       efficiency for each  $H_T$  bin is then calculated by combining the individual efficiencies  
3       using a weighted sum based on the fraction of the total luminosity of the sample that  
4       each version carries. This accounts for the change in running conditions during the data  
5       taking period and the criteria that the trigger suite takes constant rate. The higher  
6       trigger versions and thresholds generally represent more integrated luminosity due to the  
7       evolution of running conditions with time.

8       The efficiency is measured as a function of the cumulative number of events, ie the  
9       efficiency at each point on the x axis is the measured efficiency if a cut were applied  
10      offline at that cut value.

11      As an example, the efficiency of each trigger used in the  $275 \text{ GeV} < H_T < 325 \text{ GeV}$   
12      bin is measured and then combined to give the total efficiency. The cumulative efficiency  
13      curves for each trigger seeding the lowest bin is show in Figures 6.8, 6.9 & 6.10. Note  
14      that some of the triggers are repeated, due to the reference trigger version incrementing  
15      and the signal trigger not.

16      These are then combined to give Figure 6.11 the efficiency at a cut of  $\alpha_T > 0.55$   
17      is  $83.3\% + 0.5\% - 0.6\%$ . The loss in efficiency comes from the disparity between the  
18      minimum thresholds for jets to enter the  $H_T$  and  $\alpha_T$  calculations at the HLT and those  
19      used in the analysis. The trigger jet  $E_T$  threshold is 40 GeV where as the analysis jet  
20       $E_T$  threshold in this bin is  $36 \cdot 6$  GeV. The triggers used to take data at the end of this  
21      running period also have an  $\alpha_T$  threshold above the analysis cut of  $\alpha_T > 0.55$ , which  
22      again causes an inefficiency. The list of efficiencies for each  $H_T$  bin are shown in Table 6.3.  
23      The trigger efficiencies are measured to better than one percent and this information  
24      is used in the final likelihood model, to correct the expected numbers from simulation  
25      when calculating the translation factors.

26      The  $\alpha_T$  triggers were upgraded for the increased instantaneous luminosity and pile up  
27      conditions expected during the 2012 data taking period. The first stage was to implement  
28      the full  $\alpha_T$  calculation for each addition of a new jet, this change increases the purity of  
29      the trigger, meaning that for the same threshold the rate taken is lower than that of the  
30      previous algorithm. This allows the thresholds to be kept low, whilst not increasing the  
31      overall trigger rate.

Offline $H_T$ bin	Signal Trigger	Reference Trigger
$275 \text{ GeV} < H_T < 325 \text{ GeV}$	HLT-HT250_AlphaT0p53_v2	HLT_Mu15_HT200_v2
$275 \text{ GeV} < H_T < 325 \text{ GeV}$	HLT-HT250_AlphaT0p53_v3	HLT_Mu15_HT200_v3
$275 \text{ GeV} < H_T < 325 \text{ GeV}$	HLT-HT250_AlphaT0p53_v4	HLT_Mu15_HT200_v4
$275 \text{ GeV} < H_T < 325 \text{ GeV}$	HLT-HT250_AlphaT0p53_v5	HLT_Mu30_HT200_v1
$275 \text{ GeV} < H_T < 325 \text{ GeV}$	HLT-HT250_AlphaT0p55_v1	HLT_Mu5_HT200_v4
$275 \text{ GeV} < H_T < 325 \text{ GeV}$	HLT-HT250_AlphaT0p55_v2	HLT_Mu40_HT200_v4
$275 \text{ GeV} < H_T < 325 \text{ GeV}$	HLT-HT250_AlphaT0p58_v3	HLT_DoubleMu8_Mass8_HT200_v4
$275 \text{ GeV} < H_T < 325 \text{ GeV}$	HLT-HT250_AlphaT0p58_v3	HLT_DoubleMu8_Mass8_HT200_v5
$275 \text{ GeV} < H_T < 325 \text{ GeV}$	HLT-HT250_AlphaT0p60_v3	HLT_DoubleMu8_Mass8_HT200_v4
$275 \text{ GeV} < H_T < 325 \text{ GeV}$	HLT-HT250_AlphaT0p60_v3	HLT_DoubleMu8_Mass8_HT200_v5
$325 \text{ GeV} < H_T < 375 \text{ GeV}$	HLT-HT300_AlphaT0p52_v1	HLT_Mu5_HT200_v4
$325 \text{ GeV} < H_T < 375 \text{ GeV}$	HLT-HT300_AlphaT0p52_v2	HLT_Mu8_HT200_v4
$325 \text{ GeV} < H_T < 375 \text{ GeV}$	HLT-HT300_AlphaT0p52_v3	HLT_Mu15_HT200_v2
$325 \text{ GeV} < H_T < 375 \text{ GeV}$	HLT-HT300_AlphaT0p53_v3	HLT_Mu15_HT200_v3
$325 \text{ GeV} < H_T < 375 \text{ GeV}$	HLT-HT300_AlphaT0p53_v4	HLT_Mu15_HT200_v4
$325 \text{ GeV} < H_T < 375 \text{ GeV}$	HLT-HT300_AlphaT0p53_v5	HLT_Mu30_HT200_v1
$325 \text{ GeV} < H_T < 375 \text{ GeV}$	HLT-HT300_AlphaT0p53_v6	HLT_Mu40_HT200_v3
$325 \text{ GeV} < H_T < 375 \text{ GeV}$	HLT-HT300_AlphaT0p53_v6	HLT_Mu40_HT200_v4
$325 \text{ GeV} < H_T < 375 \text{ GeV}$	HLT-HT300_AlphaT0p54_v5	HLT_Mu40_HT300_v4
$325 \text{ GeV} < H_T < 375 \text{ GeV}$	HLT-HT300_AlphaT0p54_v5	HLT_Mu40_HT300_v5
$325 \text{ GeV} < H_T < 375 \text{ GeV}$	HLT-HT300_AlphaT0p55_v3	HLT_DoubleMu8_Mass8_HT200_v4
$325 \text{ GeV} < H_T < 375 \text{ GeV}$	HLT-HT300_AlphaT0p55_v3	HLT_DoubleMu8_Mass8_HT200_v5

**Table 6.1:** List of  $\alpha_T$  triggers used in the lowest two offline  $H_T$  bins and the triggers used to collect the reference sample.

Offline $H_T$ bin	Signal Trigger	Reference Trigger
$375 \text{ GeV} < H_T < 475 \text{ GeV}$	HLT-HT350_AlphaT0p51_v1	HLT_Mu5_HT200_v4
$375 \text{ GeV} < H_T < 475 \text{ GeV}$	HLT-HT350_AlphaT0p51_v2	HLT_Mu8_HT200_v4
$375 \text{ GeV} < H_T < 475 \text{ GeV}$	HLT-HT350_AlphaT0p51_v3	HLT_Mu15_HT200_v2
$375 \text{ GeV} < H_T < 475 \text{ GeV}$	HLT-HT350_AlphaT0p51_v4	HLT_Mu15_HT200_v3
$375 \text{ GeV} < H_T < 475 \text{ GeV}$	HLT-HT350_AlphaT0p51_v5	HLT_Mu15_HT200_v4
$375 \text{ GeV} < H_T < 475 \text{ GeV}$	HLT-HT350_AlphaT0p52_v1	HLT_Mu30_HT200_v1
$375 \text{ GeV} < H_T < 475 \text{ GeV}$	HLT-HT350_AlphaT0p52_v2	HLT_Mu40_HT200_v3
$375 \text{ GeV} < H_T < 475 \text{ GeV}$	HLT-HT350_AlphaT0p52_v2	HLT_Mu40_HT200_v4
$375 \text{ GeV} < H_T < 475 \text{ GeV}$	HLT-HT350_AlphaT0p53_v10	HLT_Mu40_HT300_v4
$375 \text{ GeV} < H_T < 475 \text{ GeV}$	HLT-HT350_AlphaT0p53_v10	HLT_Mu40_HT300_v5
$475 \text{ GeV} < H_T < 7 \text{ TeV}$	HLT-HT400_AlphaT0p51_v1	HLT_Mu5_HT200_v4
$475 \text{ GeV} < H_T < 7 \text{ TeV}$	HLT-HT400_AlphaT0p51_v2	HLT_Mu8_HT200_v4
$475 \text{ GeV} < H_T < 7 \text{ TeV}$	HLT-HT400_AlphaT0p51_v3	HLT_Mu15_HT200_v2
$475 \text{ GeV} < H_T < 7 \text{ TeV}$	HLT-HT400_AlphaT0p51_v4	HLT_Mu15_HT200_v3
$475 \text{ GeV} < H_T < 7 \text{ TeV}$	HLT-HT400_AlphaT0p51_v5	HLT_Mu15_HT200_v4
$475 \text{ GeV} < H_T < 7 \text{ TeV}$	HLT-HT400_AlphaT0p51_v6	HLT_Mu30_HT200_v1
$475 \text{ GeV} < H_T < 7 \text{ TeV}$	HLT-HT400_AlphaT0p51_v7	HLT_Mu40_HT200_v3
$475 \text{ GeV} < H_T < 7 \text{ TeV}$	HLT-HT400_AlphaT0p51_v7	HLT_Mu40_HT200_v4
$475 \text{ GeV} < H_T < 7 \text{ TeV}$	HLT-HT400_AlphaT0p51_v10	HLT_Mu40_HT300_v4
$475 \text{ GeV} < H_T < 7 \text{ TeV}$	HLT-HT400_AlphaT0p51_v10	HLT_Mu40_HT300_v5
$475 \text{ GeV} < H_T < 7 \text{ TeV}$	HLT-HT400_AlphaT0p52_v5	HLT_Mu40_HT300_v4
$475 \text{ GeV} < H_T < 7 \text{ TeV}$	HLT-HT400_AlphaT0p52_v5	HLT_Mu40_HT300_v5

**Table 6.2:** List of  $\alpha_T$  triggers used in the  $H_T > 375 \text{ GeV}$  bins and the triggers used to collect the reference sample.

$H_T$ range (GeV)	Trigger efficiency (%)
275–325	$83.3^{+0.5}_{-0.6}$
325–375	$95.9^{+0.7}_{-0.9}$
375–475	$98.5^{+0.5}_{-0.9}$
475– $\infty$	$100.0^{+0.0}_{-4.8}$

**Table 6.3:** Efficiencies of the  $\alpha_T$  triggers used in the 7 TeV  $\alpha_T$  analysis on  $5 \text{ fb}^{-1}$  of LHC data.

$H_T$ range	Trigger
275 GeV–325 GeV	HLT-HT250_AlphaT0p55_v*
325 GeV–375 GeV	HLT-HT300_AlphaT0p53_v*
375 GeV–475 GeV	HLT-HT350_AlphaT0p52_v*
475 GeV–8 TeV	HLT-HT400_AlphaT0p51_v*

**Table 6.4:** Triggers used to seed the analysis  $H_T$  bins during 2012 data taking.

<sup>1</sup> The second upgrade was to switch to pile up corrected jets at the HLT, this change  
<sup>2</sup> keeps the trigger cross section liner as a function of instantaneous luminosity.

<sup>3</sup> The third choice was to design a trigger suite that could run for the entire 2012  
<sup>4</sup> data taking period, with out changing the trigger thresholds, this was done to make the  
<sup>5</sup> measurement of the efficiency simpler.

<sup>6</sup> The trigger thresholds used are presented in Table 6.4, due to the constant thresholds  
<sup>7</sup> in  $H_T$  and  $\alpha_T$  though out the run, the versioning of the triggers is excluded from this  
<sup>8</sup> table. The efficiency of the triggers is measured for  $11.7 \text{ fb}^{-1}$  of LHC data taken at a  
<sup>9</sup> centre of mass energy of 8 TeV the efficiencies were measured for the analysis presented  
<sup>10</sup> at HCP, documented in [8]. A single muon trigger is used to collect the reference sample,  
<sup>11</sup> the threshold of this trigger was unchanged during the data taking period, the path  
<sup>12</sup> selected is HLT\_IsoMu24\_v\* which requires at least one muon with  $p_T > 24 \text{ GeV}$  that is  
<sup>13</sup> not over lapping with any other object in the detector. The same method is used as for  
<sup>14</sup> the 2011 trigger efficiency measurement. However the offline jets are corrected for pile  
<sup>15</sup> up using the fast jet corrections, to stay inline with the HLT object definitions.

<sup>16</sup> Figure 6.12 shows the efficiencies of the four individual triggers that seed the 275 GeV–  
<sup>17</sup> 325 GeV  $H_T$  bin for  $11.7 \text{ fb}^{-1}$  of 8 TeV LHC data, Figure 6.13 shows the combined  
<sup>18</sup> cumulative efficiency of the 2012 trigger suite.

<sup>19</sup> The two trigger suites have very similar offline performance with 100% efficiency  
<sup>20</sup> in the analysis bins above 475 GeV and high efficiency in the lower bins. To quantify  
<sup>21</sup> the difference in performance between the two algorithms the purity is defined as the  
<sup>22</sup> number of events passing the trigger that pass the offline  $\alpha_T$  requirement at the same  
<sup>23</sup> threshold as the trigger requirement divided by the total number of events accepted by  
<sup>24</sup> the trigger. The purity of each trigger algorithm is measured for an example trigger with  
<sup>25</sup> a  $H_T$  threshold of 350 GeV and an  $\alpha_T$  threshold of 0.52. The 2011 trigger which only

$H_T$ range (GeV)	Trigger efficiency (%)
275 GeV – 325 GeV	$89.6^{+0.4}_{-0.4}$
325 GeV – 375 GeV	$98.6^{+0.2}_{-0.3}$
375 GeV – 475 GeV	$99.4^{+0.2}_{-0.3}$
475 GeV – 8 TeV	$100.0^{+0.0}_{-0.5}$

**Table 6.5:** Efficiencies of the  $\alpha_T$  triggers at a centre of mass energy of 8 TeV  $\alpha_T$  measured in  $11.7 \text{ fb}^{-1}$  of LHC data.

1 performs the full  $\alpha_T$  calculation for jet multiplicities of less than four has a purity of  
 2 48%, which means a quarter of all rate taken by the trigger is used in the offline analysis.  
 3 The 2012 trigger which performs the full  $\alpha_T$  calculation for all jet multiplicities has a  
 4 purity of 75%. This 25% increase in purity translates in to a 25% rate reduction for the  
 5 same trigger threshold when changing to the full  $\alpha_T$  calculation for all jet multiplicities,  
 6 thus enabling the trigger thresholds to be kept at the same or lower thresholds in the  
 7 2012 run as in the 2011 run.

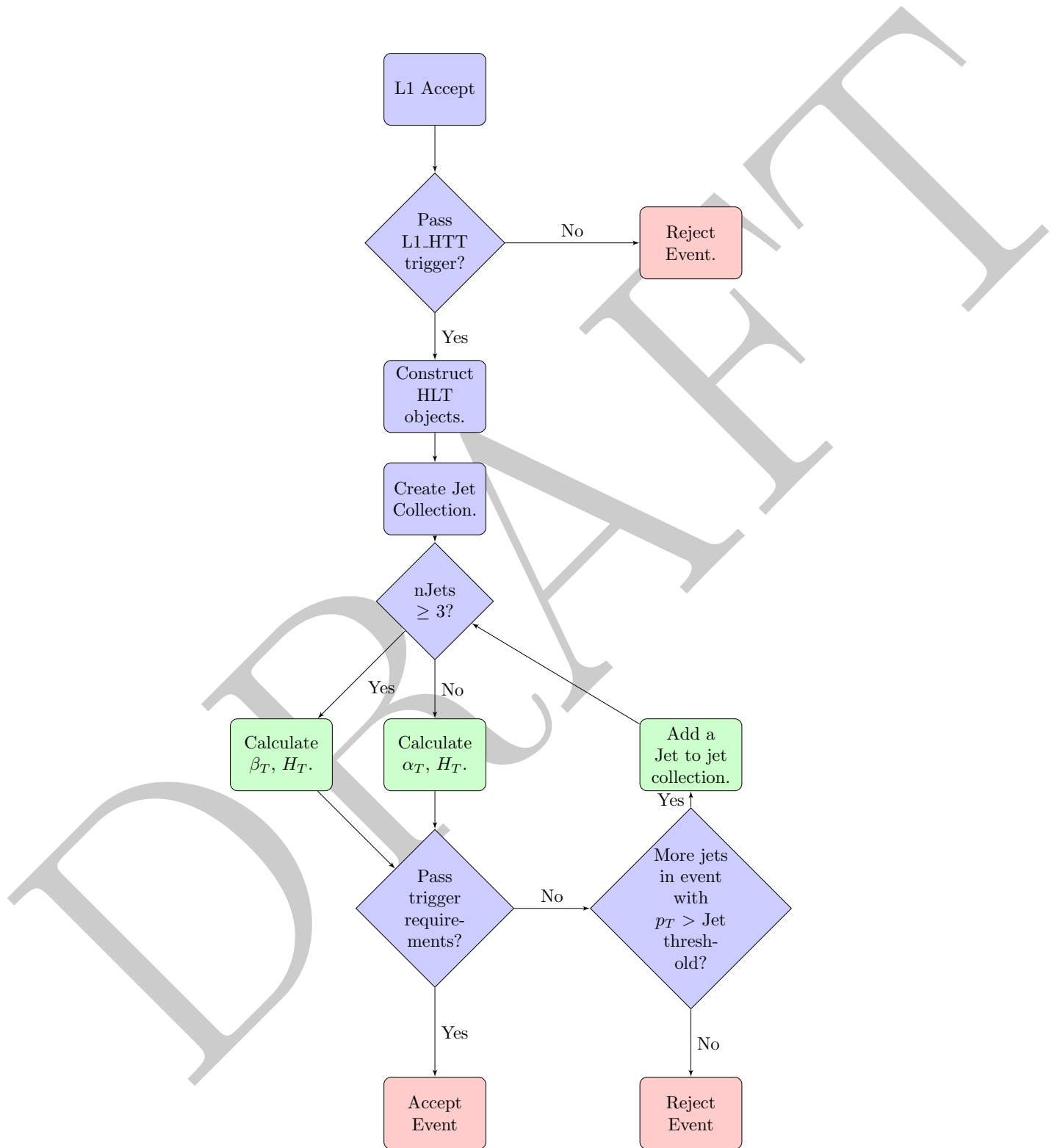
## 8 **6.5 Extension to higher analysis dimensions.**

### 9 **B-tagging**

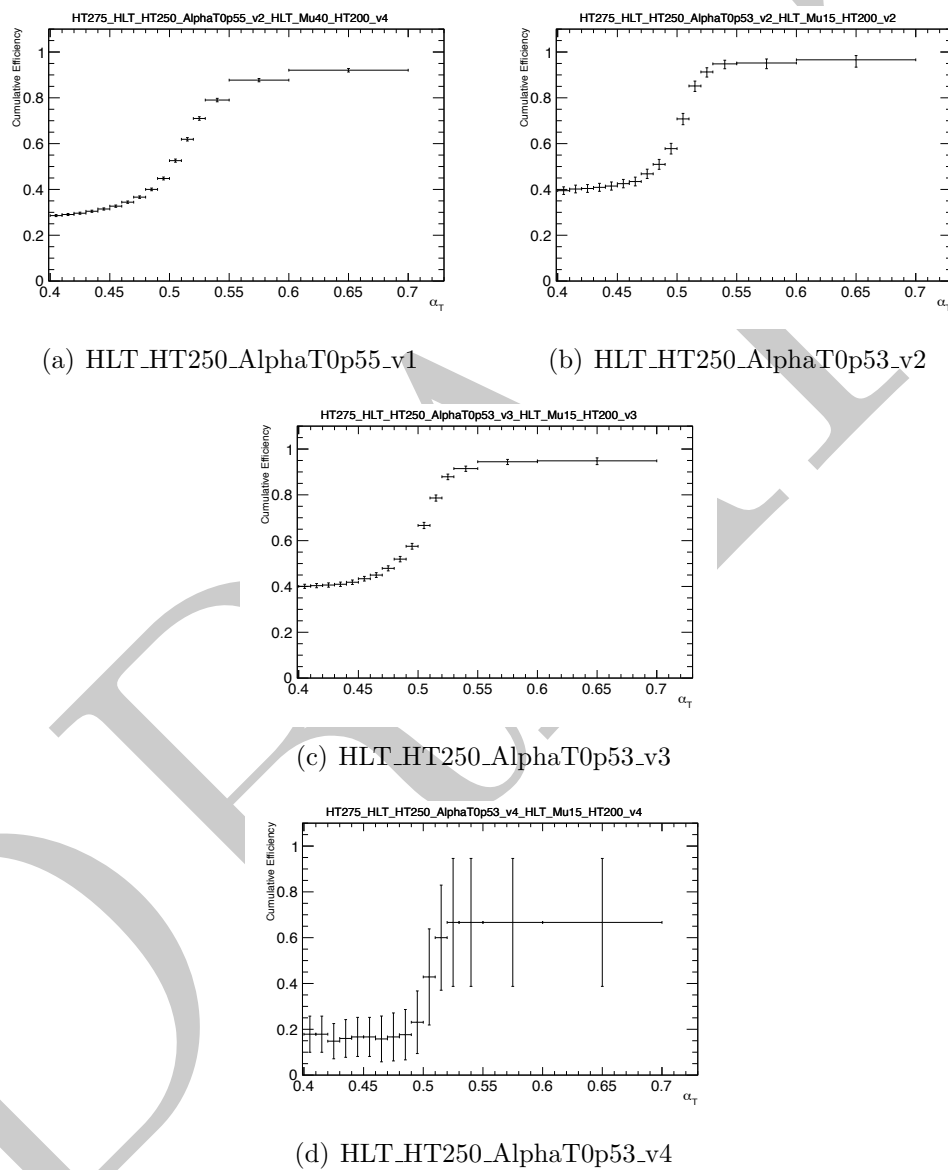
10 **Declaration** Whilst it should be noted that the author did not contribute towards  
 11 the extension of the analysis to include a dimension based on the measurement of the  
 12 number of jets containing b quarks in the final state, the final analysis does include this  
 13 extension, hence the b-tagging procedure is explained in sufficient detail as to understand  
 14 the process but not to elude to all the nuances of the method in the following section.

15 Jets are tagged as originating from a b decay via the identification of a displaced  
 16 vertex as it takes the b a finite amount of time to decay, during this time the quark  
 17 which is not produced at rest travels away from the initial interaction point, where upon  
 18 decaying a secondary decay vertex is created. The algorithm used to classify these jets as  
 19 containing a b quark is the Combined Secondary Vertex (C.S.V) tagger. The “Medium”  
 20 working point is used in the analysis, which requires a cut of  $> 0.679$  on the C.S.V  
 21 value. This results in a gluon/light quark miss tag rate of 1% where “light” quarks are  
 22 u, d and s types. The efficiency for tagging b quark jets in the range 60 – 70%[19] is  
 23 achieved, this efficiency depends on the jet  $p_T$ . The discriminator is supported by the

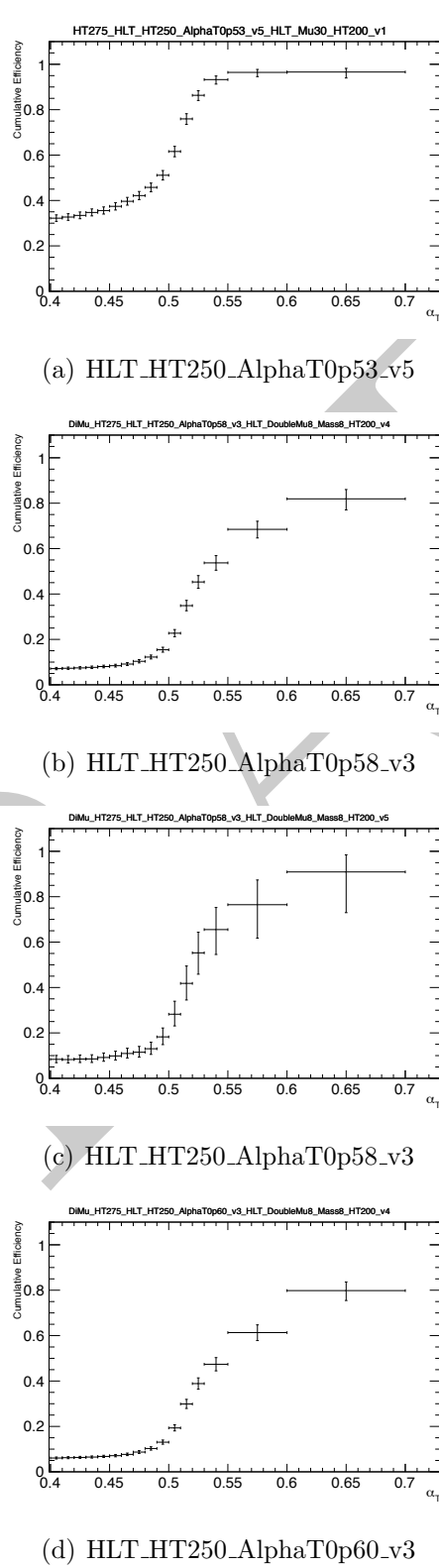
- <sup>1</sup> C.M.S b physics object group[4] and its performance is well understood. The Montecarlo  
<sup>2</sup> miss tag and identification rates are re-weighted to agree with data observations, thus  
<sup>3</sup> provide an accurate background prediction for the high multiplicity b-tagged bins which  
<sup>4</sup> are dominated by the miss tag of light quarks as b quarks.



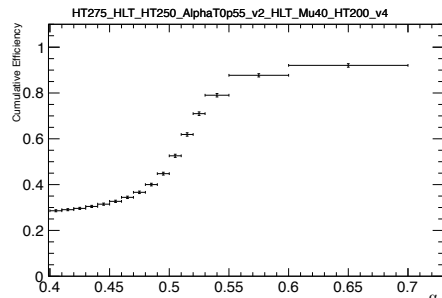
**Figure 6.7:** Flow chart representing the steps taken to make a trigger decision using the  $\alpha_T$  trigger algorithm.



**Figure 6.8:** Turn on curves for the individual  $\alpha_T$  triggers used to seed the  $275 \text{ GeV} < H_T < 325 \text{ GeV}$  bin.

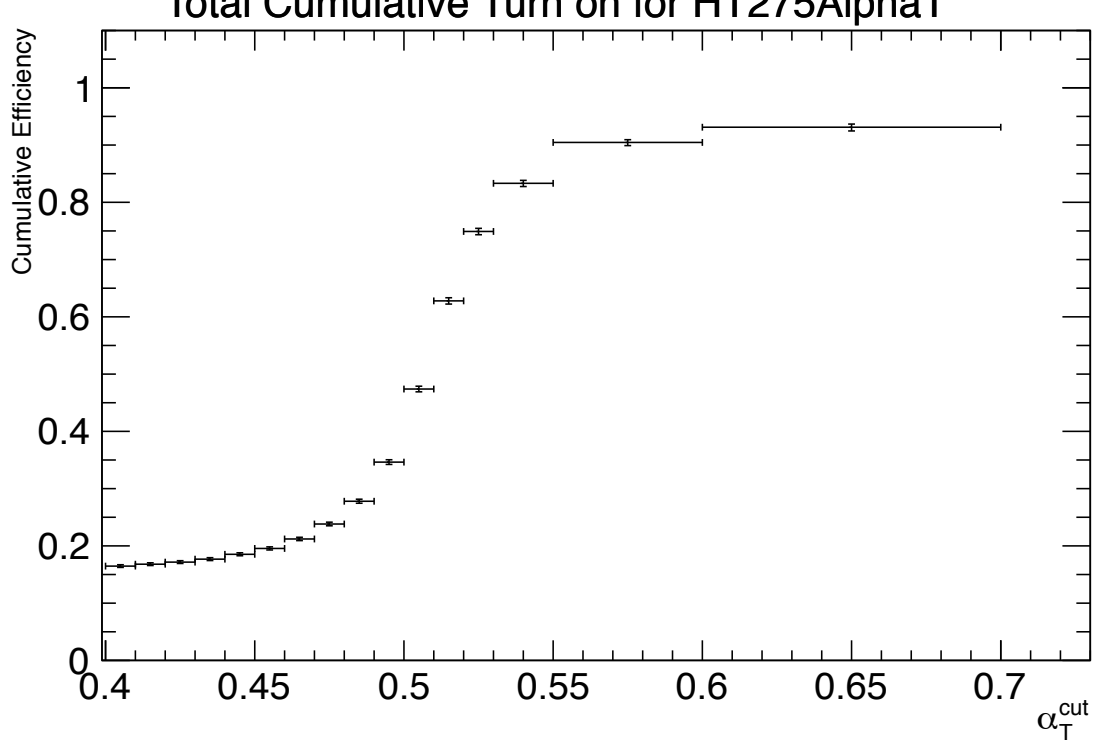


**Figure 6.9:** Turn on curves for the individual  $\alpha_T$  triggers used to seed the  $275 \text{ GeV} < H_T < 325 \text{ GeV}$  bin.

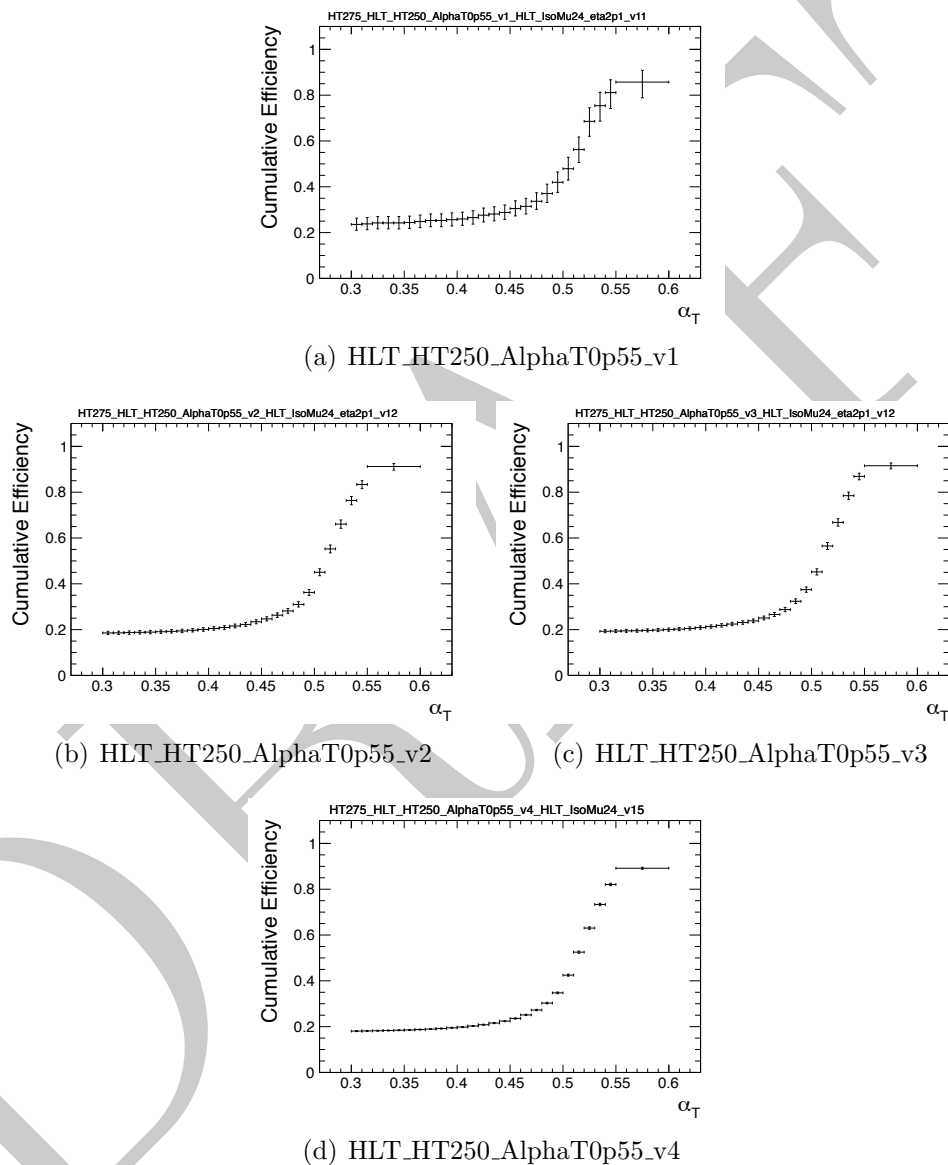


(a) HLT-HT250-AlphaT0p60-v3

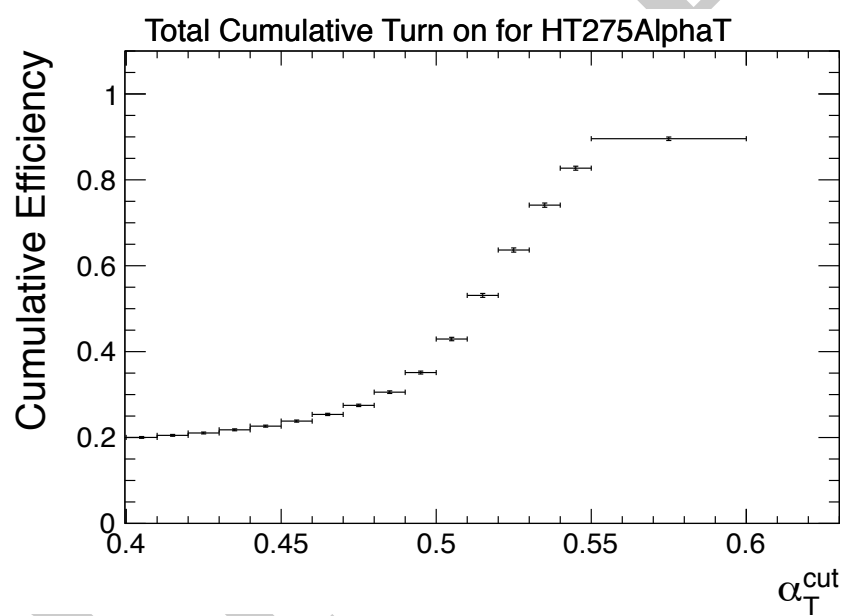
**Figure 6.10:** Turn on curves for the individual  $\alpha_T$  triggers used to seed the  $275 \text{ GeV} < H_T < 325 \text{ GeV}$  bin.



**Figure 6.11:** Combined cumulative efficiency for the triggers seeding the  $275 \text{ GeV} < H_T < 325 \text{ GeV}$  offline analysis bin.



**Figure 6.12:** Turn on curves for the individual  $\alpha_T$  triggers used to seed the  $275 \text{ GeV} < H_T < 325 \text{ GeV}$  bin, during 2012 data taking.



**Figure 6.13:** Combined cumulative efficiency for the triggers seeding the  $275 \text{ GeV} < H_T < 325 \text{ GeV}$  offline bin for  $11.7 \text{ fb}^{-1}$  of 8 TeV LHC data.

# Chapter 7

## <sup>1</sup> Background Prediction

### <sup>2</sup> 7.1 Electro-Weak Background Prediction

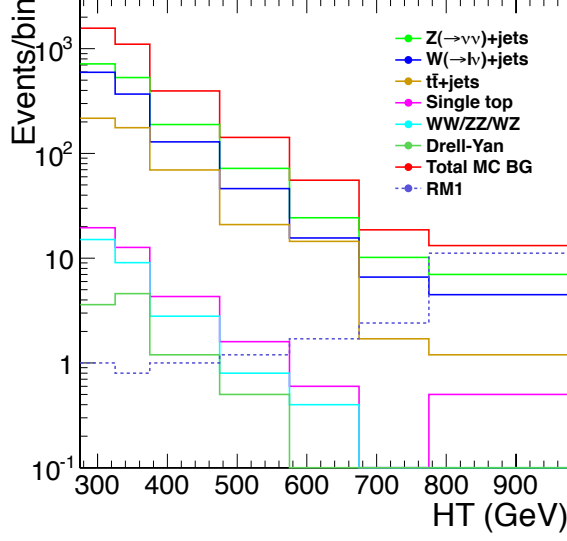
<sup>3</sup> The requirement of an  $\alpha_T$  cut on the signal sample removes multi-jet QCD events where a  
<sup>4</sup> balanced event is counted as signal due to miss-measurements, the remaining background  
<sup>5</sup> events in the signal region are due to electro-weak processes which produce real missing  
<sup>6</sup> energy. Primarily these events are produced from  $Z \rightarrow \nu\bar{\nu} + \text{Jets}$ ,  $W \rightarrow \ell\bar{\nu} + \text{Jets}$  and  
<sup>7</sup>  $t\bar{t}$  decay, with smaller contributions from Drell-Yan + Jets, single top production in the  
<sup>8</sup> s,t and tW channels and from di-boson + Jet events. To predict the number of these  
<sup>9</sup> events contributing to the number of signal like events three control samples are defined  
<sup>10</sup> and though the use of a Montecarlo derived transfer factor the control samples are used  
<sup>11</sup> to predict the number of S.M events expected in the signal region.

<sup>12</sup> Figure 7.1[6] shows the expectation from simulation in all bins of the hadronic signal  
<sup>13</sup> region, for the different background samples and an example CMSSM reference model  
<sup>14</sup> RM1.

<sup>15</sup> Explain what RM1 is

<sup>16</sup> The expected composition of the the backgrounds in the hadronic signal region, as a  
<sup>17</sup> percentage of the total S.M background, are summarised in Table 7.1.  $Z \rightarrow \nu\nu$  contributes  
<sup>18</sup>  $\approx 43\%$  of the S.M background in the 275 GeV–325 GeV  $H_T$  bin, raising to  $\approx 53\%$  in the  
<sup>19</sup>  $H_T > 875$  GeV bin. Events entering the signal region due to Z or W decays where the  
<sup>20</sup> lepton is missed by the lepton vetoes account for  $\approx 25\%$  at low  $H_T$  and  $\approx 13\%$  at high  $H_T$ .  
<sup>21</sup> Events from hadronically decays  $\tau$  ( $\tau_h$ ) have a low  $H_T$  dependance, contributing  $\approx 22\%$   
<sup>22</sup> of the background at low  $H_T$  and  $\approx 27\%$  of the background at high  $H_T$ . Those events

- <sup>1</sup> arising from  $\tau$  particles which decay leptonically ( $\tau_l$ ) and are missed by the lepton vetoes  
<sup>2</sup> account for  $\approx 10\%$  of the S.M background.



**Figure 7.1:** Expectation from MC in all bins of the hadronic signal region for the following different background processes:  $Z \rightarrow \nu\nu + \text{jets}$ ,  $W + \text{jets}$ ,  $t\bar{t}$ , single top + jets, di-boson production ( $WW/WZ/ZZ$ ), and Drell-Yan. The total SM expectation is also shown, along with that for the CMSSM benchmark model RM1.

**Table 7.1:** Relative background composition as given by MC simulation in all bins of the hadronic signal region (expressed as a percentage of the total SM background).

$H_T$ GeV	N <sub>events</sub>	$Z \rightarrow \nu\nu + \text{jets}$ (%)	W + jets, $t\bar{t}$ , single top, DY and di-boson			
			missed e, $\mu$ from W/Z (%)	$\tau_h$ (%)	$\tau_l$ (%)	$\tau_h$ matched to jet (%)
275–325	3938.0	43	24	22	11	7
325–375	1569.9	46	25	22	9	7
375–475	1104.2	48	20	23	10	7
475–575	396.0	48	17	24	11	10
575–675	142.4	51	17	23	10	11
675–775	55.5	44	19	31	7	17
775–875	18.7	55	17	22	4	9
875– $\infty$	13.2	53	13	27	7	19

- <sup>3</sup> To calculate the bin by bin translation factors the signal selection and the individual  
<sup>4</sup> control selections are applied to the montecarlo simulated background samples. The ratio

of the number of accepted events is then taken, the signal yield prediction is computed from applying the control selections to real data and multiplying the event yield by the translation factor. The measurements from all control samples are considered simultaneously in a fit defined in Section 7.4. This method can be extended to high dimensions of analysis bins, for example in [8] a secondary dimension involving the number of B quarks in the event is studied. However the B extension is not detailed in this thesis.

$$N_{\text{prediction}}^{\text{sig}}(H_T) = N_{\text{obs}}^{\text{control}}(H_T) \times \frac{N_{MC}^{\text{sig}}(H_T)}{N_{MC}^{\text{control}}(H_T)} \quad (7.1)$$

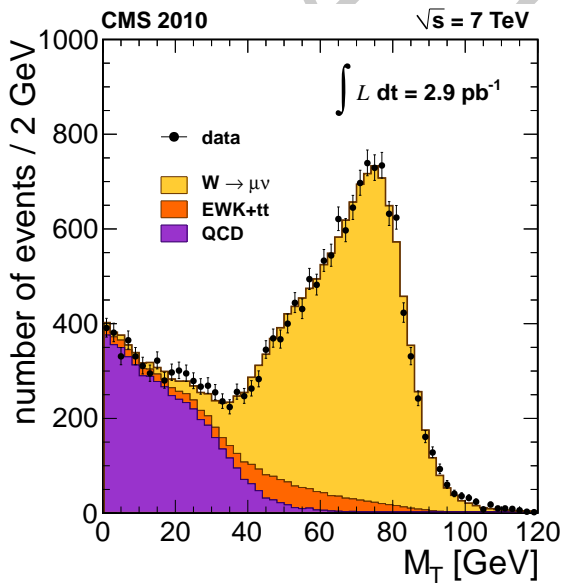
The three control samples used are a  $W \rightarrow \mu\nu + \text{Jets}$  sample, a  $Z \rightarrow \mu\mu + \text{Jets}$  sample and a  $\gamma + \text{Jets}$  sample.

The selection criteria for each of these control samples is kept as similar to the signal selection as possible, so as to not introduce systematic errors from incorrect modelling in the simulation. The use of the ratio of the number of observed events in the montecarlo cancels the systematic effects. A systematic is still assigned to each translation factor to account for theoretical uncertainties and acceptance and instrumental effects.

Additional kinematic cuts are applied in the two muon control samples to enrich the  $W + \text{Jets}$   $t\bar{t}$  and  $Z + \text{Jets}$  components in the control samples. The samples are defined to maximised efficiency rather than purity, any impurities are accounted for in the transfer factors as the yields from all montecarlo samples are used. This is valid under the assumption that the S.M electro-weak and Drell-Yan processes are well modelled by the simulation. The possibility of SUSY like signal contamination in the control samples is accounted for in the final likelihood, after measuring the signal acceptance for the control samples on simulated SUSY events.

The magnitude of the systematic uncertainties on the transfer factors is motivated by a set of closure tests between the control samples. A transfer factor is produced to predict each control sample from each of the other control samples. No assumed systematic is applied in these closure tests, instead the level of agreement with in statistical uncertainty is used to set the scale of the systematic error for each  $H_T$  bin.

**1 The  $\mu + \text{Jets}$  control sample** The  $\mu + \text{Jets}$  control sample is designed to mimic  
 2 the events appearing in the signal region due to  $W + \text{Jets}$  and  $t\bar{t}$  decays where the  
 3 leptons are missed offline, either due to falling out of acceptance or being missed by  
 4 the reconstruction algorithms. Hadronic tau decays from high  $p_T$   $W$  bosons are also  
 5 predicted from this sample. The additional selection criteria for this sample are designed  
 6 to select events containing the decay  $W \rightarrow \mu\nu + \text{Jets}$  in the same kinematic conditions  
 7 as those events entering the signal selection. Offline the event level discriminators,  $H_T$   
 8 and  $\alpha_T$ , are calculated using only the hadronic components of the event. In order to  
 9 select the  $W$  exactly one tightly identified, isolated muon with  $|\eta| < 2.5$  with  $p_T >$   
 10  $10 \text{ GeV}$  is required. The transverse mass of the muon combined with the missing energy  
 11 of the event  $M_T(\mu, \cancel{E}_T)$  is required to be larger than  $30 \text{ GeV}$ , as shown in Figure 7.2 the  
 12 transverse mass cut removes a large amount of QCD whilst preserving a high efficiency  
 13  $W$  selection. Events are vetoed if for any jet  $\Delta R(\mu, \text{Jet}) < 0.5$ , or if a second muon  
 14 candidate exists that is either loose, non-isolated or outside of acceptance if the two  
 15 muons have an invariant mass with in  $\pm 25 \text{ GeV}$  of the  $Z$  mass, to suppress  $Z \rightarrow \mu\mu$   
 16 events.



**Figure 7.2:** Transverse mass between the selected muon and  $\cancel{E}_T$  in  $W \rightarrow \mu\nu$  events.[5].

**17 The  $\mu\mu + \text{Jets}$  control sample** The  $\mu\mu + \text{Jets}$  control sample is used to measure the  
 18  $Z \rightarrow \nu\nu + \text{Jets}$  irreducible background in the signal region. The process  $Z \rightarrow \mu\mu + \text{Jets}$  is  
 19 identical kinematically, however the acceptance and the branching ratio are both smaller  
 20 the branching ratio due to the possible decay in to one of three neutrino flavour states

verses the requirement of a particular lepton flavour, the acceptance difference is due to the  $p_T$  and identification quality requirements on the muons alter the acceptance between the two processes. The following selection criteria are applied on top of the common selection: Exactly two tightly identified, isolated muons, with in  $|\eta| < 2.5$  with  $p_T > 10$  GeV are required; The invariant mass of the di-muon pair is required to be with in  $\pm 25$  GeV of the Z mass; Events are vetoed if for any muon and jet combination  $\Delta R(\mu, Jet) < 0.5$ . As in the single muon control sample all event level quantities are calculated from the hadronic objects alone. This control sample can be used in all of the offline  $H_T$  bins.

**The  $\gamma +$  Jets control sample** The  $\gamma +$  Jets control sample can also be used to measure the  $Z \rightarrow \nu\nu +$  Jets background as the  $\gamma +$  Jets process is kinematically similar when the  $\gamma E_T > \approx 100$  GeV[21, 15], again when calculating the event level quantities only hadronic objects are considered. The photon sample requires the following criteria on top of the common selection requirements: Exactly one photon with  $E_T > 150$  GeV to ensure trigger efficiency,  $|\eta| < 1.45$ . Events are vetoed if for any jet  $\Delta R(\gamma, jet) < 1.0$ . Given that due to the trigger requirements the photon  $E_T$  is required to be greater than 150 GeV and the photon is treated as missing energy, the  $\alpha_T > 0.55$  requirement implies a minimum  $H_T$  threshold of  $\approx 350$  GeV, hence the  $\gamma +$  Jets control sample can only be used in the offline region where  $H_T > 375$  GeV.

Table 7.2 gives the hadronic signal yields in each of the offline  $H_T$  bins along with the simple background estimate from the single muon plus jets control sample. The full background prediction is given from the results of the simultaneous fit to the separate background estimates.

**Muon control samples with out an  $\alpha_T$  cut.** The requirement of an  $\alpha_T$  value above 0.55 in the previous control samples limits the event yield of each of the montecarlo samples, increasing the statistical error of the prediction. This is especially evident when splitting the analysis in to more dimensions than the  $H_T$  binning. The requirement of an  $\alpha_T$  cut on the control samples means that as the muon is not seen by the calorimeter systems the signal trigger can also be used to collect the both the single and di muon background samples. The translation factor method can be used to create a prediction from any sample to any other sample if and only if the modelling of the event kinematics and acceptances of any cuts introduces no large systematic errors. We now show that

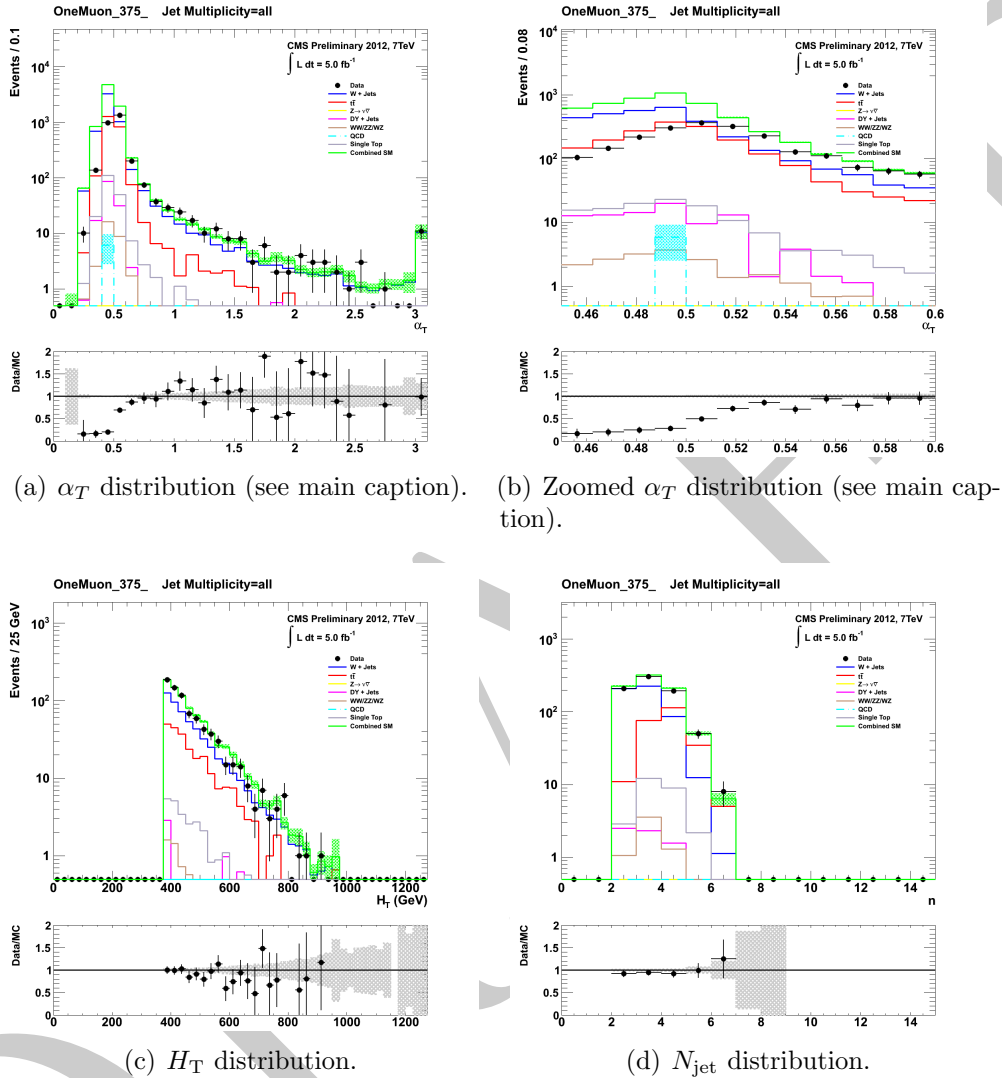
**Table 7.2:** Total SM prediction using the  $\mu + \text{Jets}$  sample only. These are illustrative only, as the final prediction is provided by the final simultaneous fit.

$\alpha_T$ bin	0.55– $\infty$	0.55– $\infty$	0.55– $\infty$	0.55– $\infty$
$H_T$ bin (GeV)	275–325	325–375	375–475	475–575
Hadronic selection MC	$2872.32 \pm 64.44$	$1384.22 \pm 51.46$	$1041.38 \pm 12.53$	$396.13 \pm 19.85$
$\mu + \text{jets}$ selection MC	$1228.90 \pm 46.18$	$670.50 \pm 38.74$	$495.14 \pm 7.86$	$181.65 \pm 9.65$
Translation factor	$2.34 \pm 0.10$	$2.06 \pm 0.14$	$2.10 \pm 0.04$	$2.18 \pm 0.16$
$\mu + \text{jets}$ selection yield data	1421	645	517	169
Total SM prediction	$3321.30 \pm 169.97$	$1331.57 \pm 105.45$	$1087.36 \pm 52.50$	$368.56 \pm 39.09$
Hadronic yield data	3703	1533	1043	346
$\alpha_T$ bin	0.55– $\infty$	0.55– $\infty$	0.55– $\infty$	0.55– $\infty$
$H_T$ bin (GeV)	575–675	675–775	775–875	875– $\infty$
Hadronic selection MC	$142.37 \pm 7.61$	$55.47 \pm 3.51$	$18.68 \pm 1.45$	$13.18 \pm 1.15$
$\mu + \text{jets}$ selection MC	$70.84 \pm 4.36$	$22.64 \pm 1.82$	$7.54 \pm 0.80$	$5.19 \pm 0.67$
Translation factor	$2.01 \pm 0.16$	$2.45 \pm 0.25$	$2.4 \pm 0.33$	$2.54 \pm 0.40$
$\mu + \text{jets}$ selection yield data	52	18	8	1
Total SM prediction	$104.50 \pm 16.81$	$44.09 \pm 11.33$	$19.83 \pm 7.41$	$2.54 \pm 3.47$
Hadronic yield data	122	44	14	6

<sup>1</sup> the montecarlo simulation accurately reproduces the kinematics and acceptance of the  
<sup>2</sup>  $\alpha_T$  cut when applied to electro-weak background samples, enabling the removal of the  
<sup>3</sup>  $\alpha_T$  requirement for the muon control samples.

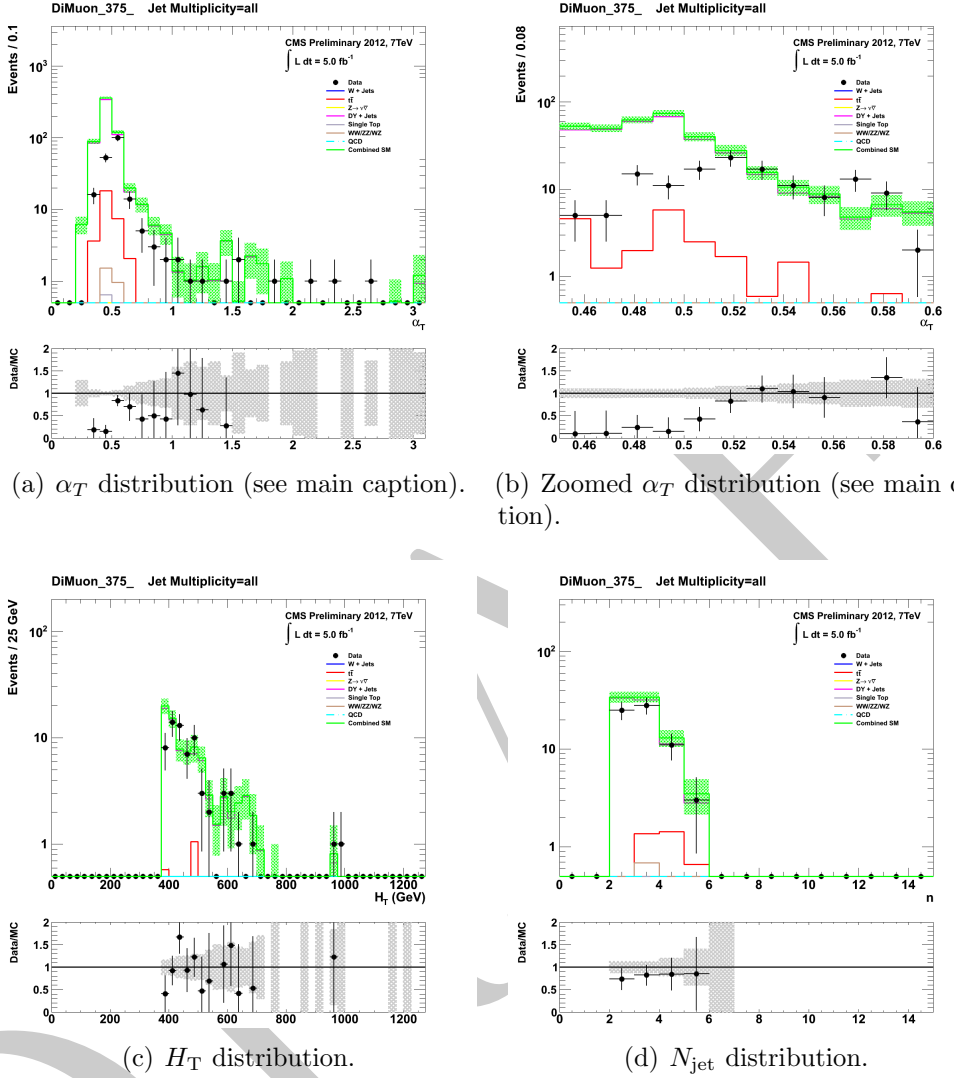
<sup>4</sup> The preselection of events in the two muon control samples ensures samples with  
<sup>5</sup> negligible QCD contamination, which are enriched with  $t\bar{t}$ ,  $W + \text{Jets}$  and  $Z + \text{Jet}$  events.  
<sup>6</sup> This is shown for the  $\mu + \text{Jets}$  sample in Figure 7.3 and for the  $\mu\mu + \text{Jets}$  sample in  
<sup>7</sup> Figure 7.4, in both sets of plots the expected number of QCD events from montecarlo  
<sup>8</sup> simulation is less than one event at any  $\alpha_T$  value for  $5 \text{ fb}^{-1}$  of integrated luminosity. The  
<sup>9</sup> requirement of tight isolation on each of the muons is largely responsible for the purity of  
<sup>10</sup> the sample, the transverse mass and di-muon mass window cuts ensure the sample is rich  
<sup>11</sup> in electro-weak events with visible muons. The agreement between data and montecarlo  
<sup>12</sup> in these plots is good and the simulation models the  $\alpha_T$  acceptance well, the systematic  
<sup>13</sup> assigned to this acceptance is detailed in Section 7.3.

<sup>14</sup> Moving to a selection where there is no required  $\alpha_T$  cut means that the  $\alpha_T$  trigger  
<sup>15</sup> suite can not be used to collect the high event yield control samples. Instead a trigger  
<sup>16</sup> requiring  $H_T$  and a muon in the final state (`Mu_HT`) is used, due to the muon trigger  
<sup>17</sup> threshold the  $p_T$  acceptance cut is raised to 45 GeV in these control samples. The  $H_T$



**Figure 7.3:** Data-MC comparisons of key variables for the muon control sample, for the region  $H_T > 375\text{GeV}$  and  $\alpha_T > 0.55$ . Bands represent the uncertainties due to the limited size of MC samples. No requirement is made on the number of b-tagged jets in an event. *The discrepancy in the  $\alpha_T$  distributions for values  $\alpha_T > 0.55$  is due to the trigger not being simulated in the MC simulation.*

- 1 requirement on these triggers raises to 300 GeV so only the offline bins with  $H_T >$
- 2 375 GeV are able to benefit from the increased background estimation precision, due to
- 3 the larger size of the predicting sample. The efficiency for triggering on a single muon at
- 4 45 GeV is measured to be  $91.3 \pm 0.1\%$  though out the data taking period, measured for
- 5 the  $H_T +$  single muon triggers, the  $H_T$  component of the trigger is measured to be 100%
- 6 efficient though out. In the case of the di-muon sample, as both muons have to be above



**Figure 7.4:** Data-MC comparisons of key variables for the di-muon control sample, for the region  $H_T > 375 \text{ GeV}$  and  $\alpha_T > 0.55$ . Bands represent the uncertainties due to the limited size of MC samples. No requirement is made on the number of b-tagged jets in an event. *The discrepancy in the  $\alpha_T$  distributions for values  $\alpha_T > 0.55$  is due to the trigger not being simulated in the MC simulation.*

1 45 GeV and either of them could have triggered the event, the efficiency is found to be  
 2  $H_T$ -dependant in the range of 95-97%.

3 The muon control samples in the  $H_T$  bins where  $H_T < 375 \text{ GeV}$  are collected with  
 4 the  $\alpha_T$  trigger suite and the measured efficiencies are the same as those measured for the  
 5 hadronic sample. The details of the triggers used for each of the muon + Jets control  
 6 samples are listed in Table 7.3.

**Table 7.3:** List of triggers used for the larger  $\mu + \text{Jets}$  and  $\mu\mu + \text{Jets}$  samples.

$H_T$ bin (GeV)	275–325	325–375	375–475	475–575	575–675	675–775	775–875	>875
$\alpha_T$ cut	0.55	0.55	None	None	None	None	None	None
Muon $p_T$ cut	10	10	45	45	45	45	45	45
Trigger	$\alpha_T$	$\alpha_T$	Mu_HT	Mu_HT	Mu_HT	Mu_HT	Mu_HT	Mu_HT
Dataset	HT	HT	MuHad	MuHad	MuHad	MuHad	MuHad	MuHad
Thresholds	Table 2	Table 2	Table 3					

## <sup>1</sup> 7.2 Estimating the residual QCD background component.[<sup>6</sup>]

<sup>3</sup> The expected QCD contamination in the signal region where  $H_T > 275$  GeV and  $\alpha_T >$   
<sup>4</sup> 0.55 from simulated background samples is negligible, residual events are removed via the  
<sup>5</sup> application of the detector failure and  $R_{miss} < 1.25$  filters. However due to the difficulty  
<sup>6</sup> in simulating QCD multi jet events accurately a conservative approach is taken where a  
<sup>7</sup> term is inserted in the likelihood to model any residual QCD contamination.

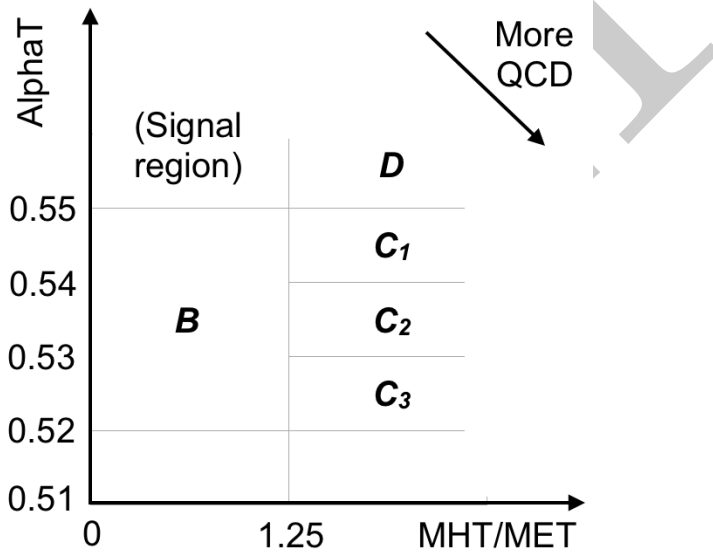
The term is based on the ratio of the number of events above and below the  $\alpha_T$  threshold of 0.55 in the individual  $H_T$  bins. The dependance of this ratio is modelled as an exponentially falling quantity:

$$R_{\alpha_T}(H_T) = \mathcal{A}_{nb} e^{-k_{QCD} H_T} \quad (7.2)$$

<sup>8</sup> Where  $\mathcal{A}_{nb}$  is the b-tag bin dependant normalisation factor and  $k_{QCD}$  is the b-tag  
<sup>9</sup> dependant decay constant.

<sup>10</sup> The exponential behaviour is due to several features, the first of which is the improve-  
<sup>11</sup> ment of the jet energy resolution with  $H_T$  due to the larger energies deposited in the  
<sup>12</sup> calorimeter systems. Secondly for the region  $H_T > 375$  GeV the jet multiplicity rises  
<sup>13</sup> slowly with  $H_T$ , which due to the combinatorics used in the  $\alpha_T$  calculation, results in  
<sup>14</sup> a narrower  $\alpha_T$  distribution peaked at 0.5. Due to the signal region definition and the  
<sup>15</sup> exponentially falling nature of the QCD background component is reduced to zero above  
<sup>16</sup>  $\approx 500$  GeV, thus the validity of the QCD background model above 575 GeV is not of  
<sup>17</sup> consequence to the final analysis, however the model chosen is shown to be valid over  
<sup>18</sup> the whole  $H_T$  region of the analysis as shown below.

Maximum likelihood (M.L) values for  $k_{QCD}$  and  $\mathcal{A}_{nb}$  are found by the final likelihood fit, however  $k_{QCD}$  is first constrained by a measurement in a background enriched side band regions where either the  $\alpha_T$  cut is relaxed or the  $R_{miss}$  cut is inverted. Figure 7.5 depicts the regions where  $k_{QCD}$  is measured, the signal region is as described before where  $\alpha_T > 0.55$  and  $R_{miss} < 1.25$  are required. Region B is defined by the inversion of the  $\alpha_T$  cut. Region C is defined by inverting both the  $\alpha_T$  requirement and the  $R_{miss}$  requirement, this region is further divided in to three slices in  $\alpha_T$  of  $0.52 < \alpha_T < 0.53$ ,  $0.53 < \alpha_T < 0.54$  and  $0.54 < \alpha_T < 0.55$ , as the index of  $C_i$  rises the expected amount of QCD in that control region increases. Finally region D has only the  $R_{miss}$  requirement inverted, region D is not used to constrain  $k_{QCD}$ , but instead to check the validity of the exponential model. The fits to the individual side bands are shown in Appendix 2. The



**Figure 7.5:** QCD side-band regions, used for determination of  $k_{QCD}$ .

best fit value for  $k_{QCD}$  of  $2.96 \pm 0.64 \times 10^{-2} \text{ GeV}^{-1}$  obtained from region B is used as the central value of the constraint. The assumption that this method gives an unbiased estimate of  $k_{QCD}$  stems from the similarity in event kinematics in the two  $\alpha_T$  regions. The best fit values for the three  $C_i$  regions are used to estimate the systematic uncertainty on the central value obtained from region B. The fit results show now dependance on the  $\alpha_T$  region used to measure the number of events, supporting the assumption that region B provides an unbiased estimate of  $k_{QCD}$ . The variation of the measured values for each  $C_i$  slice are used to calculate the error on the central value, the weighted mean and standard deviation of the three slices in  $\alpha_T$  are calculated to be  $1.13 \pm 0.26 \times 10^{-2} \text{ GeV}^{-1}$ , the relative error on this value is 20% which is then applied to the central value to give an estimate of the systematic uncertainty.

<sup>1</sup> The data side bands are used to provide a constrained value of  $k_{QCD}$  as an input to  
<sup>2</sup> the final likelihood model which describes the expected number of background events in  
<sup>3</sup> bins of  $H_T$  and the number of observed jets containing a b quark. The value measured for  
<sup>4</sup>  $k_{QCD}$  is  $2.96 \pm 0.61(\text{stat}) \pm 0.46(\text{sys}) \times 10^{-2} \text{ GeV}^{-1}$ . The uncertainty values are used  
<sup>5</sup> as penalty timers in the likelihood model which is described in Section 7.4

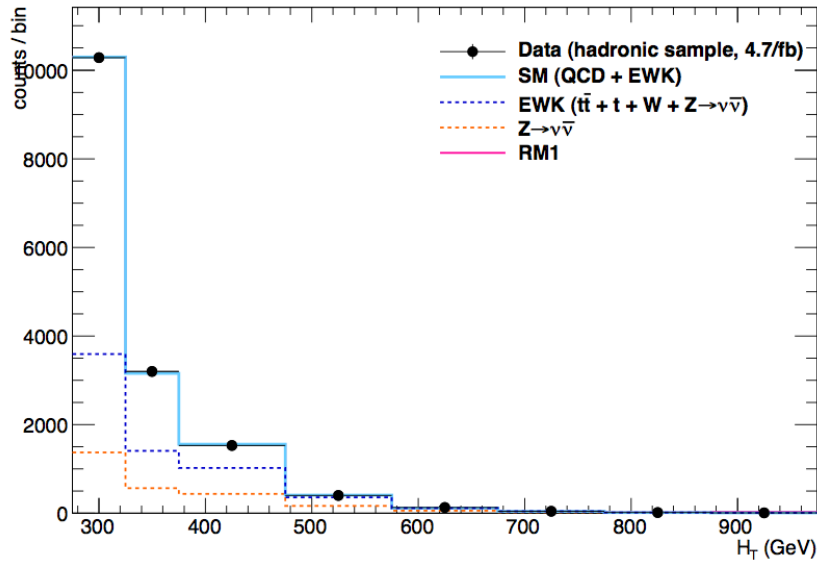
**Table 7.4:** Best fit values for the parameters  $k$  as obtained from the regions  $B$ ,  $C_1$ ,  $C_2$ , and  $C_3$ . The latter three measurements are used to calculate a weighted mean (identified as region  $C$ ). Also quoted is the maximum likelihood value of the parameter  $k$  given by the simultaneous fit using the sample defined by region  $D$ . Quoted errors are statistical only. From [6].

Side-band region	$k_{QCD} (\times 10^{-2} \text{ GeV}^{-1})$	p-value
$B$	$2.96 \pm 0.64$	0.24
$C_1$	$1.19 \pm 0.45$	0.93
$C_2$	$1.47 \pm 0.37$	0.42
$C_3$	$1.17 \pm 0.55$	0.98
$C$ (weighted mean)	$1.31 \pm 0.26$	-
$D$ (likelihood fit)	$1.31 \pm 0.09$	0.57

<sup>6</sup> A final check is performed using region  $D$ , which requires  $\alpha_T > 0.55$  but has no  
<sup>7</sup>  $R_{miss}$  cut, this introduces QCD background in to the signal region. The likelihood fit  
<sup>8</sup> is performed on this background enriched region and no constraint is applied on  $k_{QCD}$   
<sup>9</sup> which is then determined by the fit only. The fit is performed over the full  $H_T$  range  
<sup>10</sup> used in the final analysis. Figure 7.6 shows the resulting fit, the M.L value obtained for  
<sup>11</sup>  $k_{QCD}$  is  $(1.31 \pm 0.09) \times 10^{-2} \text{ GeV}^{-1}$ , this value is in excellent agreement with the value  
<sup>12</sup> found from the weighed mean of the regions  $C_i$ , secondly the fit shows that the choice of  
<sup>13</sup> exponential function used in the likelihood model is valid over the entire  $H_T$  range. This  
<sup>14</sup> supports the assumption that region  $B$  provides an unbiased estimate of  $k_{QCD}$  in the  
<sup>15</sup> signal region  $\alpha_T > 0.55$  and  $R_{miss} < 1.25$ .

### <sup>16</sup> 7.3 Systematic uncertainties on the electro-weak <sup>17</sup> background model.

<sup>18</sup> As previously discussed in Section 7.1 the final background prediction is given by the  
<sup>19</sup> simultaneous fit to the yields in the signal and control samples and the translation  
<sup>20</sup> factors obtained from MC. The fit has some freedom via the statistical and systematic



**Figure 7.6:** Comparison of the observed yields and SM expectations given by the simultaneous fit in bins of  $H_T$  for the side-band region  $D$ . No requirement on the number of b jets is made. Shown are the observed event yields in data (black dots with error bars representing the statistical uncertainties) and the expectations given by the simultaneous fit for the  $Z \rightarrow \nu\nu + \text{jets}$  process (orange dotted-dashed line); the sum of all processes with genuine  $\cancel{E}_T$ , which are primarily  $t\bar{t}$ ,  $W + \text{jets}$ , and  $Z \rightarrow \nu\nu + \text{jets}$  (dark blue long-dashed line); and the sum of QCD and all aforementioned SM processes (light blue solid line).<sup>[6]</sup>

<sup>1</sup> uncertainties measured for each translation factor. This implies that the measurement of  
<sup>2</sup> the systematic uncertainties on the translation factors are vital for the fitting procedure.

<sup>3</sup> A set of closure tests were performed on data to identify any sources of systematic  
<sup>4</sup> biased introduced by the background prediction method. To do this the individual  
<sup>5</sup> background samples are used to predict one another using the same translation factor  
<sup>6</sup> method as for the prediction of S.M missing energy sources in the hadronic signal regions.  
<sup>7</sup> The level of agreement is quantified in terms of the ratio  $(N_{\text{obs}} - N_{\text{pred}})/N_{\text{pred}}$ , the  
<sup>8</sup> statistical error from the translation factor, based on the available Montecarlo statistis  
<sup>9</sup> is combined with the statistical error on the number of events in the predicting sample  
<sup>10</sup> to give the error on the closure, hence the deviation of the ratio from zero gives the  
<sup>11</sup> level of closure per analysis bin. This gives a measure of any biases introduced by the  
<sup>12</sup> background estimation method.

<sup>13</sup> The closure tests between the background samples are designed to test the Montecarlo's  
<sup>14</sup> ability to model kinematic effects; such as the  $\alpha_T$  acceptance;  $\mu$  acceptance and  $\gamma$   
<sup>15</sup> acceptance, instrumental effects such as; reconstruction efficiencies and the effects of

pile up on isolation and finally the theoretical precision of the production and decay cross sections and their relative contributions to the S.M background. These individual components are not separable by the closure tests, which instead gives a total systematic error estimation.

As described in Section 7.1 the control samples which do not require an  $\alpha_T$  cut use a Mu-HT cross object trigger to collect the data events. As shown in Table 3 there was a period of data taking where due to the increased trigger thresholds the Mu-HT triggers are unsuitable for use in the region  $H_T < 375$  GeV. Thusly in the closure tests between the control samples which use an  $\alpha_T$  cut and those that do not the integrated luminosity is limited to  $3.9 \text{ fb}^{-1}$ . This causes a loss of some statistical power in these cases.

The individual closure tests and fits to the  $H_T$  dependance of the ratio  $(N_{obs} - N_{pred}) / N_{pred}$  are shown in Appendix 3. The Figures 6 show the closure of the prediction between  $\mu + \text{Jets}(\text{no } \alpha_T) \rightarrow \mu + \text{Jets}(\alpha_T > 0.55)$  and  $\mu\mu + \text{Jets}(\text{no } \alpha_T) \rightarrow \mu\mu + \text{Jets}(\alpha_T > 0.55)$  for two samples, one with no requirement on the number of b tagged jets ( $n_b$ ), which increases the precision of the measurement, and one requiring  $n_b = 1$ , the red line is the result of a one parameter fit. The level of closure shows that the Montecarlo accurately models the  $\alpha_T$  acceptance, with no significant bias.

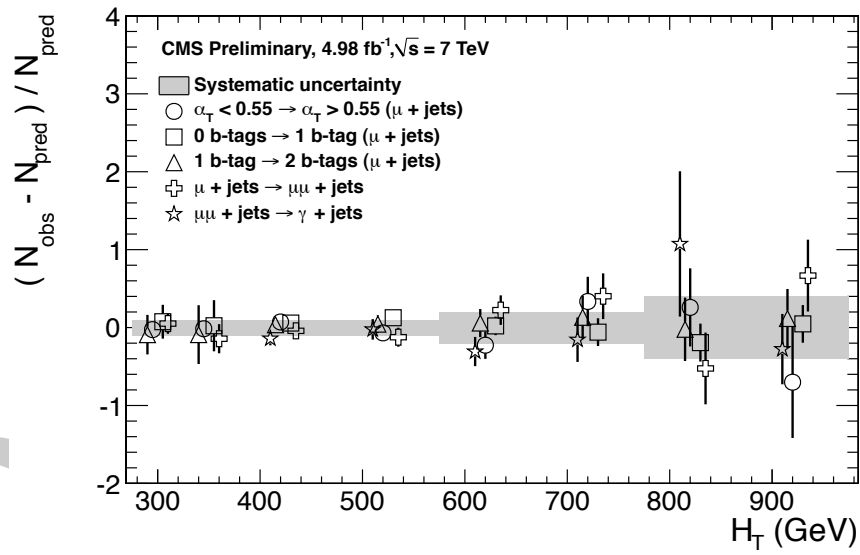
Figure 7 shows the closure between  $\mu + \text{Jets} \rightarrow \mu\mu + \text{Jets}$  and between  $\gamma + \text{jets} \rightarrow \mu\mu + \text{Jets}$  over both the full  $H_T$  range using only  $3.9 \text{ fb}^{-1}$  of integrated luminosity and for  $H_T > 375$  GeV using the full data set. Again the red lines are the result of fitting with a one parameter fit.

Figure 8 tests the closure between samples with differing  $n_b$  the three tests are  $\mu + \text{Jets}(n_b = 0) \rightarrow \mu + \text{Jets}(n_b = 1, \text{no } \alpha_T)$ ,  $\mu + \text{Jets}(n_b = 1) \rightarrow \mu + \text{Jets}(n_b > 1, \text{no } \alpha_T)$  and  $\mu + \text{Jets}(n_b = 0) \rightarrow \mu + \text{Jets}(n_b > 1, \text{no } \alpha_T)$ . Figure 9 also tests the closure between samples with differing  $n_b$ , here the test is between  $\mu + \text{Jets}(n_b = 0) \rightarrow \mu\mu + \text{Jets}(n_b = 0)$  and  $\mu + \text{Jets}(n_b = 1) \rightarrow \mu\mu + \text{Jets}(n_b = 1)$ .

Finally any dependance on pile up is measured by comparing a subset of the individual closure tests between samples which have pile up subtracted jets and those that do not. The example closures are  $\mu + \text{Jets}(\text{no } \alpha_T) \rightarrow \mu + \text{Jets}(\alpha_T > 0.55)$ ,  $\mu + \text{Jets}(\text{no } \alpha_T) \rightarrow \mu\mu + \text{Jets}(\text{no } \alpha_T)$ , and  $\mu + \text{Jets}(n_b = 0) \rightarrow \mu + \text{Jets}(n_b = 1, \text{no } \alpha_T)$ .

### <sup>1</sup> 7.3.1 Motivating the combined systematic on the translation <sup>2</sup> factors

<sup>3</sup> The closure tests described in the previous section are combined to give a total systematic  
<sup>4</sup> uncertainty. This uncertainty is binned in to three  $H_T$  regions  $275 \text{ GeV} \rightarrow 575 \text{ GeV}$ ,  
<sup>5</sup>  $575 \text{ GeV} \rightarrow 775 \text{ GeV}$  and  $775 \text{ GeV}+$ . In each of these regions all of the individual closure  
<sup>6</sup> tests are used to calculate a weighted mean and variance. The systematic is defined as  $3\sigma$   
<sup>7</sup> of this variance, which is conservative but necessary to cover any biases. The systematics  
<sup>8</sup> are treated as fully uncorrelated between the three regions, again this is the conservative  
<sup>9</sup> approach. Figure 7.7 shows the key example closures, the grey shaded region shows the  
<sup>10</sup> systematic error. The values obtained for the error are 6%, 20% and 39%, these are  
<sup>11</sup> rounded to 10%, 20% and 40% and then used in the final background simultaneous fit.



**Figure 7.7:** A set of closure tests (open symbols) overlaid on top of grey bands that represent the systematic uncertainties used for three  $H_T$  regions in the final simultaneous fit. The solid circles and their errors represent the weighted mean and standard deviation for the five closure tests of each individual  $H_T$  bin.

## <sup>12</sup> 7.4 Likelihood model

**Declaration** The likelihood model was implemented, developed, commissioned and deployed in anger by Edward Laird and is best described in his thesis[33]. However for completeness the likelihood model is described in this section. The likelihood is used

to gauge the agreement between the observed yields in the hadronic signal region and the predicted yields obtained from the control samples. For the hadronic sample the likelihood is as follows, for  $N$  bins in  $H_T$ , let  $n_i$  represent the observed hadronic yield in  $H_T$  bin  $i$ , the likelihood for observing  $n_i$  events is then

$$L_{had} = \prod_i Pois(n_i | b_i + s_i) \quad (7.3)$$

- <sup>1</sup> where  $b_i$  is the number of expected background events and  $s_i$  the expected signal
- <sup>2</sup> yield, which is dependant on the signal model being considered. Pois refers to the Poisson
- <sup>3</sup> distribution of these values,  $b_i$  is equal to the sum of electro-weak events expected plus
- <sup>4</sup> the number of QCD events ( $b_i = EWK_i + QCD_i$ ) expected per bin.

In Section 7.2 it was shown that the QCD contribution can be modelled as an exponentially falling as a function of  $H_T$ .

$$R_{\alpha_T}(H_T) = A_{qcd} e^{-k_{QCD} H_T} \quad (7.4)$$

Where  $A_{QCD}$  and  $k_{QCD}$  have been constrained by measurements in the control regions.  $QCD_i$  is then given as:

$$QCD_i = m_i A_{qcd} e^{-k_{QCD} \langle H_T \rangle^i}. \quad (7.5)$$

- <sup>5</sup> Where  $m_i$  is the number of events per  $H_T$  bin which fail  $\alpha_T > 0.55$  and  $\langle H_T \rangle^i$  is the
- <sup>6</sup> mean  $H_T$  of the the bin.

For the electro-weak background two components are considered,  $f_{Zinv}^i$  represents the fraction of the total electro-weak background contributed by  $Z \rightarrow \nu\nu + \text{Jets}$  events. This is models as a liner component:

$$f_{Zinv}^i = f_{Zinv}^0 + \frac{\langle H_T \rangle^i - \langle H_T \rangle^0}{\langle H_T \rangle^{N-1} - \langle H_T \rangle^0} (f_{Zinv}^{N-1} - f_{Zinv}^i), \quad (7.6)$$

where  $f_{Zinv}^i$  and  $f_{Zinv}^{N-1}$  are floating parameters who's final values are limited between zero and one. The total number of  $Z \rightarrow \nu\nu + \text{Jets}$  events per bin is then given by:

$$Z_{inv}^i = f_{Zinv}^i \times EWK^i \quad (7.7)$$

with the remaining background from other electro-weak processes given by:

$$\mathcal{Z} = (1 - f_{Zinv}^i) \times EWK^i. \quad (7.8)$$

In each  $H_T$  bin  $i$  there are three background measurements,  $n_\gamma^i$ ,  $n_\mu^i$  and  $n_{\mu\mu}^i$ , representing the event counts from the photon, muon and di-muon control samples respectively, each of these yields has a Montecarlo counter-part yield. From the Montecarlo it is also possible to extract  $MC_{Zinv}^i$  and  $MC_{\mathcal{Z}}^i$ . After defining:

$$r_\gamma^i = \frac{MC_\gamma^i}{MC_{Zinv}^i}, \quad r_{\mu\mu}^i = \frac{MC_{\mu\mu}^i}{MC_{Zinv}^i}, \quad r_\mu^i = \frac{MC_\mu^i}{MC_{\mathcal{Z}}^i} \quad (7.9)$$

three likelihood functions are defined:

$$L_\gamma = \prod_i Pois \left( n_\gamma^i | \rho_{\gamma Z}^j \cdot r_\gamma^i \cdot Z_{inv}^i \right), \quad (7.10)$$

$$L_{\mu\mu} = \prod_i Pois \left( n_{\mu\mu}^i | \rho_{\mu\mu Z}^j \cdot r_{\mu\mu}^i \cdot Z_{inv}^i \right), \quad (7.11)$$

$$L_\mu = \prod_i Pois \left( n_\mu^i | \rho_{\mu Z}^j \cdot r_\mu^i \cdot \mathcal{Z}^i + s_\mu^i \right), \quad (7.12)$$

- <sup>1</sup> Equation (7.10) is used to estimate the M.L values for  $Z_{inv}$  which is the expectation of  
<sup>2</sup> the number of  $Z \rightarrow \nu\nu + \text{Jets}$  events in the hadronic signal region using the observations  
<sup>3</sup>  $n_\gamma^i$  in the photon control sample and the ratio  $r_\gamma^i$ , similarly the number of  $Z \rightarrow \nu\nu + \text{Jets}$   
<sup>4</sup> events expected in the signal region predicted by the  $Z \rightarrow \mu\mu + \text{Jets}$  are found using  
<sup>5</sup> Equation (7.11). The non  $Z \rightarrow \nu\nu$  backgrounds are estimated by the M.L value for  
<sup>6</sup> Equation (7.12) in a similar way with the addition of  $s_\mu^i$  which represents the signal  
<sup>7</sup> contamination in the single muon control sample. The measurements and ratios are  
<sup>8</sup> considered simultaneously though the relationships defined in

<sup>9</sup> read the note here and reference the right equations.

The ratios  $r_\gamma^i$ ,  $r_{\mu\mu}^i$  and  $r_\mu^i$  are the inverse of the translation factors given by Equation (7.1). The parameters  $\rho_{\gamma Z}$ ,  $\rho_{\mu\mu Z}$  and  $\rho_{\mu Z}$  are correction factors that account for the systematic uncertainty on each of the ratios and  $\sigma_{\gamma Z}$ ,  $\sigma_{\mu\mu Z}$  and  $\sigma_{\mu Z}$  represent the relative

**Table 7.5:** The systematic parameters used in  $H_T$  bins.

$H_T$ bin ( $i$ )	0	1	2	3	4	5	6	7
syst. parameter ( $j$ )	0	0	0	0	1	1	2	2

systematic uncertainties for the control sample constraints, these are accounted for in:

$$L_{EWK \ syst} = \prod_j Gaus \left( 1.0 | \rho_{\mu Z}^j, \sigma_{\mu Z}^j \right) \times Gaus \left( 1.0 | \rho_{\mu\mu Z}^j, \sigma_{\mu\mu Z}^j \right) \times Gaus \left( 1.0 | \rho_{\gamma Z}^j, \sigma_{\gamma Z}^j \right) \quad (7.13)$$

- <sup>1</sup> Three parameters per control sample are used to cover the eight  $H_T$  bins as show in
- <sup>2</sup> Table 7.5.

Alternatively the single muon control sample can be used to constrain the total electro-weak background, we can define:

$$r_\mu^{ti} = \frac{MC_\mu^i}{MC_{tot}^i} \quad (7.14)$$

and

$$L'_\mu = \prod_i Pois \left( n_\mu^i | \rho_{\mu Z} \times r_\mu^{ti} \times EWK^i + s_\mu^i \right) \quad (7.15)$$

**Signal Contamination** The cross section for each model is represented by  $x$ ,  $l$  represents the total recorded luminosity considered by the analysis in the signal region. The efficiency is defined as  $\epsilon_{had}^i$  for the signal region and  $\epsilon_\mu^i$  for the single muon control sample,  $\delta$  represents the relative uncertainty on signal measured in the previous section,  $\delta$  is taken to be fully correlated though the  $H_T$  bins.  $\rho_{sig}$  is the correction factor to the signal yield which accommodates this uncertainty.  $\{\}$  represents an unknown multiplicative factor on the signal cross section, for which an allowed interval is computed. The expected signal yield  $s^i$  from Equation (7.3) is defined as:

$$s_{had}^i = \{\rho_{sig} x l \epsilon_{had}^i, \quad (7.16)$$

the signal contamination  $s_\mu^i$  is given by:

$$s_\mu^i = \{\rho_\mu x l \epsilon_\mu^i\}. \quad (7.17)$$

The systematic on signal uncertainty is included by an additional term in the likelihood:

$$L_{sig} = Gaus(1.0|\rho_{sig}, \delta). \quad (7.18)$$

**The total likelihood** The total likelihood for a given signal selection  $k(H_T, n_b)$  is given by:

$$L^k = L_{had}^k \times L_\mu^k \times L_\gamma^k \times L_{\mu\mu}^k, \quad (7.19)$$

each  $k$  has  $3 + N$  nuisance parameters;  $\mathcal{A}_{QCD}, f_{Zinv}^0, f_{Zinv}^{N-1}, \{EWK^i\}_{i=0}^{N-1}$ . The 11 parameters  $k_{QCD}, \rho_{sig}$ , and  $\rho_{\gamma Z}^k, \rho_{\mu\mu}^k, \rho_\mu^k$  with  $j = \{0, 1, 2\}$  are shared between the selections, the total likelihood is then given as:

$$L = L_{sig} \times L_{EWKsyst} \times \prod_k L_{had}^k \times L_\mu^k \times L_\gamma^k \times L_{\mu\mu}^k. \quad (7.20)$$

## 7.5 Final Results

- 2 The yields obtained in the hadronic signal regions are tested for their compatibility with
- 3 the background predicted by the likelihood model both in terms of agreement with the
- 4 Standard Model and interpretations in the forms of limits on new physics models.

To test the level of agreement with the standard model the signal terms are dropped from the likelihood, which is then maximised over all parameters using `Roofit`[35] and `MINUIT`[31]. The individual yields and errors from the fits are shown in Appendix

put these tables in teh appendix

. The total background and data yields and their errors as given by the M.L fit are show below in Table 7.6.

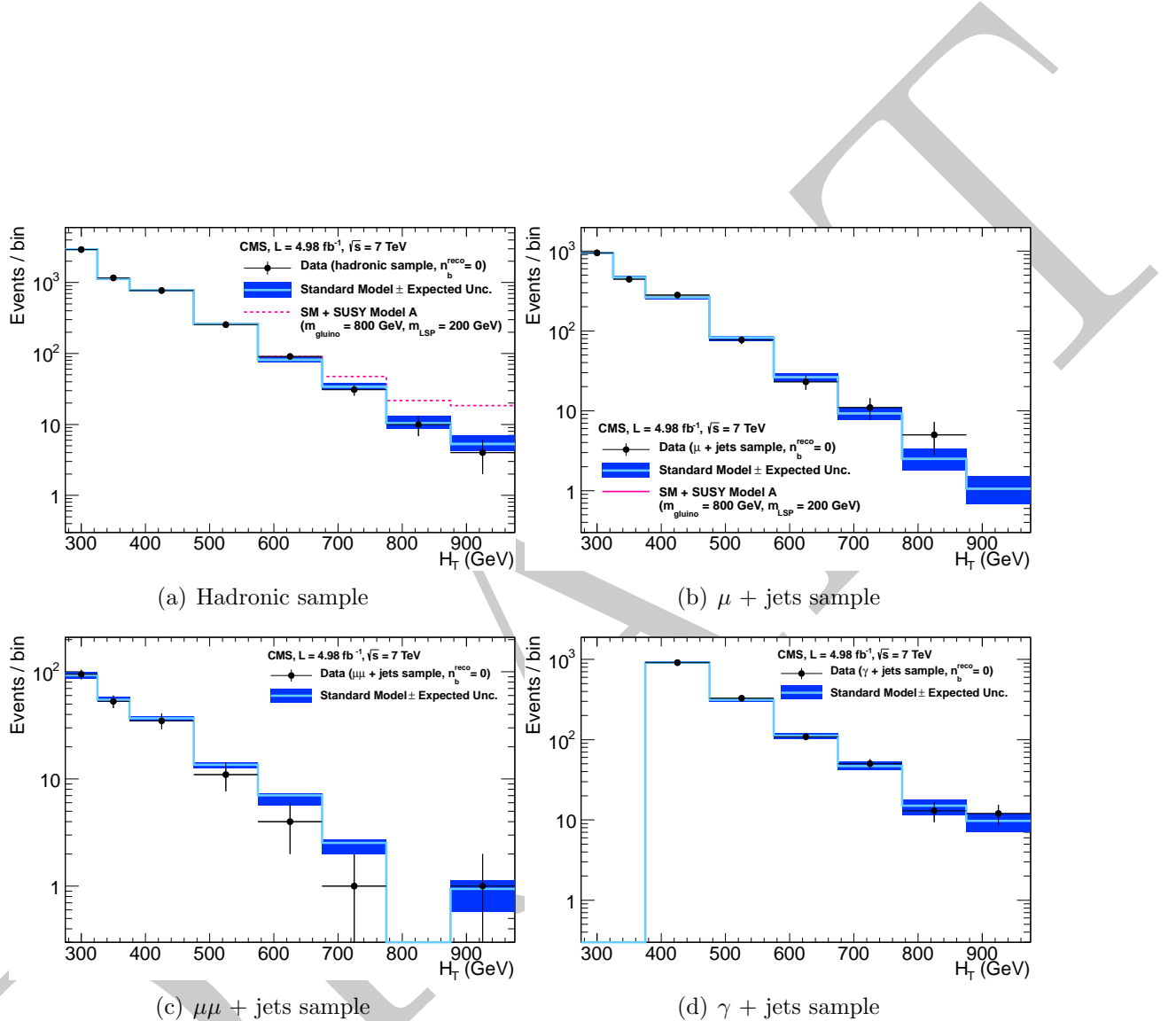
Figures 7.8, 7.9, 7.10 and 7.11 show comparisons of the observed yields and the Standard Model only expectations given by the simultaneous fit for 0, 1, 2,  $\geq 3$  exclusive b-tag bins. A good agreement with the standard model is observed in all  $H_T$  and b-tag

**Table 7.6:** Comparison of the measured yields in the different  $H_T$  and b jet multiplicity bins for the hadronic sample with the SM expectations and combined statistical and systematic uncertainties given by the simultaneous fit.

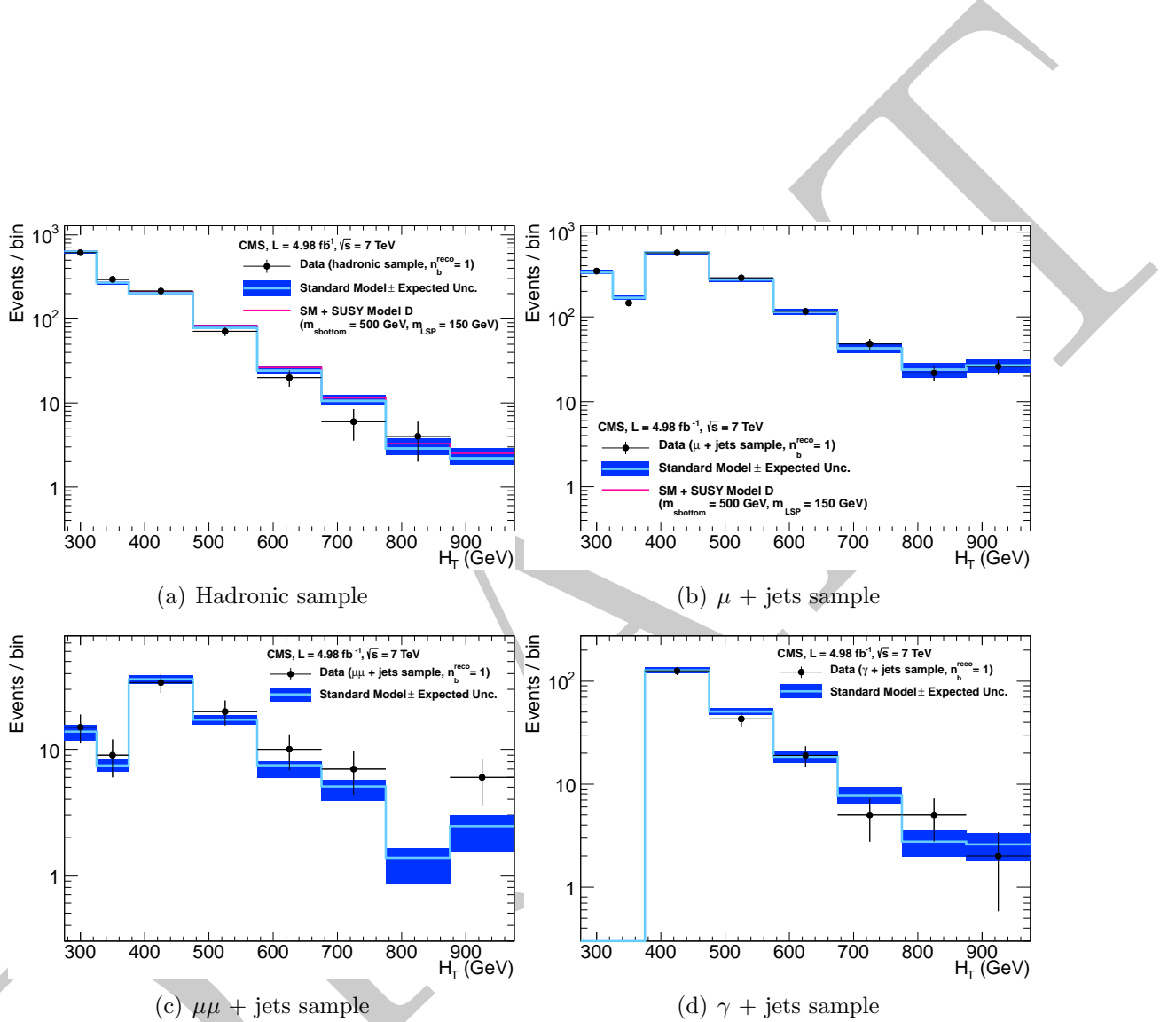
$H_T$ (GeV)	275–325	325–375	375–475	475–575	575–675	675–775	775–875	875– $\infty$
0 b jets SM	$2933^{+56}_{-52}$	$1139^{+17}_{-40}$	$783^{+17}_{-27}$	$261^{+14}_{-8}$	$81.5^{+6.5}_{-6.5}$	$34.2^{+4.0}_{-3.8}$	$10.4^{+2.8}_{-1.8}$	$5.3^{+1.7}_{-1.1}$
0 b jets Data	2919	1166	769	255	91	31	10	4
1 b jet SM	$630^{+26}_{-25}$	$271^{+10}_{-16}$	$202^{+10}_{-6}$	$78.0^{+6.9}_{-1.9}$	$24.2^{+2.9}_{-2.0}$	$10.6^{+1.7}_{-1.3}$	$2.9^{+0.9}_{-0.5}$	$2.2^{+0.7}_{-0.4}$
1 b jet Data	614	294	214	71	20	6	4	0
2 b jets SM	$162^{+13}_{-12}$	$61.8^{+4.8}_{-6.3}$	$58.8^{+4.8}_{-2.6}$	$28.0^{+3.5}_{-1.1}$	$9.0^{+1.4}_{-1.0}$	$7.1^{+1.4}_{-1.0}$	$0.6^{+0.3}_{-0.2}$	$0.9^{+0.4}_{-0.2}$
2 b jets Data	160	68	52	19	11	7	0	2
$\geq 3$ b jets SM	$10.5^{+3.5}_{-2.2}$	$7.1^{+2.2}_{-1.8}$	$5.8^{+1.4}_{-0.9}$	$3.1^{+1.0}_{-0.7}$	$1.7^{+0.5}_{-0.4}$	$0.7^{+0.5}_{-0.4}$	$0.1^{+0.1}_{-0.1}$	$0.2^{+0.1}_{-0.1}$
$\geq 3$ b jets Data	10	8	8	1	0	0	0	0

<sup>1</sup> categories. Given the lack of a signal like observation limits are set on the production

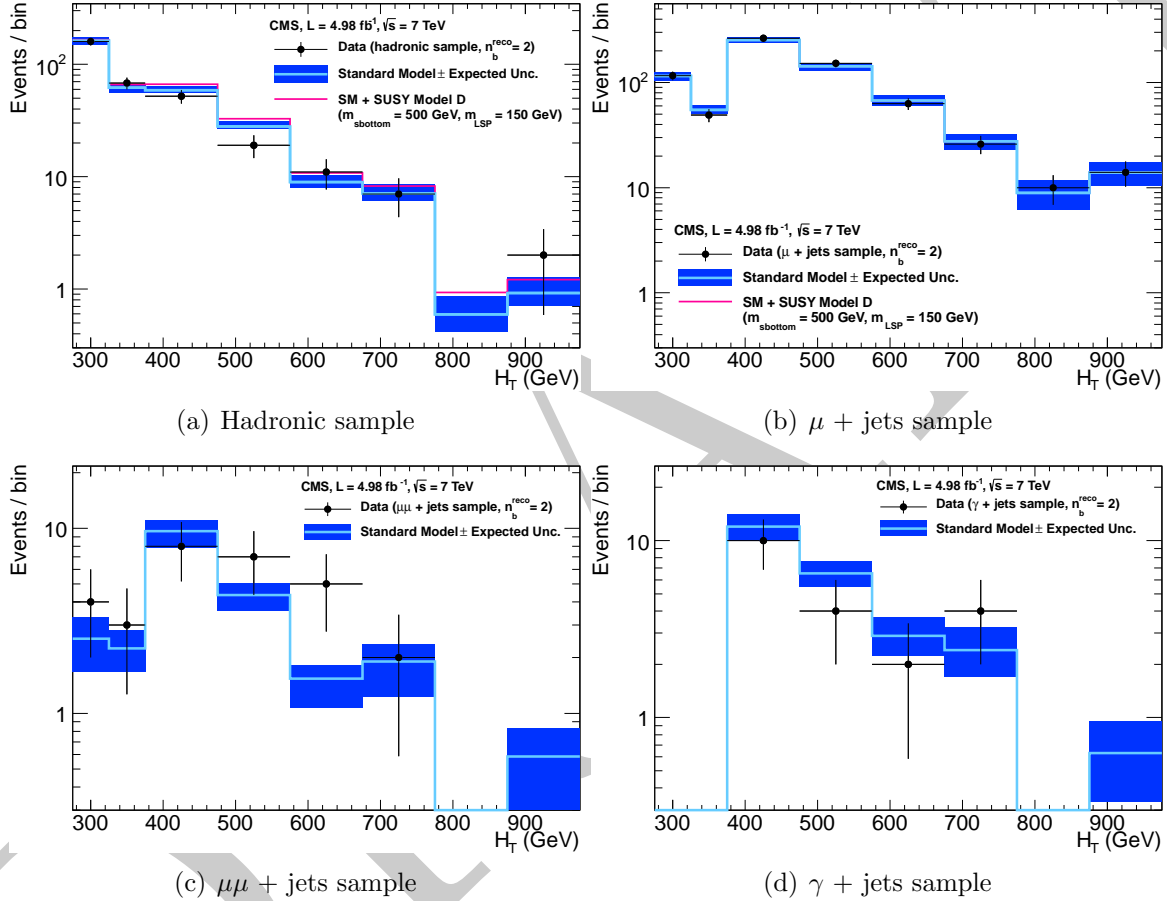
<sup>2</sup> masses and cross sections of beyond the standard model particles.



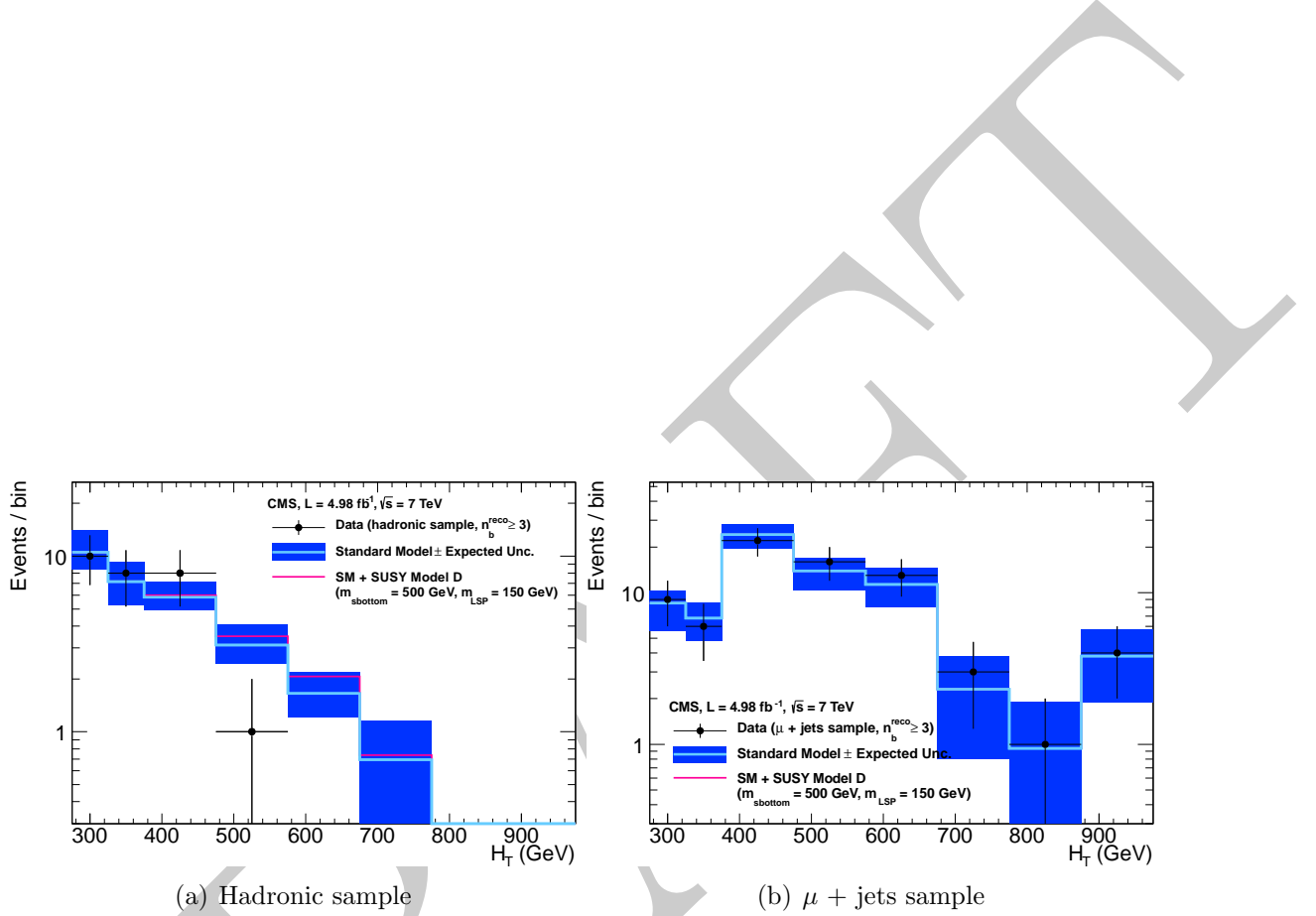
**Figure 7.8:** Comparison of the observed yields and SM expectations given by the simultaneous fit in bins of  $H_T$  for the (a) hadronic, (b)  $\mu +$  Jets, (c)  $\mu\mu +$  Jets and (d)  $\gamma +$  Jets samples when requiring exactly zero reconstructed b-jets. The observed event yields in data (black dots) and the expectations and their uncertainties, as determined by the simultaneous fit, for all SM processes (light blue solid line with dark blue bands) are shown. For illustrative purposes only, an example signal model is superimposed on the SM expectation (magenta solid line). The expected signal contamination in the control samples is negligible.



**Figure 7.9:** Comparison of the observed yields and SM expectations given by the simultaneous fit in bins of  $H_T$  for the (a) hadronic, (b)  $\mu +$  Jets, (c)  $\mu\mu +$  Jets and (d)  $\gamma +$  Jets samples when requiring exactly one reconstructed b-jet. The observed event yields in data (black dots) and the expectations and their uncertainties, as determined by the simultaneous fit, for all SM processes (light blue solid line with dark blue bands) are shown. For illustrative purposes only, an example signal model is superimposed on the SM expectation (magenta solid line). The expected signal contamination in the control samples is negligible.



**Figure 7.10:** Comparison of the observed yields and SM expectations given by the simultaneous fit in bins of  $H_T$  for the (a) hadronic, (b)  $\mu + \text{Jets}$ , (c)  $\mu\mu + \text{Jets}$  and (d)  $\gamma + \text{Jets}$  samples when requiring exactly two reconstructed b-jets. The observed event yields in data (black dots) and the expectations and their uncertainties, as determined by the simultaneous fit, for all SM processes (light blue solid line with dark blue bands) are shown. For illustrative purposes only, an example signal model is superimposed on the SM expectation (magenta solid line). The expected signal contamination in the control samples is negligible.



**Figure 7.11:** Comparison of the observed yields and SM expectations given by the simultaneous fit in bins of  $H_T$  for the (a) hadronic and (b)  $\mu +$  Jets samples when requiring at least three reconstructed b-jets. The observed event yields in data (black dots) and the expectations and their uncertainties, as determined by the simultaneous fit, for all SM processes (light blue solid line with dark blue bands) are shown. For illustrative purposes only, an example signal model is superimposed on the SM expectation (magenta solid line). The expected signal contamination in the  $\mu +$  Jets control sample is negligible.

# Chapter 8

## <sup>1</sup> Interpretation

### <sup>2</sup> 8.1 Signal Models

<sup>3</sup> The level of agreement of the analysis with the S.M give a handle on the production  
<sup>4</sup> cross sections and masses of particles predicted by new physics models. The final results  
<sup>5</sup> are presented in terms of a specific SuperSymmetry (SUSY) model and a selection of  
<sup>6</sup> generic final state topologies, known as Simplified Model Spectra (S.M.S).

<sup>7</sup> The SUSY model considered is the CMSSM[] which is described in Section 2.1, the  
<sup>8</sup> parameters chosen are  $\tan \beta = 3$ ,  $A_0 = 0$ ,  $\mu = 0$  with the exclusion curve presented in the  $m_0$ ,  
<sup>9</sup>  $m_{1/2}$  plane. This model combines many production and decay topologies and is common  
<sup>10</sup> to results shown by previous and contemporary experiments []

<sup>11</sup> Reference ATLAS and Tevatron susy results

<sup>12</sup> . The results are also presented in terms of S.M.S[] models, these are models with  
<sup>13</sup> single production methods and a specified decay topology. The C.M.S terminology for  
<sup>14</sup> the production methods are as follows: T1 models are gluino-gluino production, which  
<sup>15</sup> then decay to four S.M hadronic jets and two neutralinos. T2 models are squark-squark  
<sup>16</sup> production with decays to two S.M hadronic jets and two neutralinos. These topologies  
<sup>17</sup> can be further specialised by enforcing the squarks or gluinos to decay to heavy flavour  
<sup>18</sup> S.M quarks, such as t, which promptly decay to jets containing b quarks or direct decays  
<sup>19</sup> to b quarks. The limits on the S.M.S space are defined in terms of the mass splitting  
<sup>20</sup> between the neutralino and the pair produced SUSY particle defining the model.

## <sup>1</sup> 8.2 Signal Efficiency

### <sup>2</sup> 8.2.1 CMSSM

<sup>3</sup> The CMSSM signal scan is composed of eight sub-processes which define the production  
<sup>4</sup> and decay topologies. The dominant process varies with  $m_0, m_{1/2}$  and at next to leading  
<sup>5</sup> order the cross section for each of these processes varies per point. The analysis is run  
<sup>6</sup> over each sub process in turn with the final efficiency given by the weighted sum of the  
<sup>7</sup> subprocess efficiencies. The yield per point is then given by  $\epsilon \times \mathcal{L}$  for  $5 \text{ fb}^{-1}$  the total  
<sup>8</sup> yields are shown in the appendix in Figure 11 these yields are for the sum of the  $H_T$   
<sup>9</sup> analysis bins.

### <sup>10</sup> 8.2.2 Simplified Models

<sup>11</sup> The S.M.S models contain only one production process and a set decay topology, making  
<sup>12</sup> the interpretation in these models simpler, however the individual models are not  
<sup>13</sup> representative of some complete SUSY model. Instead these models allow the testing of  
<sup>14</sup> specific facets of new physics models, with out the ambiguity of the relative contributions  
<sup>15</sup> of each sub process at a point which is seen when testing full models. The efficiency  
<sup>16</sup> is measured for each of the models, with the yield per point given by  $\epsilon \times \sigma \times \mathcal{L}$  where  
<sup>17</sup>  $\sigma$  is given as a reference cross section only. The efficiencies for which are shown in the  
<sup>18</sup> appendix, Table 8.1 lists which figure corresponds to which model, it is to be noted that  
<sup>19</sup> the total efficiency summed over  $H_T$  bins is shown.

**Table 8.1:** Production and decay modes for various simplified models.

Model	Production and decay modes	Figure showing efficiency
T1	$\tilde{g}\tilde{g} \rightarrow q\bar{q}\tilde{\chi}^0 q\bar{q}\tilde{\chi}^0$	<sup>12</sup>
T2	$\tilde{q}\tilde{q} \rightarrow q\tilde{\chi}^0 \bar{q}\tilde{\chi}^0$	<sup>13</sup>
T2tt	$\tilde{t}\tilde{t} \rightarrow t\tilde{\chi}^0 \bar{t}\tilde{\chi}^0$	<sup>14</sup>
T2bb	$\tilde{b}\tilde{b} \rightarrow b\tilde{\chi}^0 \bar{b}\tilde{\chi}^0$	<sup>15</sup>
T1tttt	$\tilde{g}\tilde{g} \rightarrow t\bar{t}\tilde{\chi}^0 t\bar{t}\tilde{\chi}^0$	<sup>16</sup>
T1bbbb	$\tilde{g}\tilde{g} \rightarrow b\bar{b}\tilde{\chi}^0 b\bar{b}\tilde{\chi}^0$	<sup>17</sup>

<sup>20</sup> **Signal Efficiency for the Background Selection** If the couplings of the SUSY  
<sup>21</sup> particles are analogous to the S.M particles then the final states may involve muons

which in the presence of signal would infer an over estimation of the background from the control samples. To measure this the background selection is applied to the signal models and the yields are taken into account in the final limit setting procedure. On average the background selection’s efficiency on signal is  $10\times$  lower than the efficiency in the hadronic signal region. This is shown for the model T1tttt in Figure 18 where the most muons of all the signal models are expected in the final state, the contamination in the  $n_b$  bins that drive the limit is on the order of 10 – 20%.

### 8.3 Uncertainty on Signal Efficiency

The systematic uncertainty on the signal models is due to: Choice of PDF at generator level, the PDF set used to generate the sample has effects on both the acceptance and the cross section; The measurement of the integrated luminosity is accounted for in the signal yield; Due to the signal models being created with C.M.S FastSim[] rather than C.M.S FullSim[] the acceptance differs between the signal and the background samples; The error on the jet energy scale is accounted for on the signal yield; Systematic errors from the cleanings cuts ( $R_{miss}$  and ECAL dead regions) and lepton/photon vetoes are also taken in to account; Finally corrections to the b-tagging efficiency between the FullSim and the FastSim are applied as well as their errors.

Each of these uncertainties is expressed as a percentage change in the efficiency from the central value given by applying the full analysis to each signal model, the total systematic is given by summing the components in quadrature. In the following section the measurements of the error from each of these sources is detailed and summarised per considered signal model at the end of the section.

The uncertainties for the CMSSM are considered in a band of  $\pm 60$  GeV in  $m_{1/2}$  around the expected limit to confine the errors to the relevant part of the plane, in the very high  $m_0, m_{1/2}$  area the jet energy scale causes large fluctuations due to the small mass splitting between the SUSY particles. For the S.M.S models two regions are defined, one “close” to the diagonal, which has small mass splitting and thus the effects of jet energy scale and PDF acceptance have a large impact on the analysis efficiency. A second “far” region is defined with large mass splitting and thus a small change on the analysis efficiency due to jet energy scale and PDF variations. The near and far regions

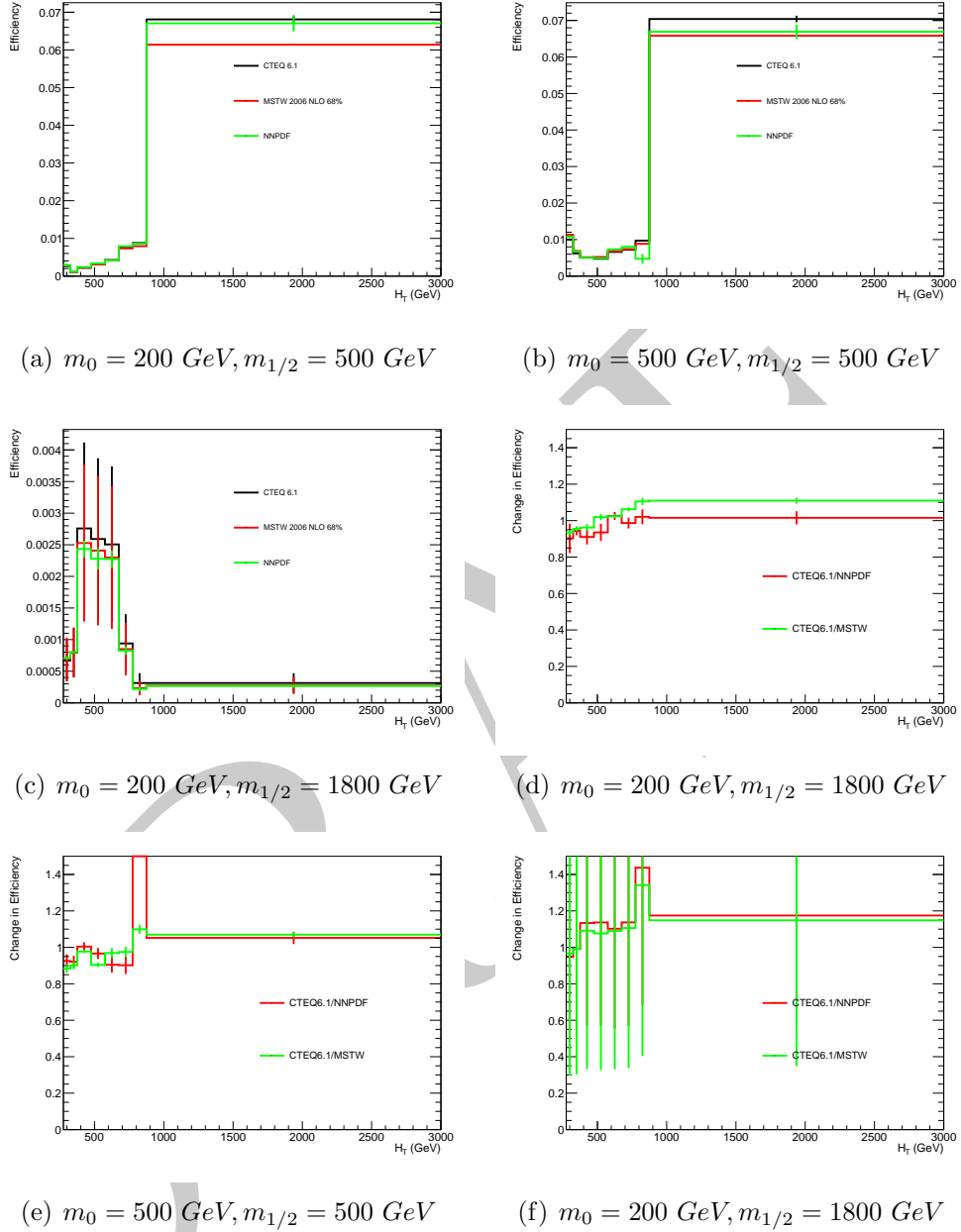
are defined by:

$$m_{sq}(m_{gl}) - m_{lsp} > 350 \text{ GeV and } m_{sq}(m_{gl}) > 475 \text{ GeV} \quad (8.1)$$

- <sub>1</sub> events passing these conditions are classified as being in the “far” region, those failing in  
<sub>2</sub> the “close” region.

### <sub>3</sub> 8.4 Choice of PDF set at generator level.

<sub>4</sub> The PDF set contains information on the interaction probabilities of the quark and  
<sub>5</sub> gluons in the proton at different energies, the model used in the production of the  
<sub>6</sub> Montecarlo simulation has direct impact on the kinematics of the final states, since  
<sub>7</sub> the PDFs have been measured at lower energies than those found at the L.H.C the  
<sub>8</sub> quark and gluon distributions have been extrapolated from the low energy regime, the  
<sub>9</sub> uncertainty at high energy is thus significant. The uncertainties on acceptance due to the  
<sub>10</sub> choice of PDF set used to generate the signal Montecarlo are calculated in line with the  
<sub>11</sub> PDF4LHC[16] working group recommendations. On the event level the individual weights  
<sub>12</sub> are re-calculated by moving between PDF set, the weight is based on the energy at which  
<sub>13</sub> the quarks or gluons interaction and the form given by the PDF. This is done for the  
<sub>14</sub> central value of the three considered PDF sets (CTEQ6.1[40], MSTW2008nlo68cl[42]  
<sub>15</sub> and NNPDF2.0[43]) and for the variations of each of their errors. The change in analysis  
<sub>16</sub> efficiency is measured per  $H_T$  bin, Figure 8.1 shows the deviation in efficiency per bin  
<sub>17</sub> for three examples points in the CMSSM plane, the error bars represent the Root Mean  
<sub>18</sub> Squared (RMS) of the spread of the efficiency inside each PDF set. It is to be noted  
<sub>19</sub> that some bins show a large change in efficiency due to the choice of PDF set, however  
<sub>20</sub> these are low efficiency bins where changes in yield of a few events has a large effect, the  
<sub>21</sub> final result however is driven by the high efficiency bins, hence these large fluctuations  
<sub>22</sub> can be ignored. The effects on the cross section are studied by re-calculating the Next  
<sub>23</sub> to Leading Order (N.L.O) cross sections of each of the sub processes for each choice of  
<sub>24</sub> PDF set, this is done centrally by C.M.S, these changes in cross section are accounted  
<sub>25</sub> for in the error band on the expected limit.



**Figure 8.1:** Figures 8.1(a), 8.1(b) and 8.1(c) show the efficiency per  $H_T$  bin for the inclusive selection. The three coloured lines represent the analysis efficiency for a choice of PDF set, the error bars are the RMS of the change in efficiency per PDF set from varying the internal components by  $1\sigma$  of their error. Figures 8.1(d), 8.1(e) and 8.1(f) show the ratio of the change in efficiency from the default PDF set (CTEQ6.1) for three illustrative points in the  $m_0, m_{1/2}$  plane of the CMSSM. The change in efficiency in the high efficiency bins is on the order of 10% for all points.

## <sup>1</sup> 8.5 Effects of Jet Energy Scale Variations on Signal <sup>2</sup> Efficiency

<sup>3</sup> Section 6.2.1 describes the Jet Energy Corrections (JEC) and their uncertainties, which  
<sup>4</sup> are derived in [18], these uncertainties are dependant on the  $|\eta|$  and  $E_T$  of the jet in  
<sup>5</sup> question. To measure the impact of the individual jet energy uncertainties on signal  
<sup>6</sup> acceptance two additional selections are performed on the signal samples, the first with  
<sup>7</sup> the energy of each jet in the event raised from the central value by  $1\sigma$  of it's uncertainty,  
<sup>8</sup> the second with the energy decreased by  $1\sigma$ , the relative change in efficiency with respect  
<sup>9</sup> to the central value is then calculated for signal point. The model dependant systematic  
<sup>10</sup> is found from the 68<sup>th</sup> percentile of the 1D distribution of the absolute change in signal  
<sup>11</sup> efficiency over each point in the model space. Figure 19 shows the change in efficiency  
<sup>12</sup> over the full  $m_0, m_{1/2}$  plane for the CMSSM, at high  $m_0, m_{1/2}$  the variation is large due  
<sup>13</sup> to the primary production method of SUSY particles being electro-weak production of  
<sup>14</sup> charginos in this region. These charginos then decay though a chain to the neutrino and  
<sup>15</sup> S.M particles, due to the small mass splitting (compressed spectra) between each of the  
<sup>16</sup> charginos the jets produced are only just within  $E_T$  acceptance. A small change of the  
<sup>17</sup> individual jet  $E_T$ 's thus moves many jets in and out of acceptance causing a large change  
<sup>18</sup> in analysis efficiency, hence only the region within  $\pm 60$  GeV around the expected limit in  
<sup>19</sup>  $m_{1/2}$  is considered when calculating the systematic for the CMSSM. The points close to  
<sup>20</sup> the diagonal in the S.M.S models display compressed spectra and so are effected by the  
<sup>21</sup> change in jet energy scale. Figures 20 and 21 show the effects of scaling the jet energies  
<sup>22</sup> for the considered S.M.S models, Figures 22 and 23 show the 68% coverage of the 1D  
<sup>23</sup> distribution of the relative change in efficiency for the near and far regions from which  
<sup>24</sup> the systematic is taken.

## <sup>25</sup> 8.6 Systematic Uncertainty on Signal Yield from <sup>26</sup> Cleaning Filters and Object Veto.

<sup>27</sup> For each of the cleaning cuts,  $R_{miss}$  and the DeadECAL, the systematic is given as the  
<sup>28</sup> product of the ratio of normalised yields in the control samples, between data and  
<sup>29</sup> Montecarlo and the relative change in efficiency due to the cleaning filter for each  
<sup>30</sup> individual signal model. The background sample is chosen before an  $\alpha_T$  cut or any other  
<sup>31</sup> cleaning cuts and is high in real  $\cancel{E}_T$  due to the selection of W + Jets and t $\bar{t}$  events,

meaning the efficiency of the  $R_{miss}$  cut should be high. Figure 24 shows the accuracy of the  $R_{miss}$  modelling, at a cut value of  $R_{miss} < 1.25$  the miss modelling is at the level of 14%. Figures 25, 26 and 27 show the change in selection efficiency due to the  $R_{miss}$  on the signal models.

As for the  $R_{miss}$  cut the background selection is performed on data and Montecarlo and the accuracy of modelling the DeadECAL filter is measured, the ratio of the normalised cut efficiency on data and simulation shows a miss modelling at the level of 1.8%, this is taken as the uncertainty on the Montecarlo model of the detector failures. Figures 29, 30 and 31 show the relative change in efficiency due to the DeadECAL filter on the considered signal models.

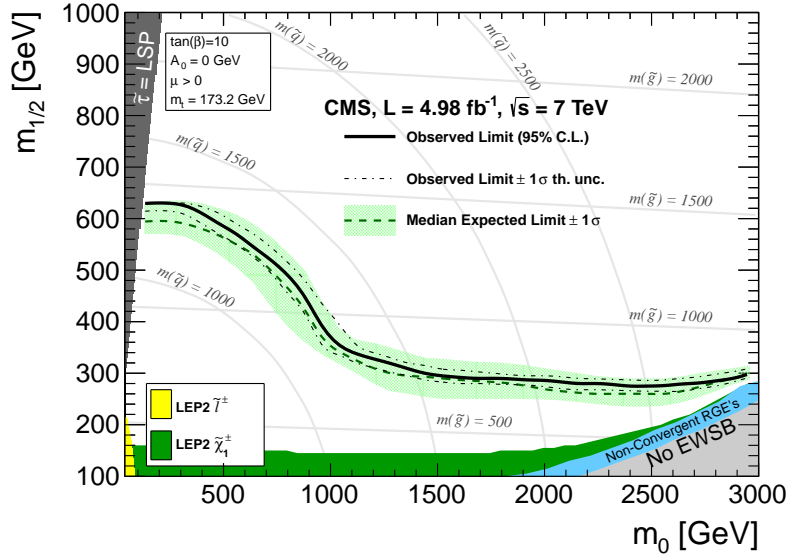
Again regions with compressed spectra and many jet topologies are more effected by the cleaning cuts.

Finally the effects of the lepton vetoes on the signal efficiency are studied. A generator level filter is first applied removing any events with final state leptons or photons, thus measuring the effect of hadronic objects faking leptons or photons. The relative change in efficiency due to the application of the object vetoes is show in Figures 33, 35 and 36, the inefficiency for each signal model are very small and are used directly as the systematic error.

## 8.7 Interpretation in terms of new physics models.

Due to the lack of a signal like observation limits are set on new physics models. The first of these is the CMSSM, at each point in the  $m_0, m_{1/2}$  parameter space the SUSY particle spectrum is calculated using **SoftSUSY**[12], the signal events are generated at leading order using **Pythia 6.4**[41], the Next to Leading Order + Next Leading Log (NLO+NNL) process dependant cross sections are calculated using **PROSPINO**[13] using the **CTEQ6**[40] PDF set. The previously measured errors on the background prediction, total collected luminosity and signal yield are included in the calculation of the limit. Although signal contributions from each data observation (hadronic,  $\mu + \text{Jets}$ ,  $\mu\mu + \text{Jets}$  and  $\gamma + \text{Jets}$ ) are included, the only relevant signal contribution to the CMSSM is from the hadronic signal regions. Figure 8.2 shows the expected limit contour with it's associated  $\pm 1\sigma$  error band as well as the observed limit. The limit is calculated using NLO+NNL cross sections using **CL<sub>s</sub>**[36], the limit presented is for the 95% confidence level. For the choice

of  $\tan \beta = 10$ ,  $A_0 = 0$  GeV,  $\mu > 0$  and a top quark mass  $m_{top} = 173.2$  GeV, squarks with masses below 1.25 TeV are excluded at 95% confidence, gluinos with a mass up to 1.25 TeV are also excluded when  $m_0 < 600$  GeV. In the region  $m_0 > 600$  GeV gluino masses below 700 GeV are excluded as are squarks with masses between 1.25-2.5 TeV,  $m_0$  dependant.



**Figure 8.2:** Exclusion contours at 95% CL in the CMSSM ( $m_0, m_{1/2}$ ) plane ( $\tan \beta = 10, A_0 = 0, \mu > 0$ ) calculated with NLO+NNL SUSY production cross sections and the  $CL_s$  method. The solid black line indicates the observed exclusion region. The dotted-dashed black lines represent the observed excluded region when varying the cross section by its theoretical uncertainty. The expected median exclusion region (green dashed line)  $\pm 1\sigma$  (green band) are also shown.

The observed yields are also used to set limits on S.M.S models. This allows interpretation of the results for defined mass splittings and final states. Each S.M.S sample is characterised by the SUSY particle which is pair produced, either a squark or a gluino and the LSP mass, the individual points are then defined by the mass difference between the pair produced particle and the LSP. The decay topologies are further specialised by enforcing the final state quarks to be heavy flavours, either top or bottom quarks. The decays of the considered models are summarised in Table 8.2 As before the experimental uncertainties on the background estimation, collected luminosity, and the model dependant signal uncertainties are accounted for in the calculation of the limit.

In the regions  $m_{\tilde{q}(\tilde{g})} - m_{LSP} < 200$  GeV and  $m_{\tilde{q}(\tilde{g})} < 350$  GeV any selection efficiency is strongly dependant on the presence of initial state radiation which is not well modelled in the Montecarlo simulation, hence these regions are not considered when setting limits

in the S.M.S models, for the model **T1tttt** the ignored region is expanded to cover  $m_{\tilde{g}} - m_{LSP} < 400$  GeV.

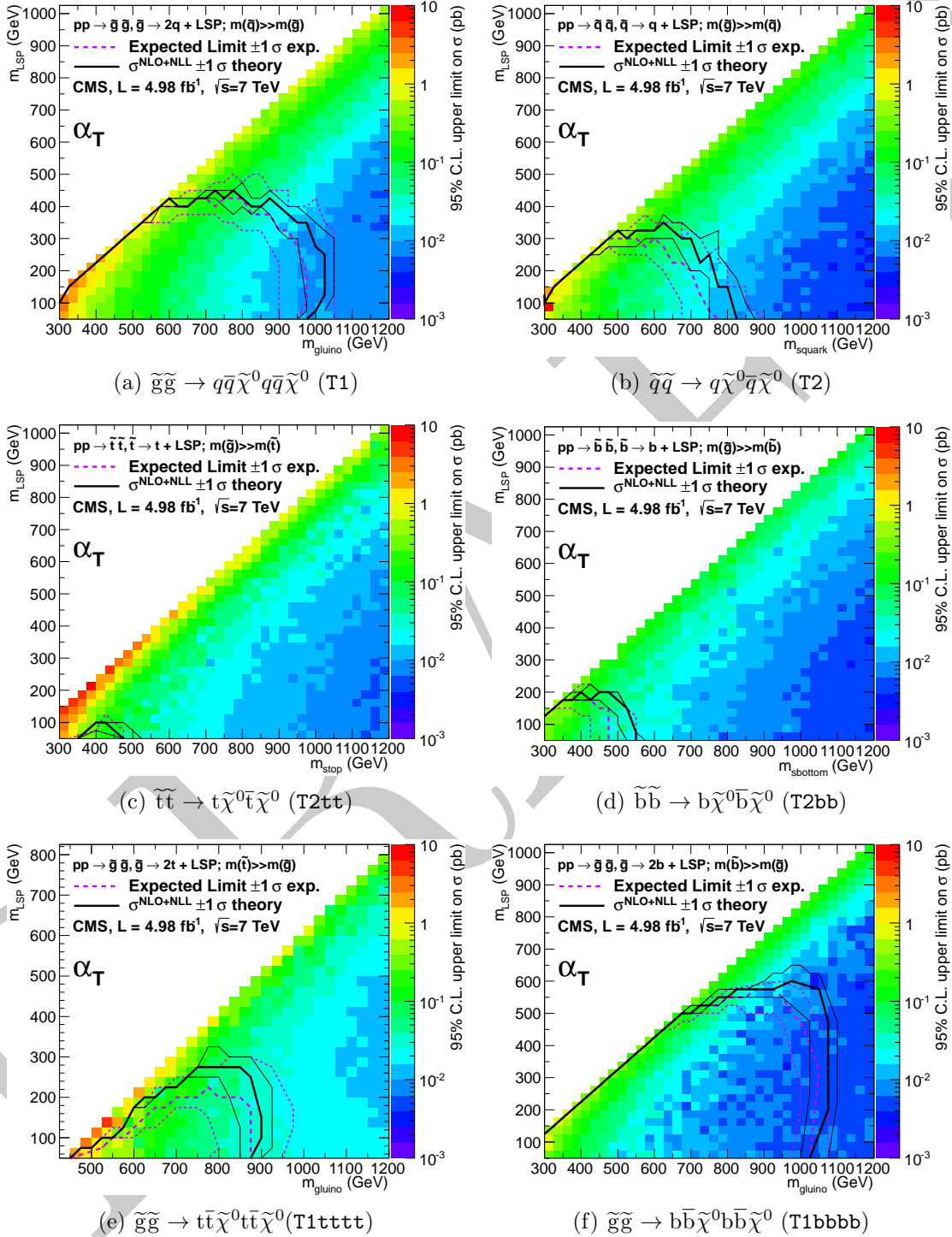
Figure 8.3 shows the observed limits at 95% confidence level obtained using  $CL_s$  as a function of  $m_{\tilde{q}(\tilde{g})}$  and  $m_{LSP}$ . The solid black lines represent the observed median limit assuming NLO+NNL[13, 32] SUSY cross sections for squark pair production in the limit of de-coupled gluinos and vice versa for the gluino production models. The thin black lines represent the limit when this cross section is varied by  $\pm 1\sigma$  of the theoretical uncertainty, the dashed purple lines represent the expected limit and its  $\pm 1\sigma$  uncertainty.

The best limits are set on the mass of the pair produced sparticles are at low  $m_{LSP}$  due to the large mass splitting between the sparticles and the LSP producing high  $p_T$  final state objects. The limits degrade as the decay spectra become compressed, above a certain  $m_{LSP}$  no limit is set.

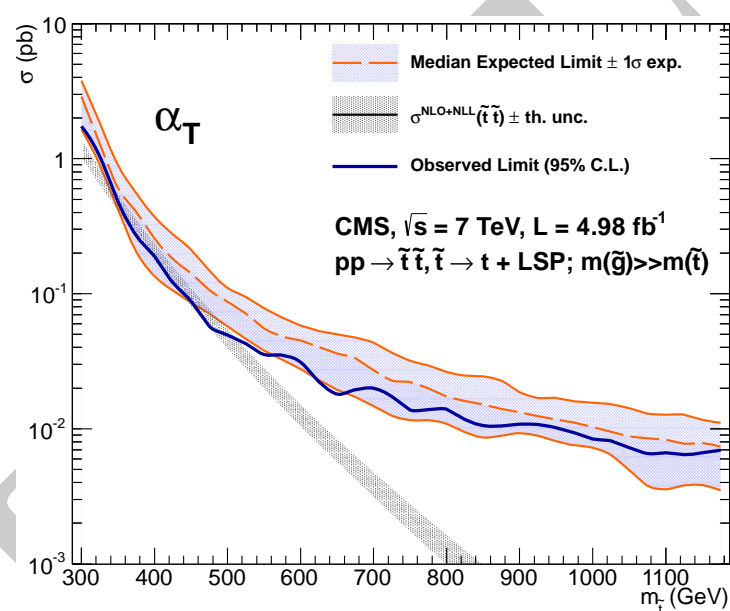
No exclusion on direct stop, stop production (**T2tt**) is expected assuming the NLO+NNL production cross section for  $m_{LSP} > 50$  GeV. Figure 8.4 shows the observed upper limit at 95% confidence level on the cross section as a function of  $m_{stop}$  for an LSP with a mass of 50 GeV.

**Table 8.2:** Production and decay modes for various simplified models.

Model	Production and decay modes	Figure showing limit
T1	$\tilde{g}\tilde{g} \rightarrow q\bar{q}\tilde{\chi}^0 q\bar{q}\tilde{\chi}^0$	8.3(a)
T2	$\tilde{q}\tilde{q} \rightarrow q\tilde{\chi}^0 \bar{q}\tilde{\chi}^0$	8.3(b)
T2tt	$\tilde{t}\tilde{t} \rightarrow t\tilde{\chi}^0 \bar{t}\tilde{\chi}^0$	8.3(c), 8.4
T2bb	$\tilde{b}\tilde{b} \rightarrow b\tilde{\chi}^0 \bar{b}\tilde{\chi}^0$	8.3(d)
T1tttt	$\tilde{g}\tilde{g} \rightarrow t\bar{t}\tilde{\chi}^0 t\bar{t}\tilde{\chi}^0$	8.3(e)
T1bbbb	$\tilde{g}\tilde{g} \rightarrow b\bar{b}\tilde{\chi}^0 b\bar{b}\tilde{\chi}^0$	8.3(f)



**Figure 8.3:** Upper limit on cross section at 95% CL as a function of  $m_{\tilde{q}}$  or  $m_{\tilde{g}}$  and  $m_{\text{LSP}}$  for various simplified models. The solid thick black line indicates the observed exclusion region assuming NLO+NNL SUSY production cross section. The thin black lines represent the observed excluded region when varying the cross section by its theoretical uncertainty. The dashed purple lines indicate the median (thick line)  $\pm 1\sigma$  (thin lines) expected exclusion regions.



**Figure 8.4:** Excluded cross section versus top squark mass for a model in which pair-produced top squarks decay to two top quarks and two neutralinos. The solid blue line indicates the observed cross section upper limit (95% CL) as a function of the top squark mass,  $m_{\tilde{t}}$ . The dashed orange line and blue band indicate the median expected excluded cross section with experimental uncertainties. The solid black line with grey band indicates the NLO+NNL SUSY top squark pair-production cross section and theoretical uncertainties.

# **Chapter 9**

## **Conclusion**

2

DRAFT

# <sup>1</sup> Bibliography

- <sup>2</sup> [1]
- <sup>3</sup> [2]
- <sup>4</sup> [3]
- <sup>5</sup> [4] Technical report.
- <sup>6</sup> [5] Updated measurements of the inclusive w and z cross sections at 7 tev. (CMS-AN-  
<sup>7</sup> 10-264), 2010.
- <sup>8</sup> [6] Search for supersymmetry with the  $\alpha_t$  variable in the 7 tev dataset of 2011. (CMS-  
<sup>9</sup> AN-11-517), 2011.
- <sup>10</sup> [7] Ecal performance plots, 2012 data. Jul 2012.
- <sup>11</sup> [8] Search for supersymmetry in final states with missing transverse energy and 0,  
<sup>12</sup> 1, 2, 3, or at least 4 b-quark jets in 8 tev pp collisions using the variable alphat.  
<sup>13</sup> (CMS-PAS-SUS-12-028), 2012.
- <sup>14</sup> [9] W Adam, R Frhwirth, A Strandlie, and T Todorov. Reconstruction of electrons  
<sup>15</sup> with the gaussian-sum filter in the cms tracker at the lhc. *Journal of Physics G: Nuclear and Particle Physics*, 31(9):N9, 2005.
- <sup>17</sup> [10] T Åkesson. The ATLAS experiment at the CERN Large Hadron Collider - CERN  
<sup>18</sup> Document Server. *Particles*, 1999.
- <sup>19</sup> [11] B Alessandro, F Antinori, J Belikov, and C Blume. ALICE: Physics performance  
<sup>20</sup> report, volume II. *Journal of Physics G: Nuclear and Particle Physics*, January  
<sup>21</sup> 2006.
- <sup>22</sup> [12] B C Allanach. SOFTSUSY: a program for calculating supersymmetric spectra.  
<sup>23</sup> *Comput. Phys. Commun.*, 143:305, 2002.

- <sup>1</sup> [13] W. Beenakker and others. Squark and gluino production at hadron colliders. *Nucl. Phys. B*, 492:51, 1997.
- <sup>3</sup> [14] Michael Benedikt, Paul Collier, V Mertens, John Poole, and Karlheinz Schindl. *LHC Design Report*. CERN, Geneva, 2004.
- <sup>5</sup> [15] Z Bern, G Diana, L J Dixon, F Febres Cordero, S Hoche, and others. Driving Missing Data at Next-to-Leading Order. *arXiv*, D84:114002, 2011.
- <sup>7</sup> [16] Michiel Botje, Jon Butterworth, Amanda Cooper-Sarkar, Albert de Roeck, Joel Feltesse, Stefano Forte, Alexander Glazov, Joey Huston, Ronan McNulty, Torbjorn Sjostrand, and Robert Thorne. The PDF4LHC Working Group Interim Recommendations. *arXiv.org*, hep-ph, January 2011.
- <sup>11</sup> [17] M Cacciari, G Salam, and G Soyez. The anti-kt jet clustering algorithm. *Journal of High Energy ...*, January 2008.
- <sup>13</sup> [18] Serguei Chatrchyan and others. Determination of Jet Energy Calibration and Transverse Momentum Resolution in CMS. *arXiv*, 6:P11002, 2011.
- <sup>15</sup> [19] CMS Collaboration. CMS b-tagging performance database. Technical report.
- <sup>16</sup> [20] CMS Collaboration. The Trigger and Data Acquisition Project Technical Design Report, Volume 1, The Level-1 Trigger. *CERN/LHCC 2000-038, CMS TDR 6.1*, 2000.
- <sup>19</sup> [21] CMS Collaboration. Data-Driven Estimation of the Invisible Z Background to the SUSY MET Plus Jets Search. Technical report, 2008.
- <sup>21</sup> [22] CMS Collaboration. SUSY searches with dijet events. Technical report, 2008.
- <sup>22</sup> [23] CMS Collaboration. Search strategy for exclusive multi-jet events from supersymmetry at CMS. Technical report, 2009.
- <sup>24</sup> [24] CMS Collaboration. Electron reconstruction and identification at  $\sqrt{s} = 7$  TeV. Technical report, 2010.
- <sup>26</sup> [25] CMS Collaboration. Isolated Photon Reconstruction and Identification at  $\sqrt{s} = 7$  TeV. Technical report, 2010.
- <sup>28</sup> [26] CMS Collaboration. Performance of muon identification in pp collisions at  $\sqrt{s} = 7$  TeV. Technical report, 2010.

- <sup>1</sup> [27] The CMS Collaboration. CMS - The Compact Muon Solenoid. January 1996.
- <sup>2</sup> [28] The CMS Collaboration. Cms physics technical design report, volume ii: Physics performance. *Journal of Physics G: Nuclear and Particle Physics*, 34(6):995, 2007.
- <sup>4</sup> [29] The C.M.S Collaboration. Cms tracking performance results from early lhc operation. *Eur. Phys. J. C*, 70(arXiv:1007.1988. CERN-PH-EP-2010-019. CMS-TRK-10-001):1165. 29 p, Jul 2010.
- <sup>7</sup> [30] The CMS collaboration. Determination of jet energy calibration and transverse momentum resolution in cms. *Journal of Instrumentation*, 6(11):P11002, 2011.
- <sup>9</sup> [31] Frederic James. MINUIT Reference Manual. *CERN Program Library Writeup*, D506.
- <sup>11</sup> [32] M Kr amer, A Kulesza, R van der Leeuw, and others. Supersymmetry production cross sections in pp collisions at  $\sqrt{s} = 7$  TeV. *arXiv*.
- <sup>13</sup> [33] Edward Matthew Laird. A Search for Squarks and Gluinos with the CMS Detector. 2012.
- <sup>15</sup> [34] J Marrouche and others. Commissioning the CMS Global Calorimeter Trigger. *CMS IN*, 2010/029, 2010.
- <sup>17</sup> [35] Belasco Cranmer Moneta and others. The RooStats Project. *Proceedings of Science*, 2010.
- <sup>19</sup> [36] K Nakamura. Review of particle physics. *J. Phys. G*, 37:075021, 2010.
- <sup>20</sup> [37] J Rademacker. LHCb: Status and Physics Prospects. *Arxiv preprint hep-ex*, January 2005.
- <sup>22</sup> [38] Lisa Randall and David Tucker-Smith. Dijet Searches for Supersymmetry at the LHC. *arXiv*, hep-ph, January 2008.
- <sup>24</sup> [39] WH Smith, Ph Busson, S Dasu, J Hauser, G Heath, J Krolikowski, J Varela, A Taurok, G Wrochna, and P Zotto. Cms phyiscs technical design report: The trigger system. 1:1–630, Dec 2000.
- <sup>27</sup> [40] Daniel Stump, Joey Huston, Jon Pumplin, Wu-Ki Tung, H.L. Lai, et al. Inclusive jet production, parton distributions, and the search for new physics. *JHEP*, 0310:046, 2003.

- <sup>1</sup> [41] S Mrenna T. Sjöstrand and P Z Skands. PYTHIA 6.4 Physics and Manual. *JHEP*,  
<sup>2</sup> 05:026, 2006.
- <sup>3</sup> [42] R.S. Thorne, A.D. Martin, W.J. Stirling, and G. Watt. Status of MRST/MSTW  
<sup>4</sup> PDF sets. 2009.
- <sup>5</sup> [43] Maria Ubiali, Richard D. Ball, Luigi Del Debbio, Stefano Forte, Alberto Guffanti,  
<sup>6</sup> et al. Combined PDF and strong coupling uncertainties at the LHC with NNPDF2.0.  
<sup>7</sup> 2010.
- <sup>8</sup> [44] C Wulz. The CMS experiment at CERN. *cdsweb.cern.ch*.

## <sup>1</sup> 1 Additional information on triggers

**Table 1:** List of HT triggers used.

$H_T$ bin (GeV)	Trigger
$275 < H_T < 325$	HLT-HT250_v*
$325 < H_T < 375$	HLT-HT300_v*
$375 < H_T < 475$	HLT-HT350_v*
$H_T > 475$	HLT-HT400_v*

**Table 2:** List of  $\alpha_T$  triggers used.

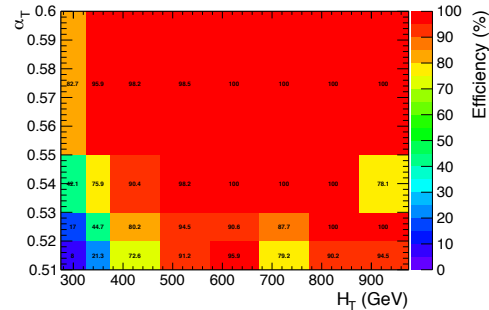
$275 < H_T < 325 GeV$	$325 < H_T < 375 GeV$
HLT-HT250_AlphaT0p53_v*	HLT-HT300_AlphaT0p52_v*
HLT-HT250_AlphaT0p55_v*	HLT-HT300_AlphaT0p53_v*
HLT-HT250_AlphaT0p58_v*	HLT-HT300_AlphaT0p54_v*
HLT-HT250_AlphaT0p60_v*	HLT-HT300_AlphaT0p55_v*
$375 < H_T < 475 GeV$	$H_T > 475 GeV$
HLT-HT350_AlphaT0p51_v*	HLT-HT400_AlphaT0p51_v*
HLT-HT350_AlphaT0p52_v*	HLT-HT400_AlphaT0p52_v*
HLT-HT350_AlphaT0p52_v*	
HLT-HT350_AlphaT0p53_v*	

**Table 3:** List of Mu-HT triggers used.

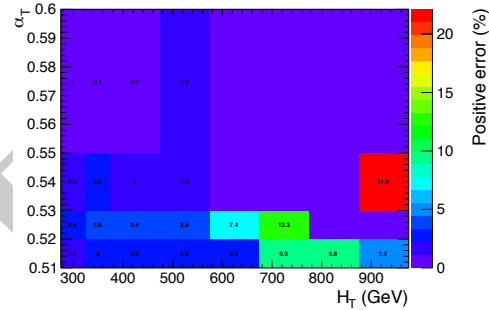
$H_T > 275 GeV$	$H_T > 375 GeV$
HLT_Mu5-HT200_v*	HLT_Mu5-HT200_v*
HLT_Mu8-HT200_v*	HLT_Mu8-HT200_v*
HLT_Mu15-HT200_v*	HLT_Mu15-HT200_v*
HLT_Mu30-HT200_v*	HLT_Mu30-HT200_v*
HLT_Mu40-HT200_v*	HLT_Mu40-HT200_v*
	HLT_Mu40-HT300_v*

**Table 4:** List of Photon triggers used.

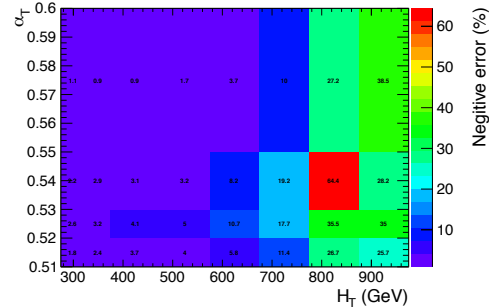
$H_T > 375 GeV$
HLT_Photon75_CaloIdVL_v*
HLT_Photon75_CaloIdVL_IsoL_v*
HLT_Photon90_CaloIdVL_v*
HLT_Photon90_CaloIdVL_IsoL_v*
HLT_Photon125_v*
HLT_Photon135_v*



(a) Efficiency (%)

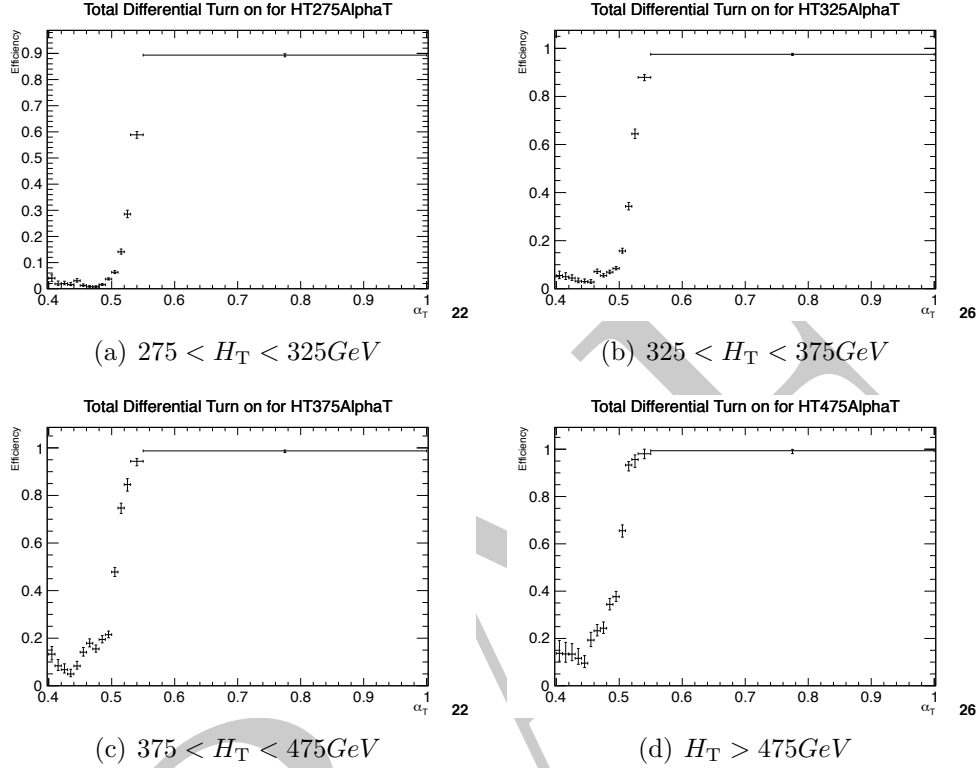


(b) Positive error (%)

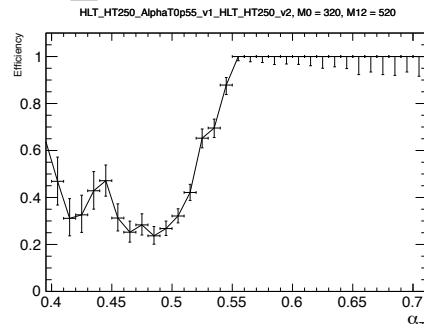


(c) Negative error (%)

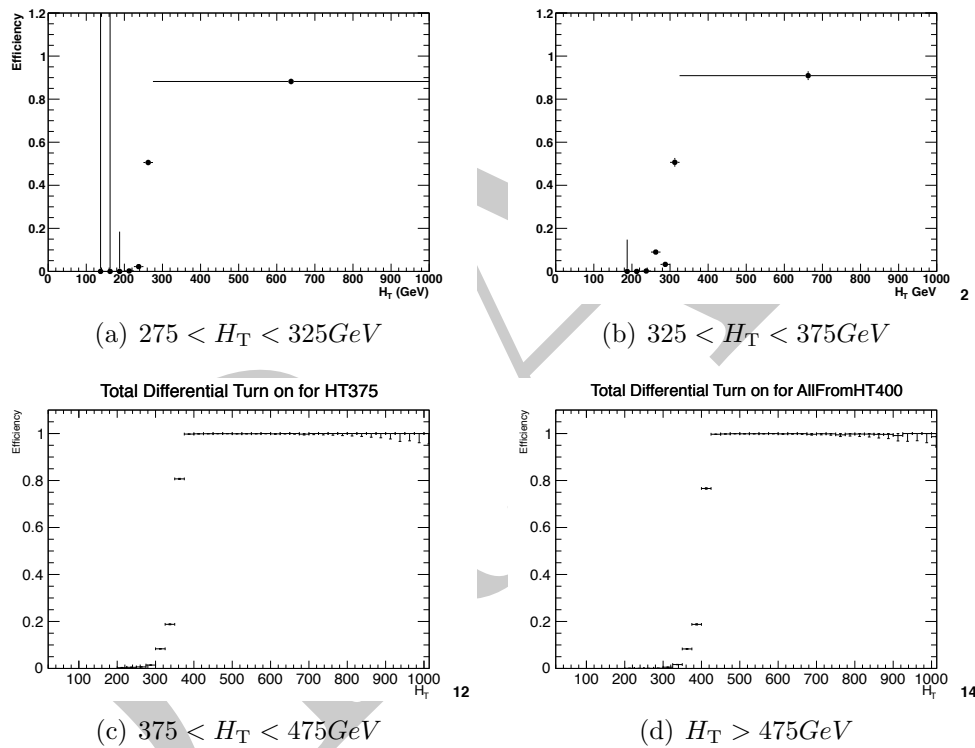
**Figure 1:** Efficiency and associated errors of the  $\alpha_T$  trigger in offline bins of  $H_T$  and  $\alpha_T$ .



**Figure 2:** Efficiency turn-on curves for the  $\alpha_T$  triggers used to collect events for four different HT regions.



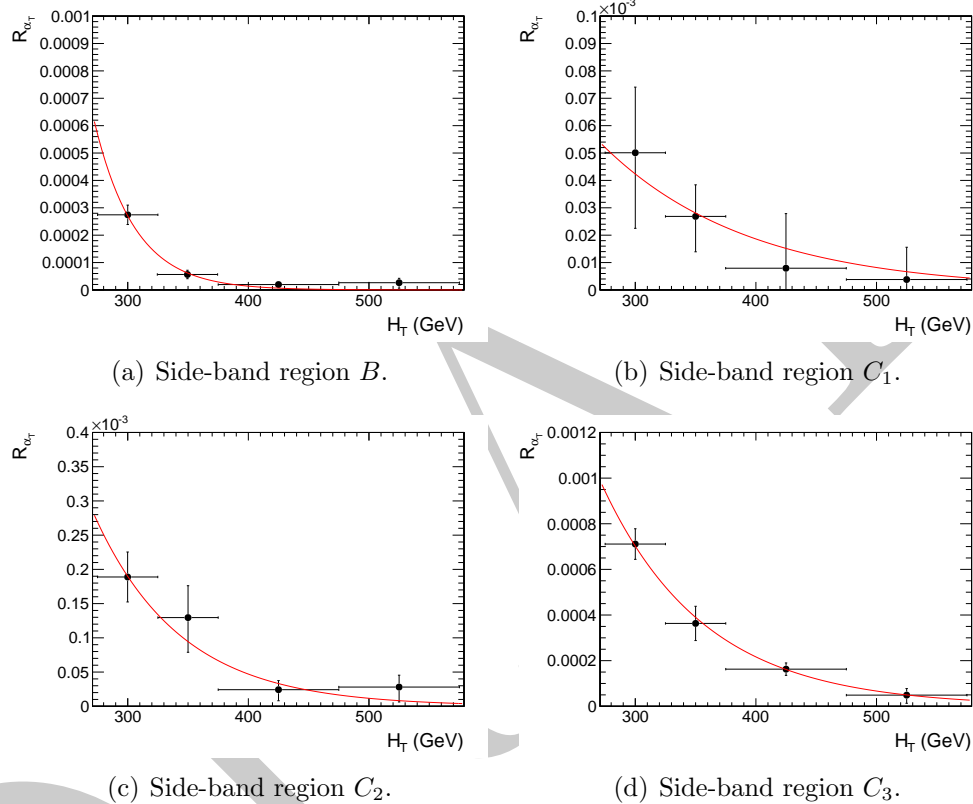
**Figure 3:** Efficiency turn-on curve for the representative model RM1, with  $m_0 = 320 \text{ GeV}$  and  $m_{1/2} = 520 \text{ GeV}$ , using the  $\alpha_T$  trigger with thresholds  $H_T > 250 \text{ GeV}$  and  $\alpha_T > 0.55$  and an offline signal region defined by  $H_T > 275 \text{ GeV}$  and  $\alpha_T > 0.55$ .



**Figure 4:** Efficiency turn-on curves for the  $H_T$  triggers used to collect events for four different  $H_T$  regions.

## 2 Addition information on background estimation methods

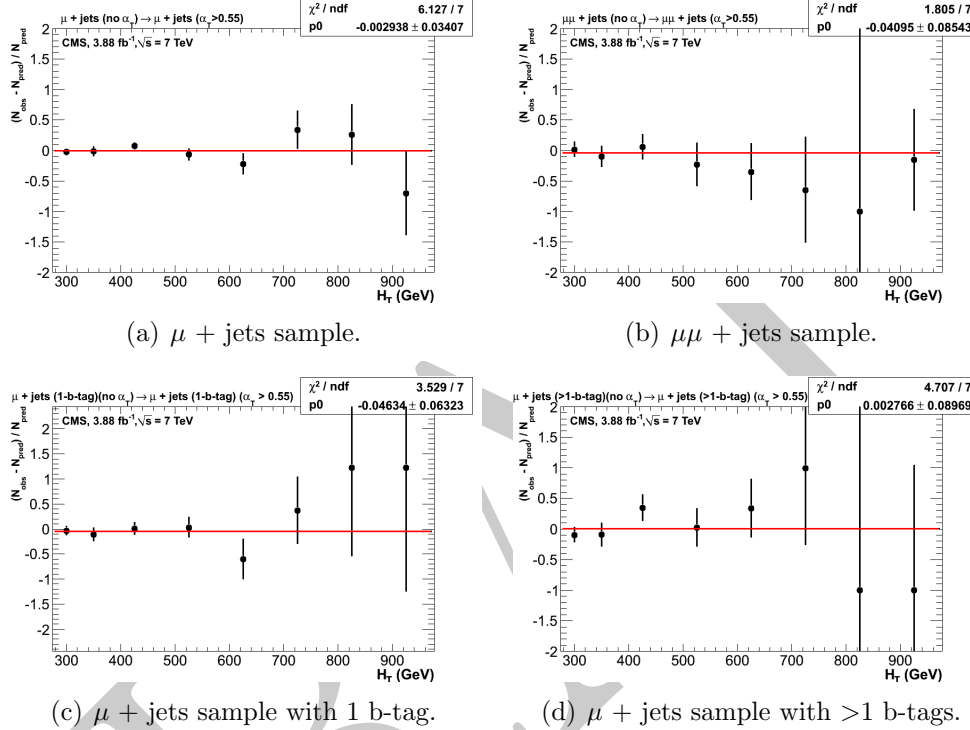
### 2.1 Determination of $k_{QCD}$



**Figure 5:**  $R_{\alpha_T}(H_T)$  and exponential fit for various data side-bands. Linear y-axis scale.

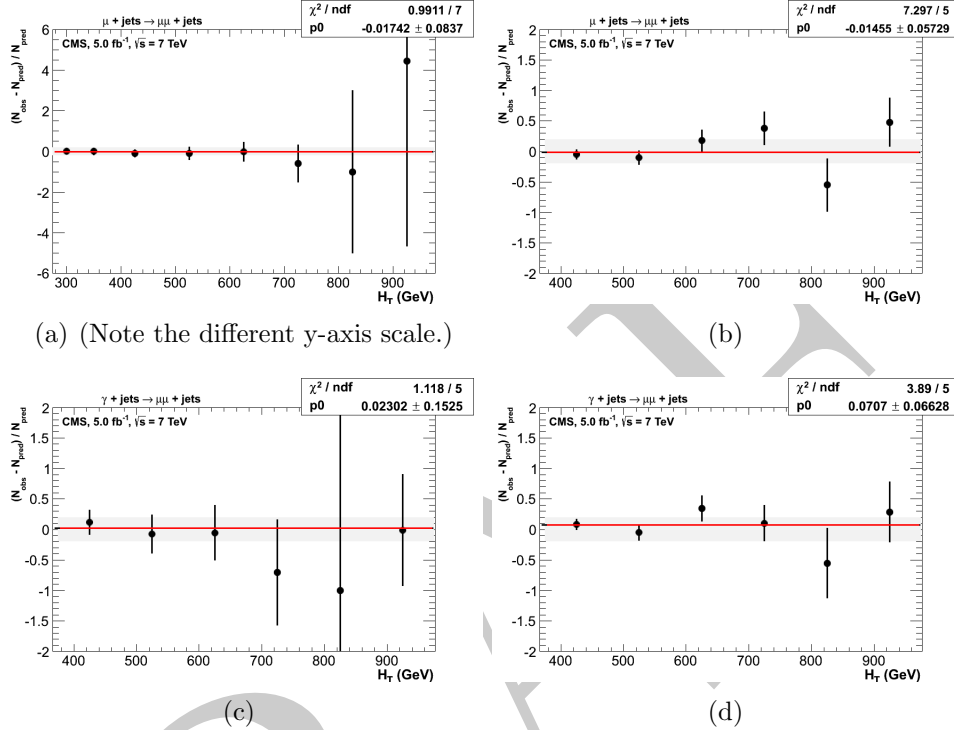
### 3 Closure tests and systematic uncertainties

#### 3.1 Defining muon samples without an $\alpha_T$ requirement



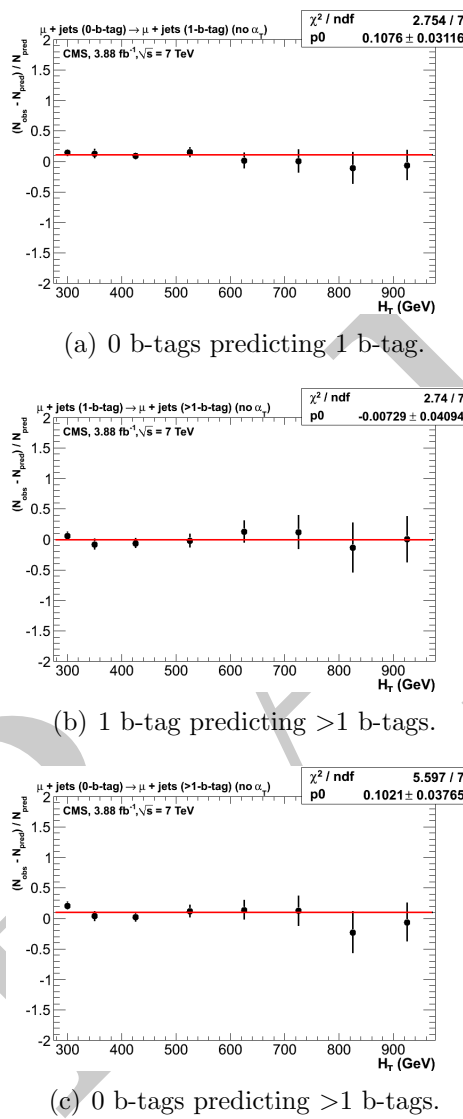
**Figure 6:** Closure tests that demonstrate the MC modelling of the  $\alpha_T$  acceptance. The closure tests are performed for both the inclusive analysis with (a) the  $\mu + \text{jets}$  sample and (b) the  $\mu\mu + \text{jets}$  control sample. Similar tests are performed for the b-tag analysis using (a) the  $\mu + \text{jets}$  sample and a requirement of exactly one b-tag, and (b) the  $\mu + \text{jets}$  sample and a requirement of at least two b-tags. The red lines indicate the constant best fit value across all  $H_T$  bins.

### 3.2 Closure tests for inclusive analysis

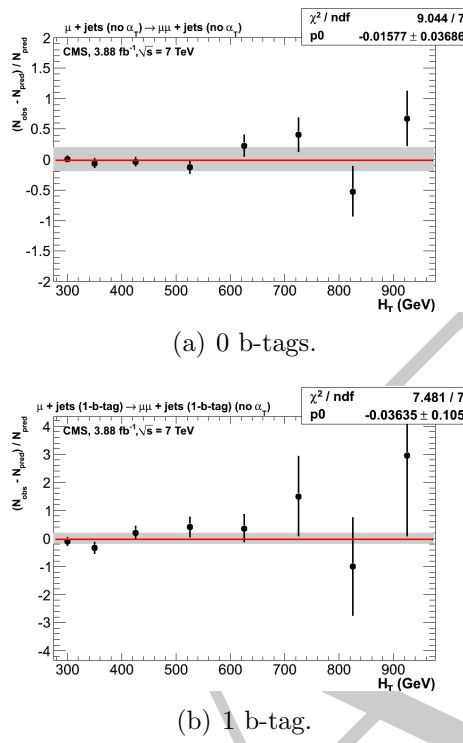


**Figure 7:** Closure tests using yields from one control to predict yields in another sample. The two plots on the left show closure tests which use “low stats” muon samples recorded with the `HT_AlphaT` triggers and defined by offline selection criteria that include an  $\alpha_T$  requirement: (a)  $\mu + \text{jets} \rightarrow \mu\mu + \text{jets}$  sample and (c)  $\gamma + \text{jets} \rightarrow \mu\mu + \text{jets}$  sample. Similarly, the plots on the right show the same closure tests but using “high-stats” muon samples recorded with `Mu_HT` triggers and defined with no offline  $\alpha_T$  requirement. The same tests are performed: (b)  $\mu + \text{jets} \rightarrow \mu\mu + \text{jets}$  sample and (d)  $\gamma + \text{jets} \rightarrow \mu\mu + \text{jets}$  sample. These closure tests are only possible for the six highest  $H_T$  bins due to the trigger conditions. The red lines indicate the constant best fit value across all  $H_T$  bins.

### 3.3 Closure tests for b-tag analysis

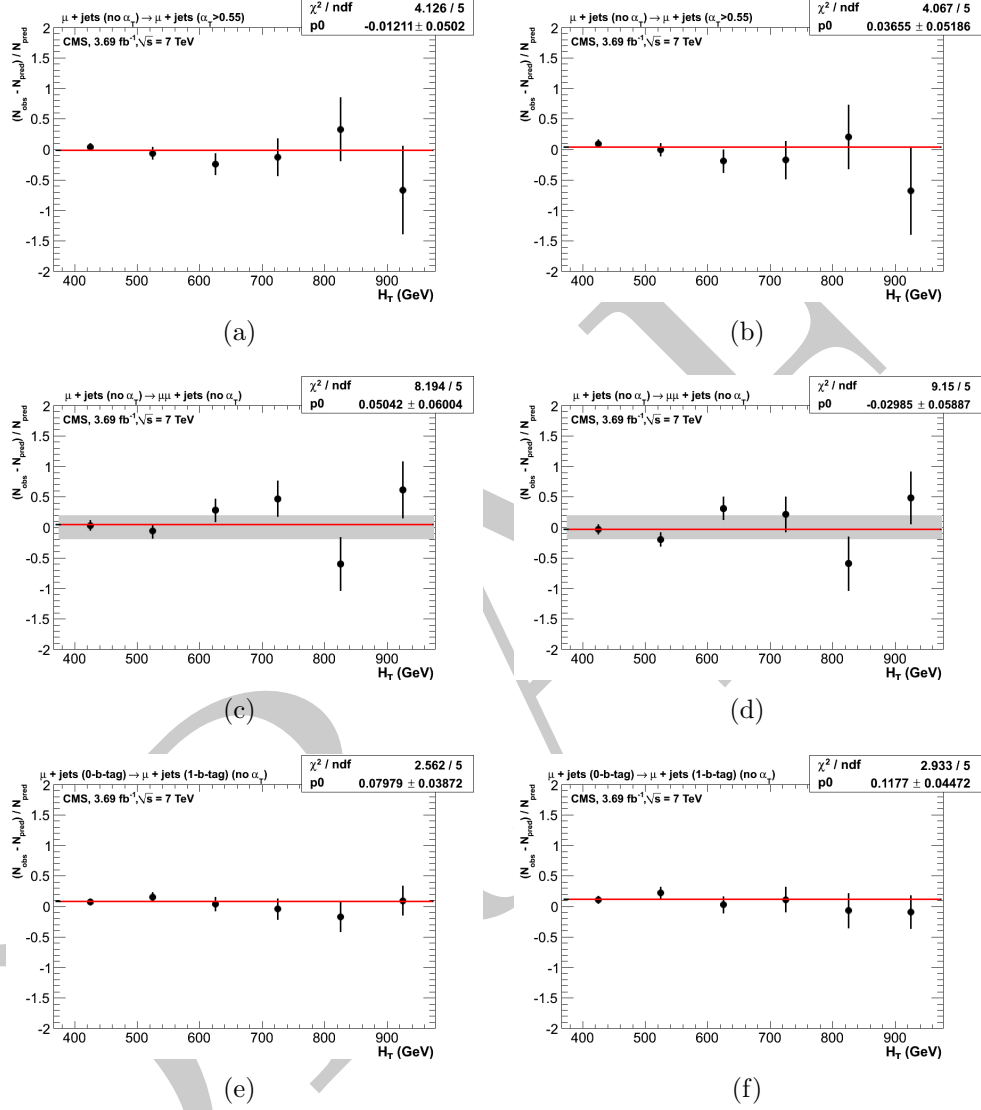


**Figure 8:** Closure tests with the  $\mu + \text{jets}$  sample that demonstrate the MC modelling of the b-tagging algorithm and of different sample compositions by for different b-tag multiplicities: (a) 0 b-tags  $\rightarrow$  1 b-tag, (b) 1 b-tags  $\rightarrow \geq 2$  b-tags, (c) 0 b-tags  $\rightarrow \geq 2$  b-tags.



**Figure 9:** Closure tests using the  $\mu + \text{jets}$  sample to predict the yields in a  $\mu\mu + \text{jets}$  sample, for events with (a) exactly 0-b-tags and (b) exactly 1-b-tags.

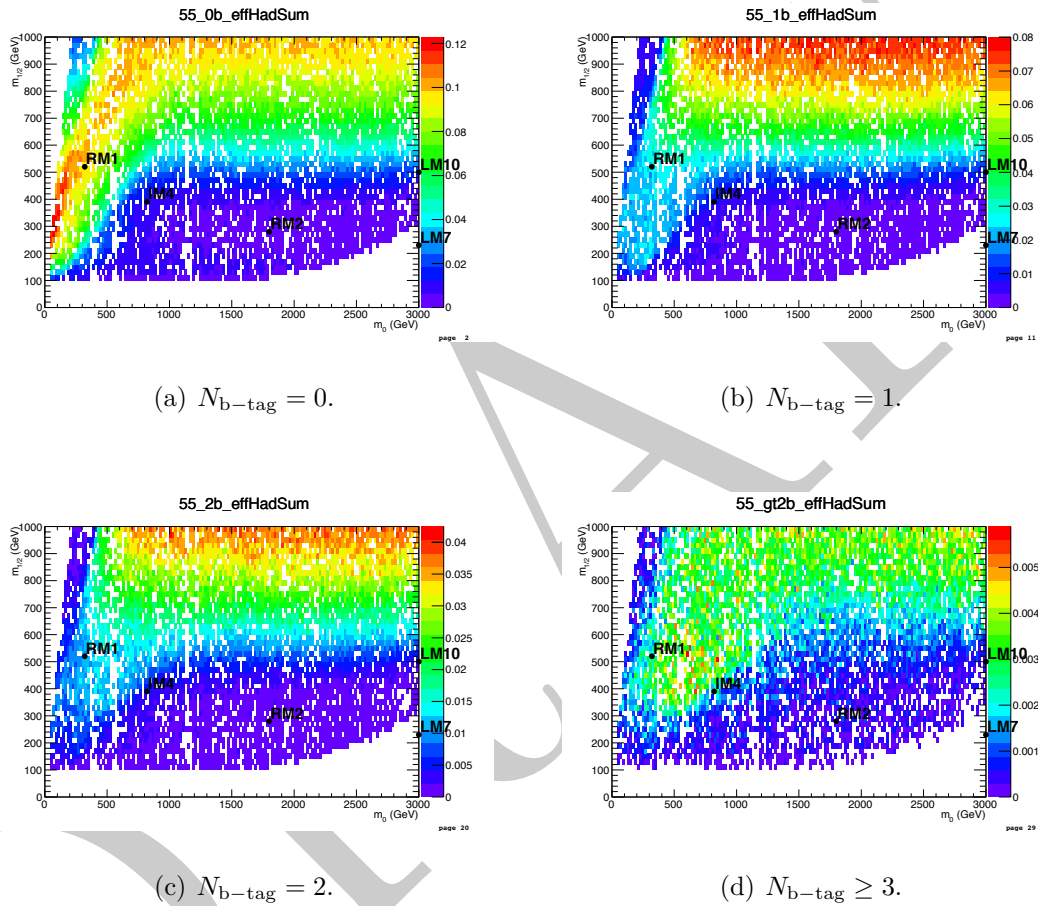
### 3.4 Closure tests concerning pile-up



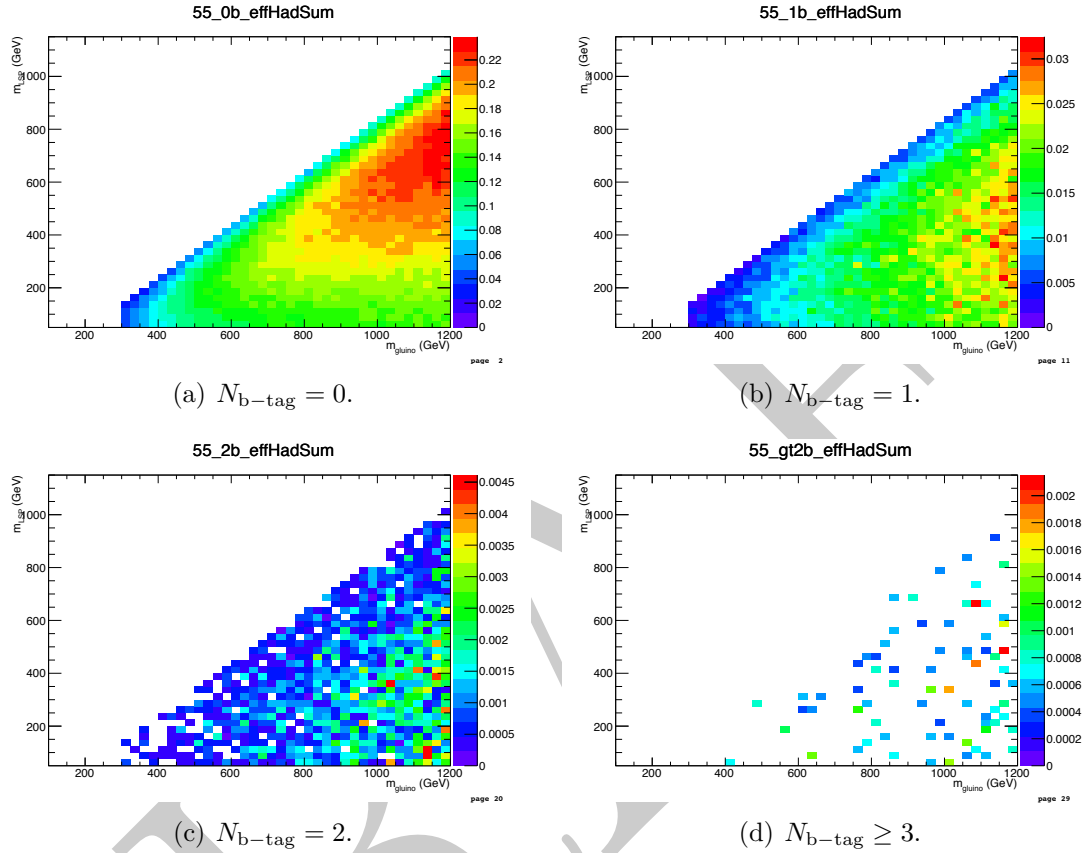
**Figure 10:** Closure tests using yields from one control to predict yields in another sample. The three plots on the left show closure tests from the inclusive analysis, which uses jets that are not corrected for the effects of pile-up. On the right, the jets in the analysis *are* corrected for pile-up effects by applying the `L10offset` jet energy correction. The three closure tests are: probing the MC modelling of the  $\alpha_T$  acceptance with the  $\mu + \text{jets}$  sample (a) without and (b) with `L10offset` jet energy corrections; using the  $\mu + \text{jets}$  sample to predict yields in the  $\mu\mu + \text{jets}$  sample (a) without and (b) with `L10offset` jet energy corrections; and using a 0 b-tagged  $\mu + \text{jets}$  sample to predict yields in a 1 b-tagged  $\mu + \text{jets}$  sample (a) without and (b) with `L10offset` jet energy corrections. The red lines indicate the constant best fit value across all  $H_T$  bins.

## 4 Signal efficiency

### 4.1 CMSSM

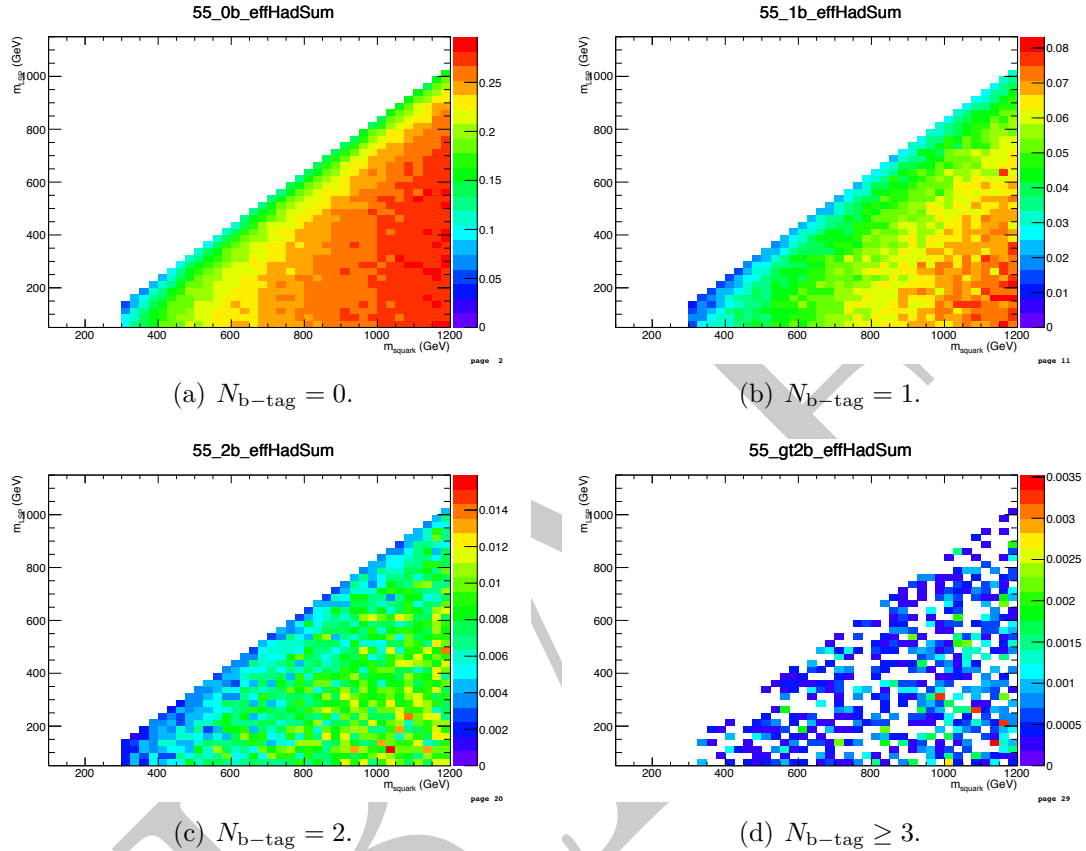


**Figure 11:** Signal efficiency in the  $(m_0, m_{1/2})$  plane of the CMSSM, of the full hadronic signal selection, integrating over all eight  $H_T$  bins and requiring (a) exactly zero, (b) exactly one, (c) exactly two, and (d) at least three b-tags per event.

<sup>1</sup> **4.2 T1**


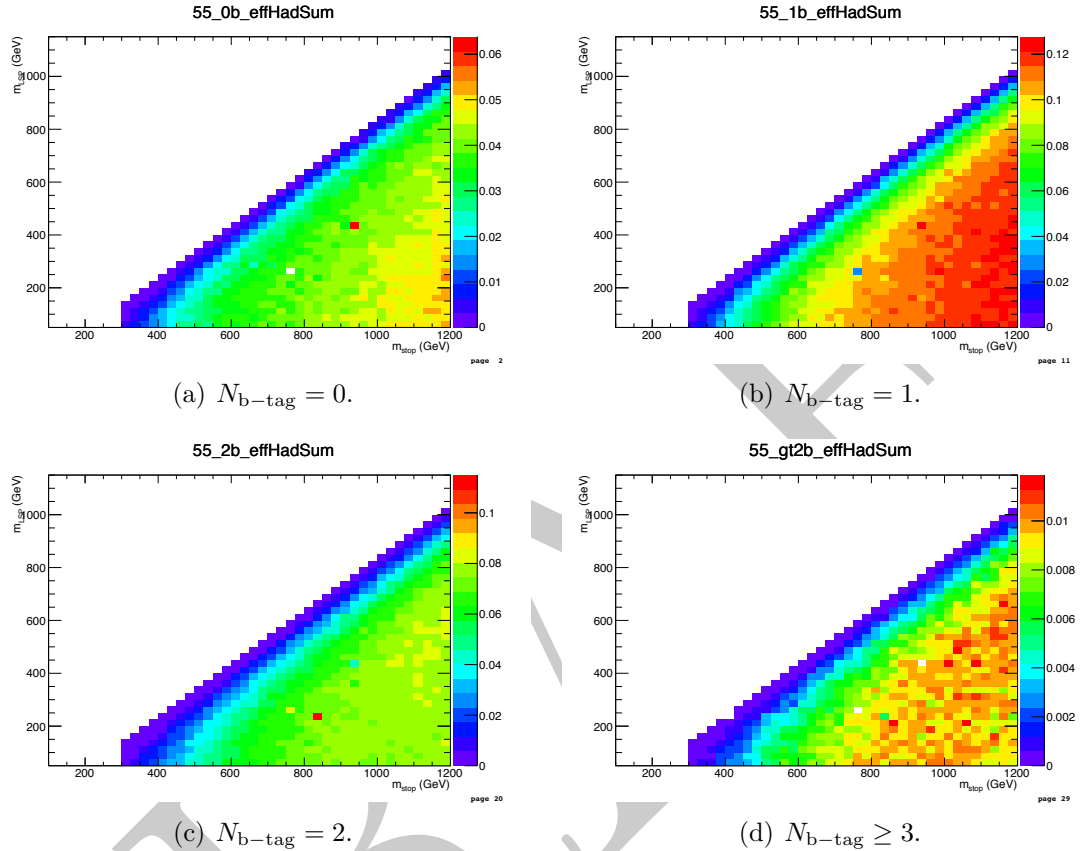
**Figure 12:** Signal efficiency in the  $(m_{\text{gl}}, m_{\text{LSP}})$  plane of the T1 simplified model, of the full hadronic signal selection, integrating over all eight  $H_T$  bins and requiring (a) exactly zero, (b) exactly one, (c) exactly two, and (d) at least three b-tags per event.

### 1 4.3 T2



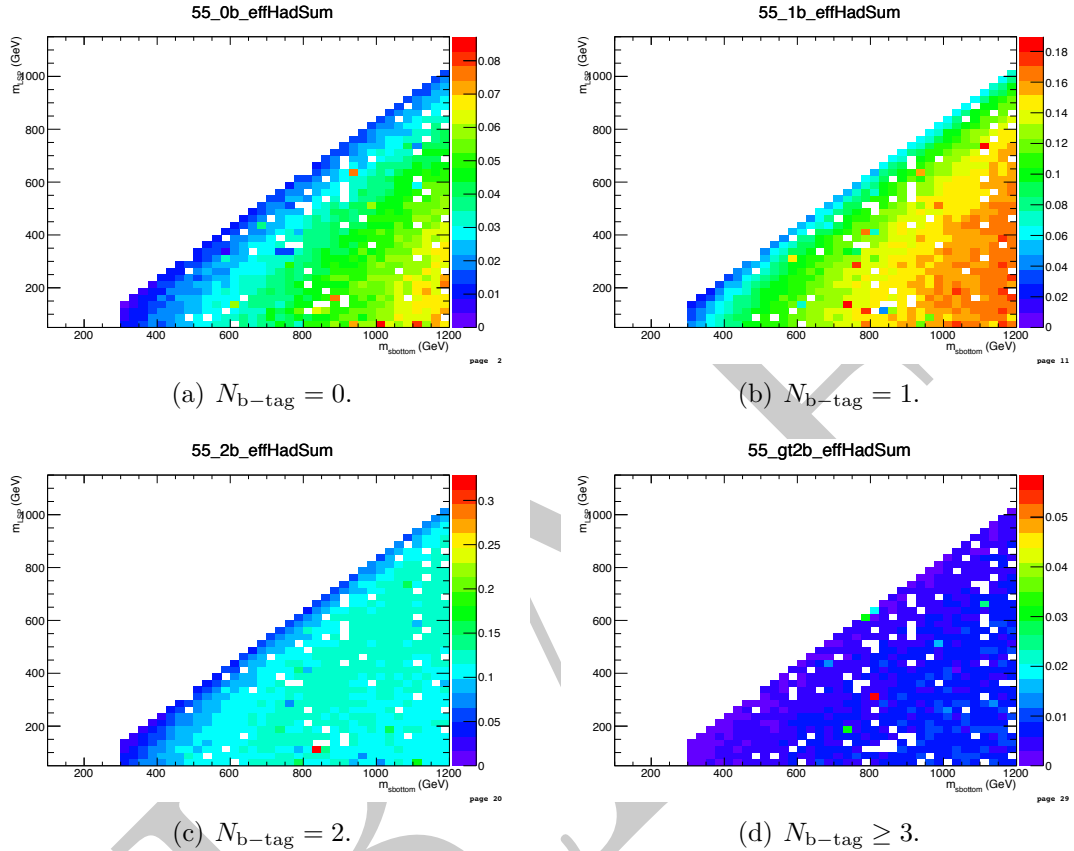
**Figure 13:** Signal efficiency in the  $(m_{\text{sq}}, m_{\text{LSP}})$  plane of the T2 simplified model, of the full hadronic signal selection, integrating over all eight  $H_T$  bins and requiring (a) exactly zero, (b) exactly one, (c) exactly two, and (d) at least three b-tags per event.

## 4.4 T2tt



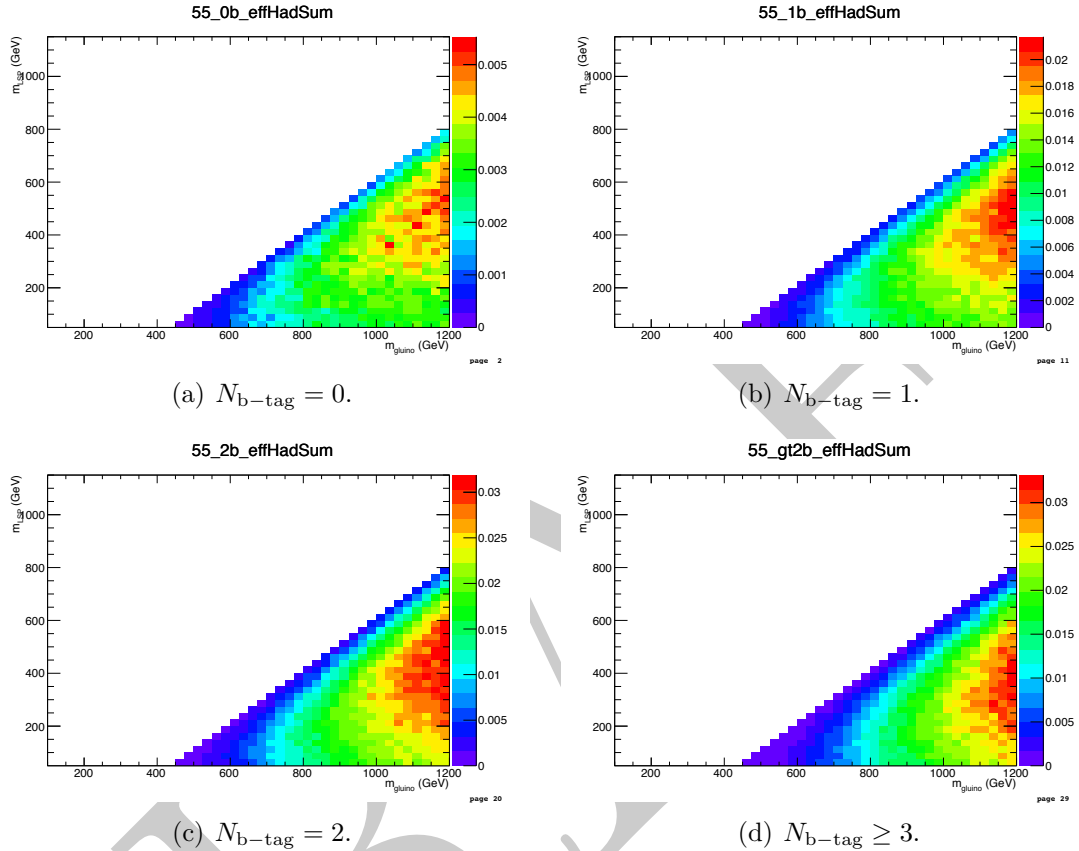
**Figure 14:** Signal efficiency in the  $(m_{sq}, m_{LSP})$  plane of the T2tt simplified model, of the full hadronic signal selection, integrating over all eight  $H_T$  bins and requiring (a) exactly zero, (b) exactly one, (c) exactly two, and (d) at least three b-tags per event.

## 4.5 T2bb



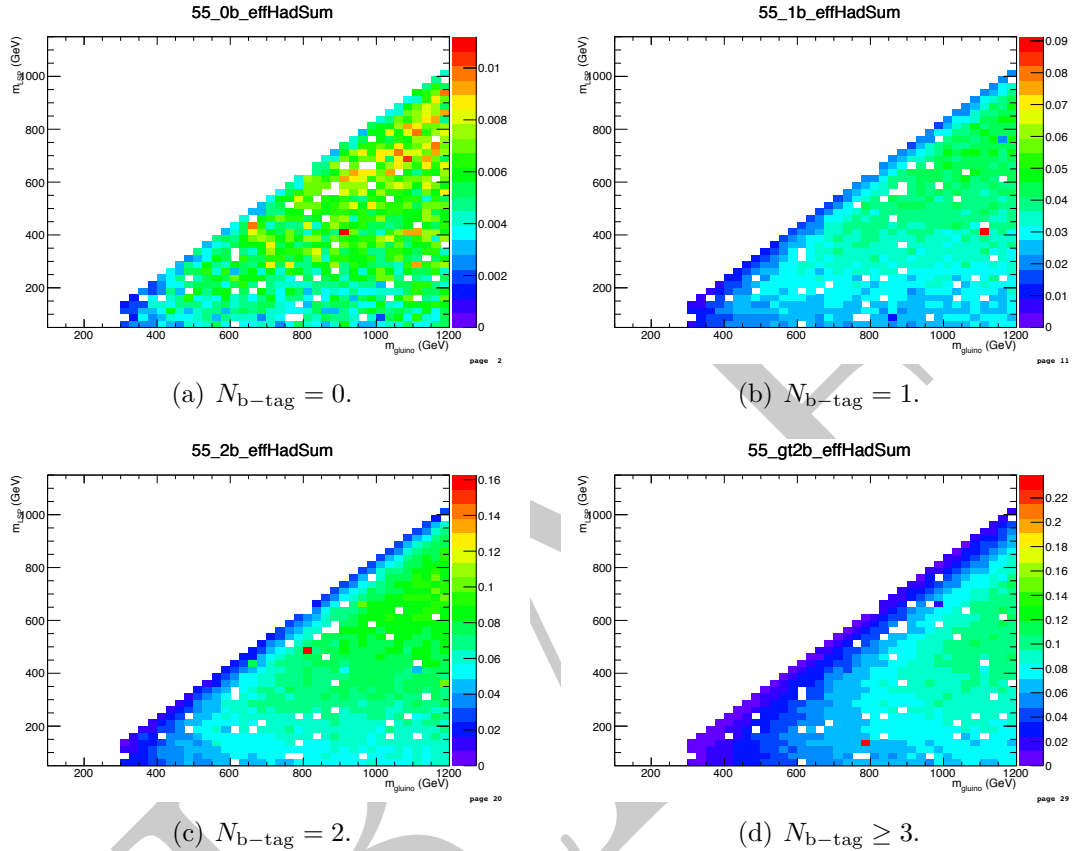
**Figure 15:** Signal efficiency in the  $(m_{sq}, m_{LSP})$  plane of the T2bb simplified model, of the full hadronic signal selection, integrating over all eight  $H_T$  bins and requiring (a) exactly zero, (b) exactly one, (c) exactly two, and (d) at least three b-tags per event.

## 1 4.6 T1tttt



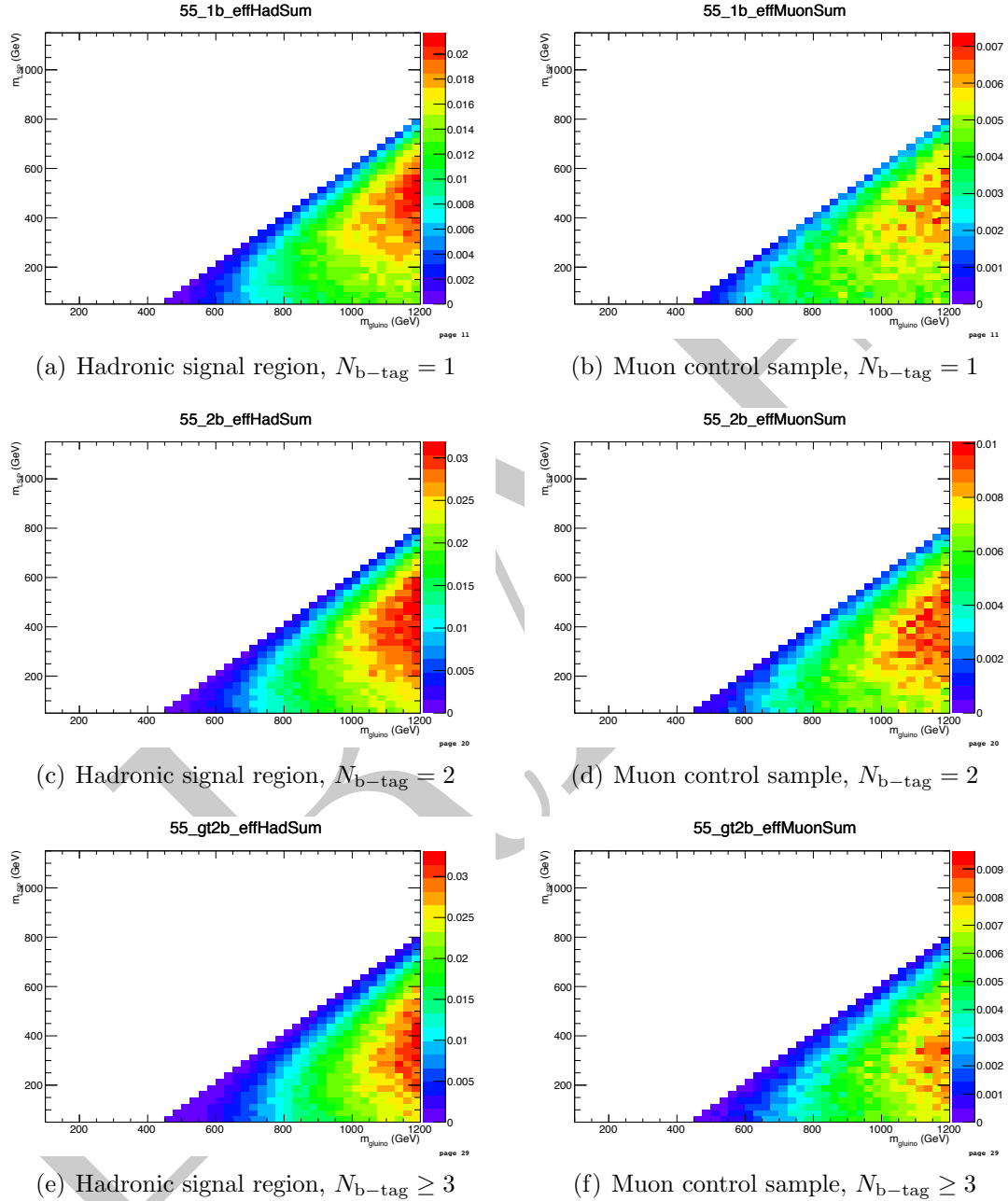
**Figure 16:** Signal efficiency in the  $(m_{\text{glino}}, m_{\text{LSP}})$  plane of the T1tttt simplified model, of the full hadronic signal selection, integrating over all eight  $H_T$  bins and requiring (a) exactly zero, (b) exactly one, (c) exactly two, and (d) at least three b-tags per event.

## 4.7 T1bbbb



**Figure 17:** Signal efficiency in the  $(m_{\text{gl}}, m_{\text{LSP}})$  plane of the T1bbbb simplified model, of the full hadronic signal selection, integrating over all eight  $H_T$  bins and requiring (a) exactly zero, (b) exactly one, (c) exactly two, and (d) at least three b-tags per event.

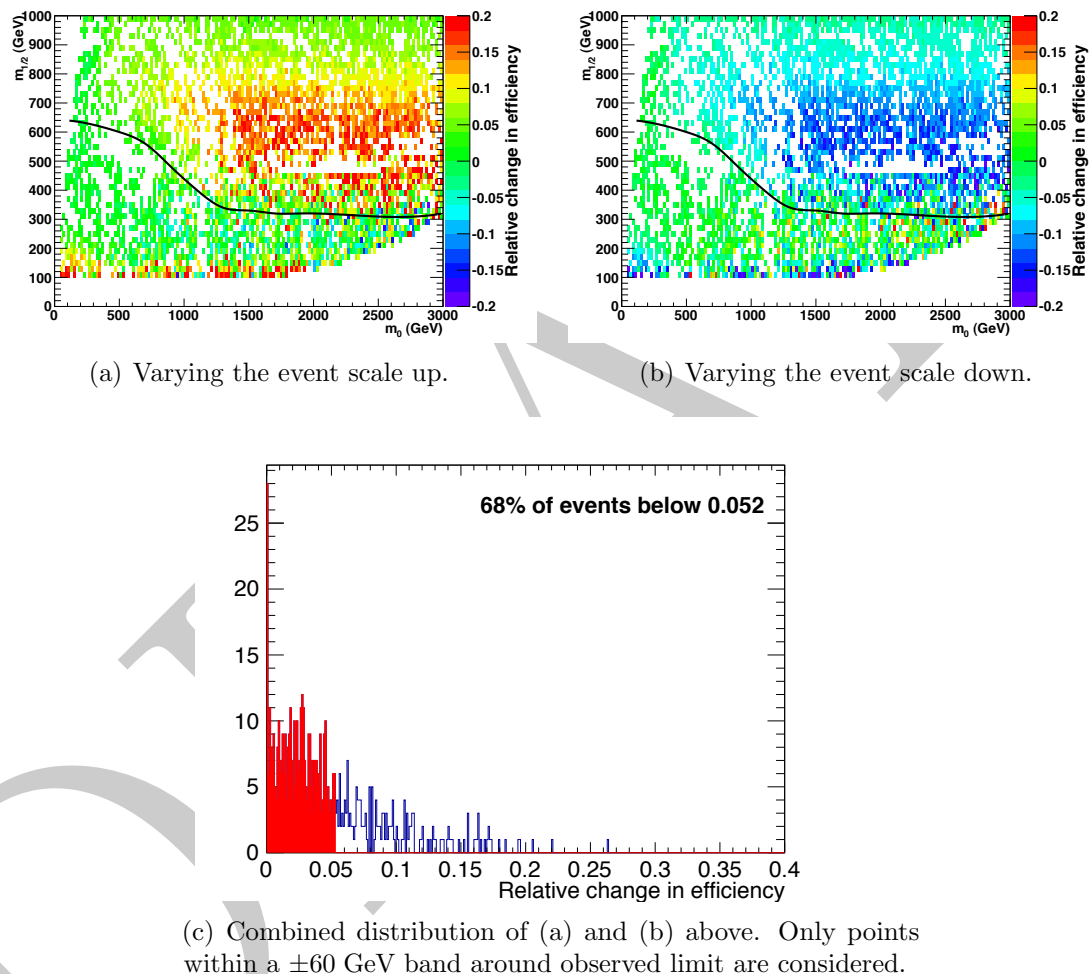
## 4.8 Signal contamination for T1tttt



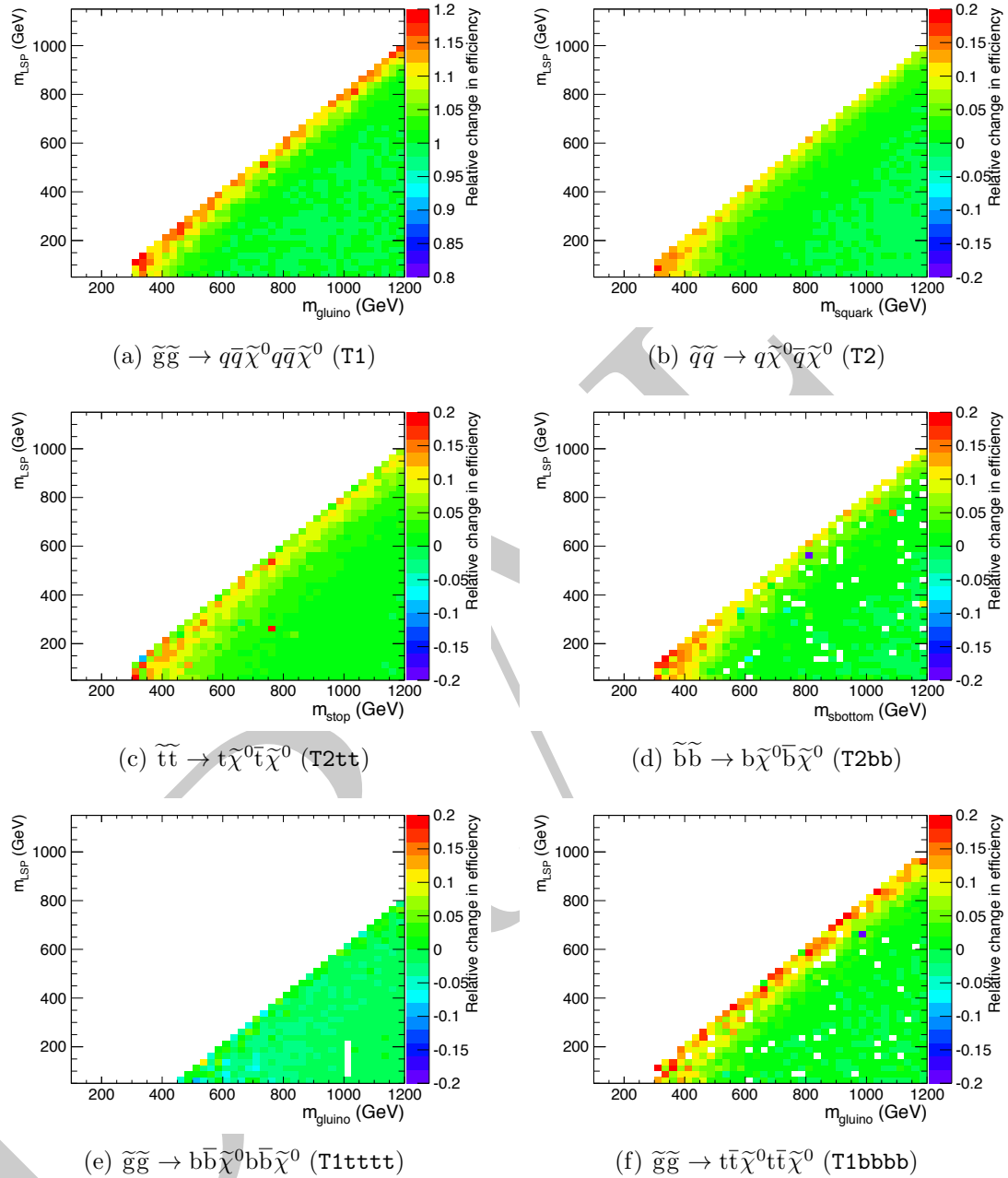
**Figure 18:** Signal efficiency in the planes of simplified model T1tttt, of the (left) hadronic signal sample selection or (right) single muon control sample selection, integrating over all eight  $H_T$  bins and requiring (top) exactly one, (middle) exactly two, or (bottom) at least three b-tags per event.

## 1 5 Experimental systematic uncertainties on signal 2 efficiency times acceptance

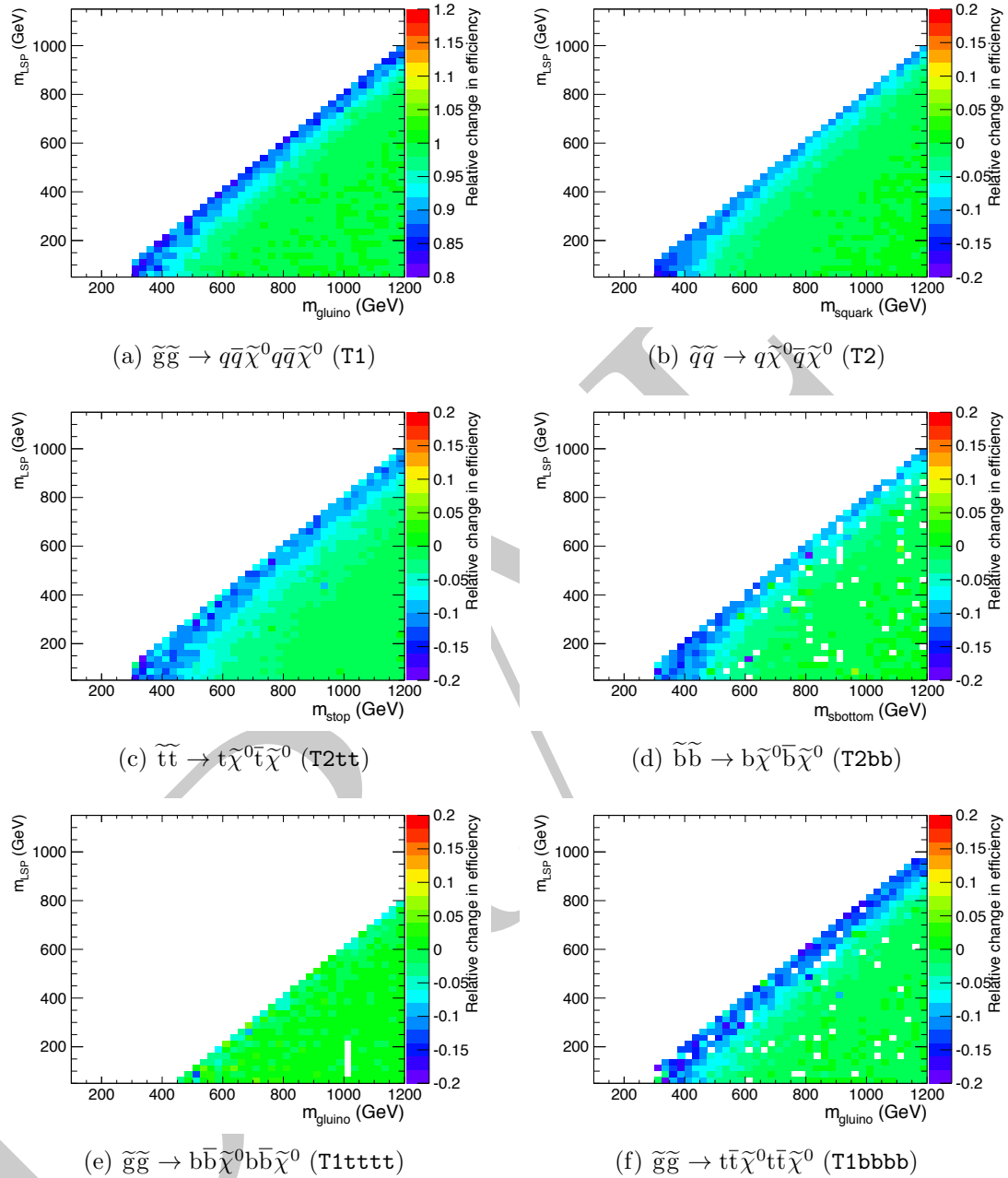
### 3 5.1 Systematics due to jet energy scale uncertainties



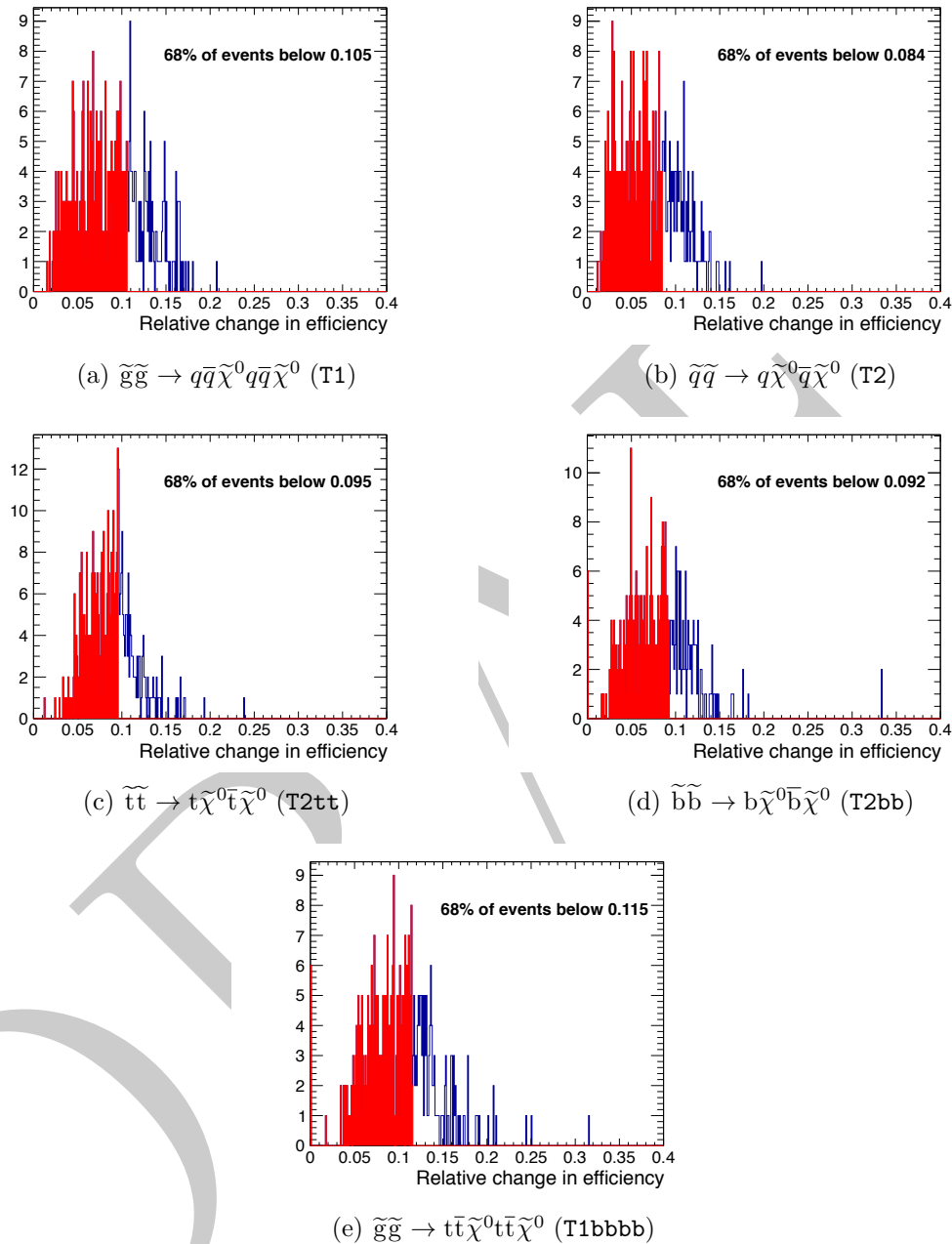
**Figure 19:** The effect of jet energy scale variations on signal efficiency in the CMSSM plane. All plots show the relative change in efficiency. No requirement is made on the number of reconstructed b jets. The red shaded area is bounded by the 68<sup>th</sup> percentile.



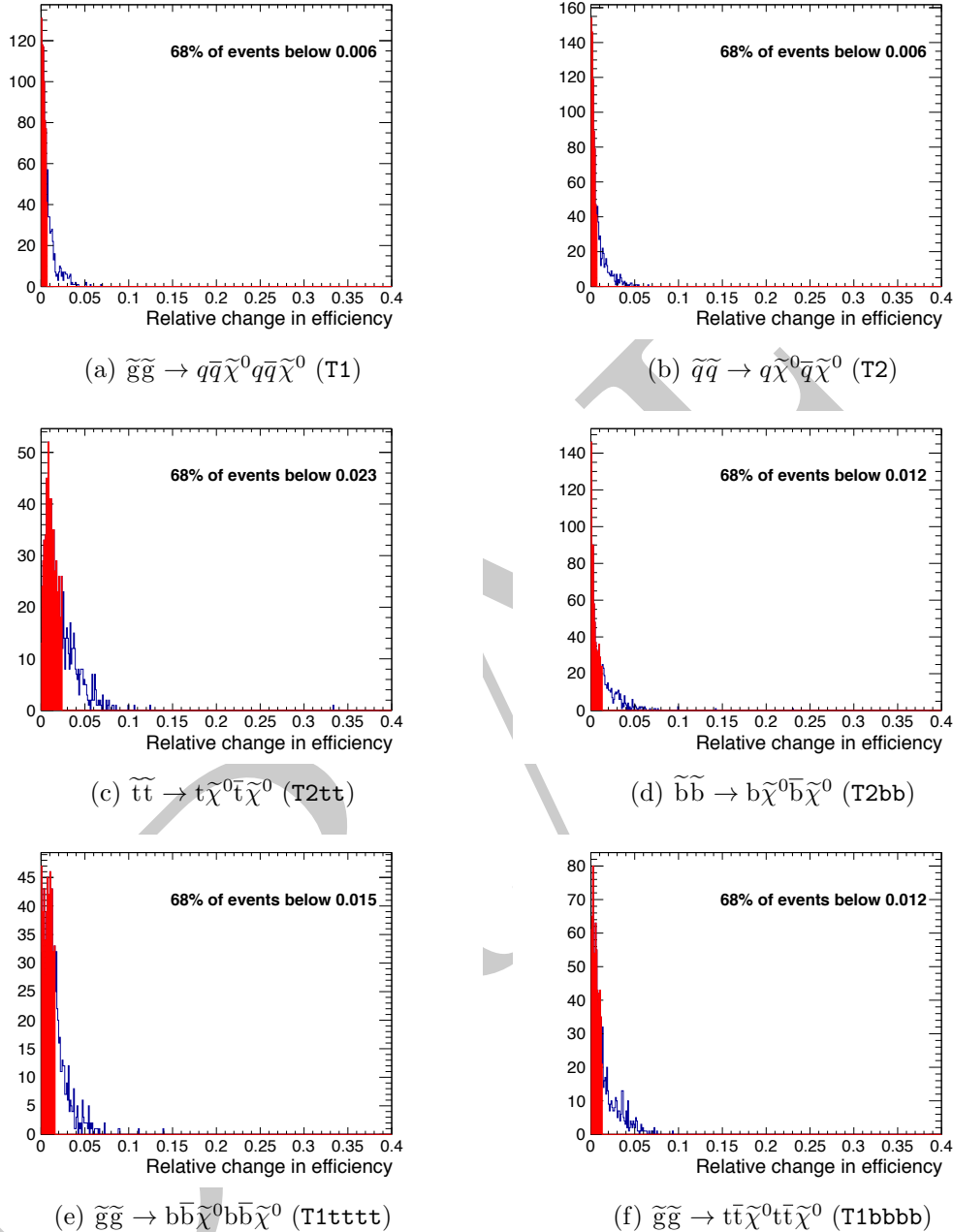
**Figure 20:** The fractional change in signal efficiency due to systematically increasing all jet energies, for various topologies. No requirement is made on the number of reconstructed b jets.



**Figure 21:** The fractional change in signal efficiency due to systematically decreasing all jet energies, for various topologies. No requirement is made on the number of reconstructed b jets.

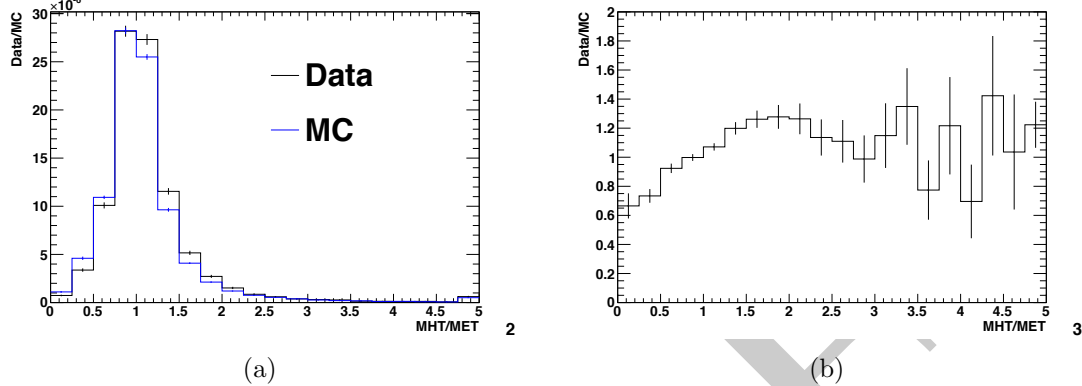


**Figure 22:** The fractional change in signal efficiency near to the diagonal due to systematically increasing or decreasing all jet energies, for various topologies. No requirement is made on the number of reconstructed b jets.

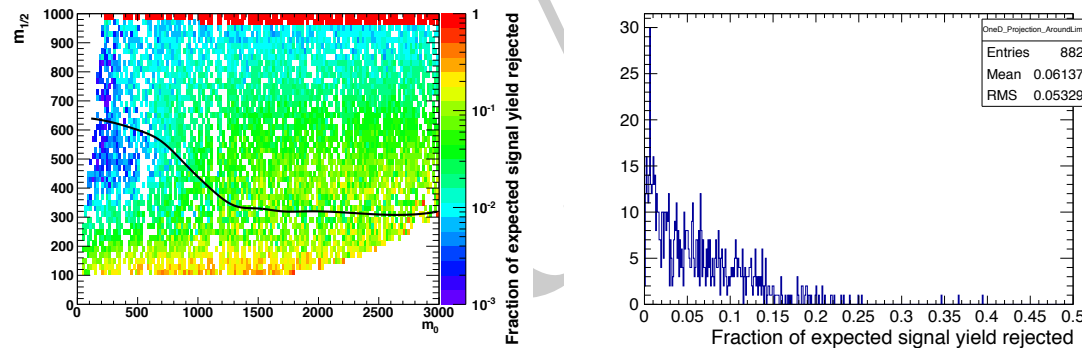


**Figure 23:** The fractional change in signal efficiency far from the diagonal due to systematically increasing or decreasing all jet energies, for various topologies. No requirement is made on the number of reconstructed b jets.

## 5.2 Systematics due to the MHT/MET cut



**Figure 24:** (a) Comparison of the MHT/MET distributions from data and MC, and (b) the ratio of the distributions, data/MC, as a function of the MHT/MET cut value.

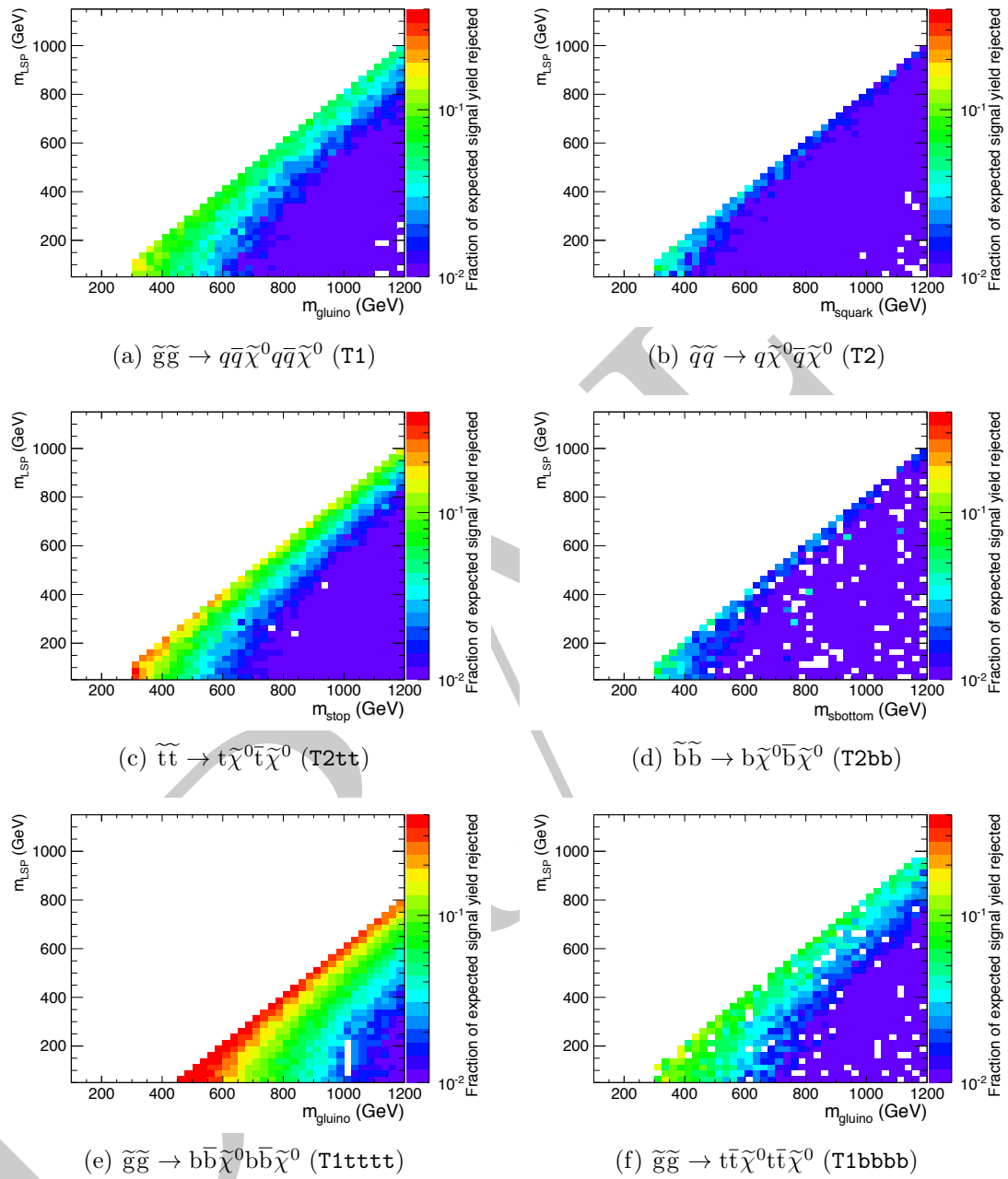


(a) Fraction of expected signal yield rejected. (b) Fraction of expected signal yield rejected in a  $\pm 60$  GeV band around the observed limit.

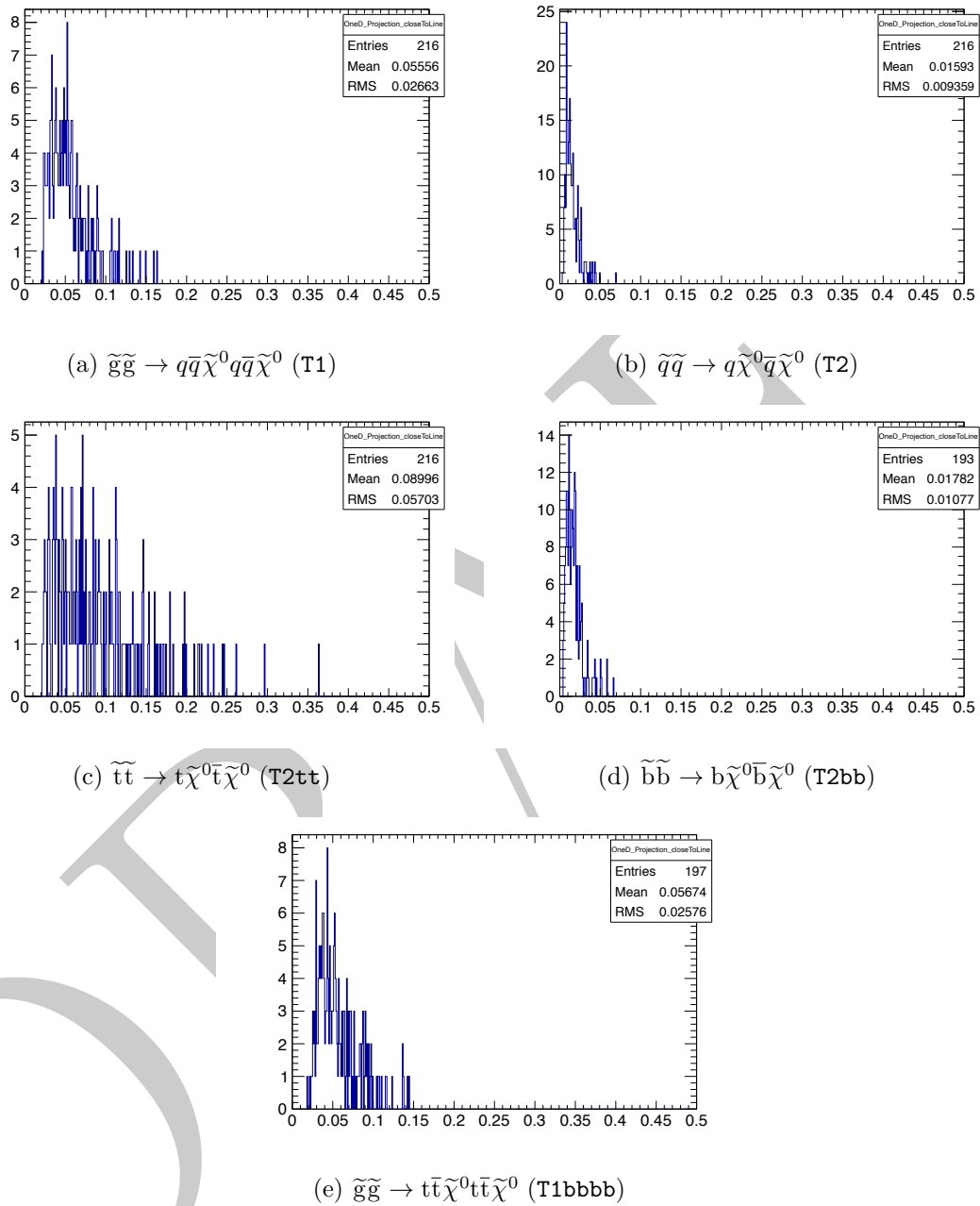
**Figure 25:** The fraction of expected signal yield that is rejected by the MHT/MET cut in the CMSSM plane. No requirement is made on the number of reconstructed b jets.

**Table 5:** Conservative estimates of inefficiency (%) for the MHT/MET cut when considering model points in the region near to the diagonal (i.e. small mass splitting and compressed spectra) for various simplified models.

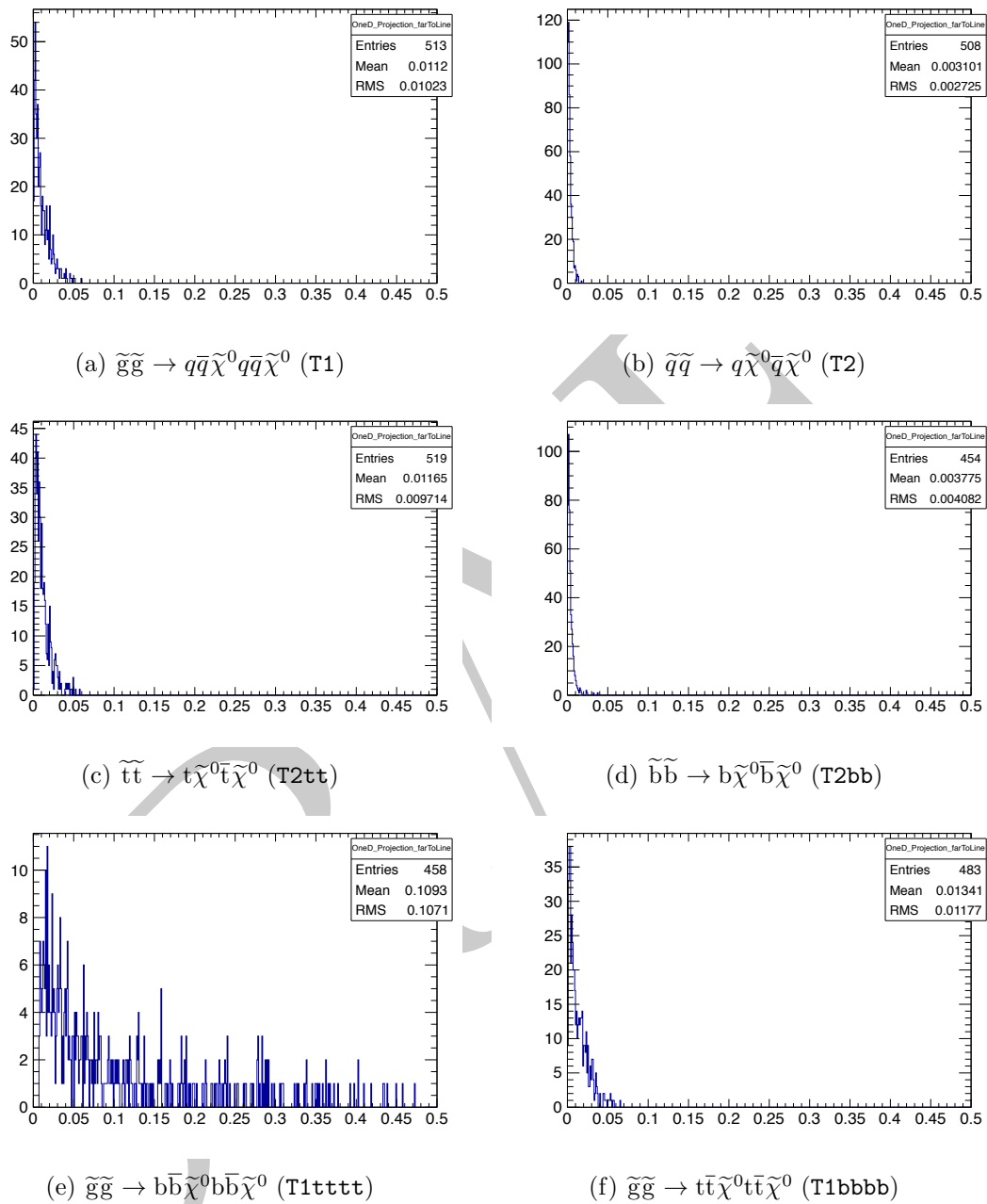
	T1	T2	T2tt	T2bb	T1tttt	T1bbbb
Near	10.9	3.5	20.4	3.9	-	10.8
Far	3.2	0.9	3.1	1.2	32.4	3.7



**Figure 26:** The fraction of expected signal yield that is rejected by the MHT/MET cleaning cut, for various topologies. No requirement is made on the number of reconstructed b jets.

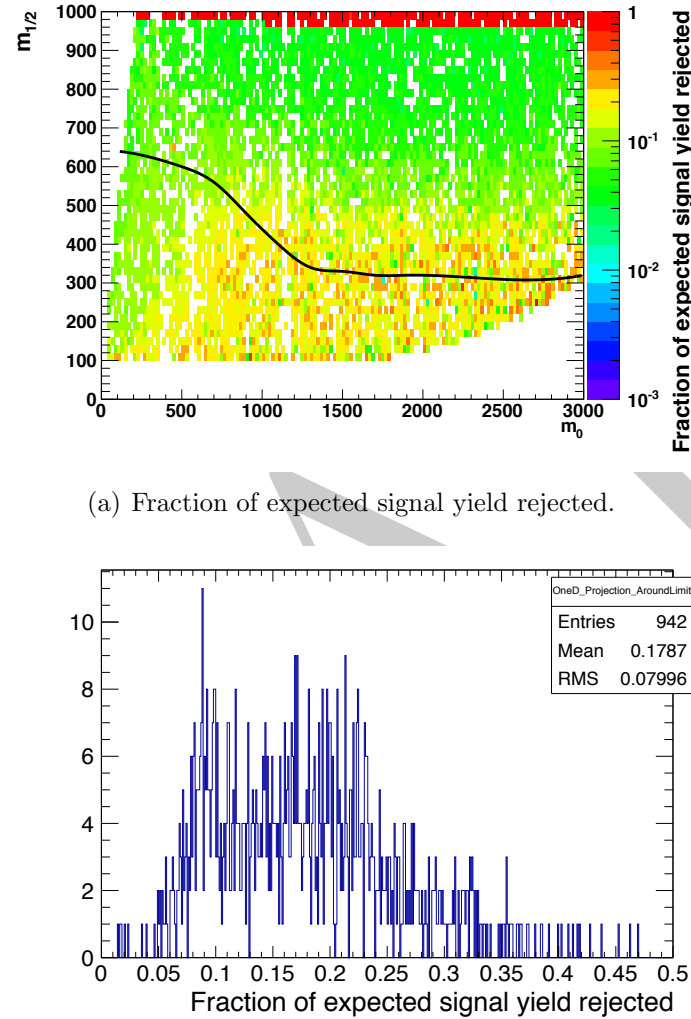


**Figure 27:** The fraction of expected signal yield that is rejected by the MHT/MET cleaning cut, near to the diagonal, for various topologies. No requirement is made on the number of reconstructed b jets.



**Figure 28:** The fraction of expected signal yield that is rejected by the MHT/MET cleaning cut, far from the diagonal, for various topologies. No requirement is made on the number of reconstructed b jets.

### <sup>1</sup> 5.3 Systematics due to the dead ECAL cut

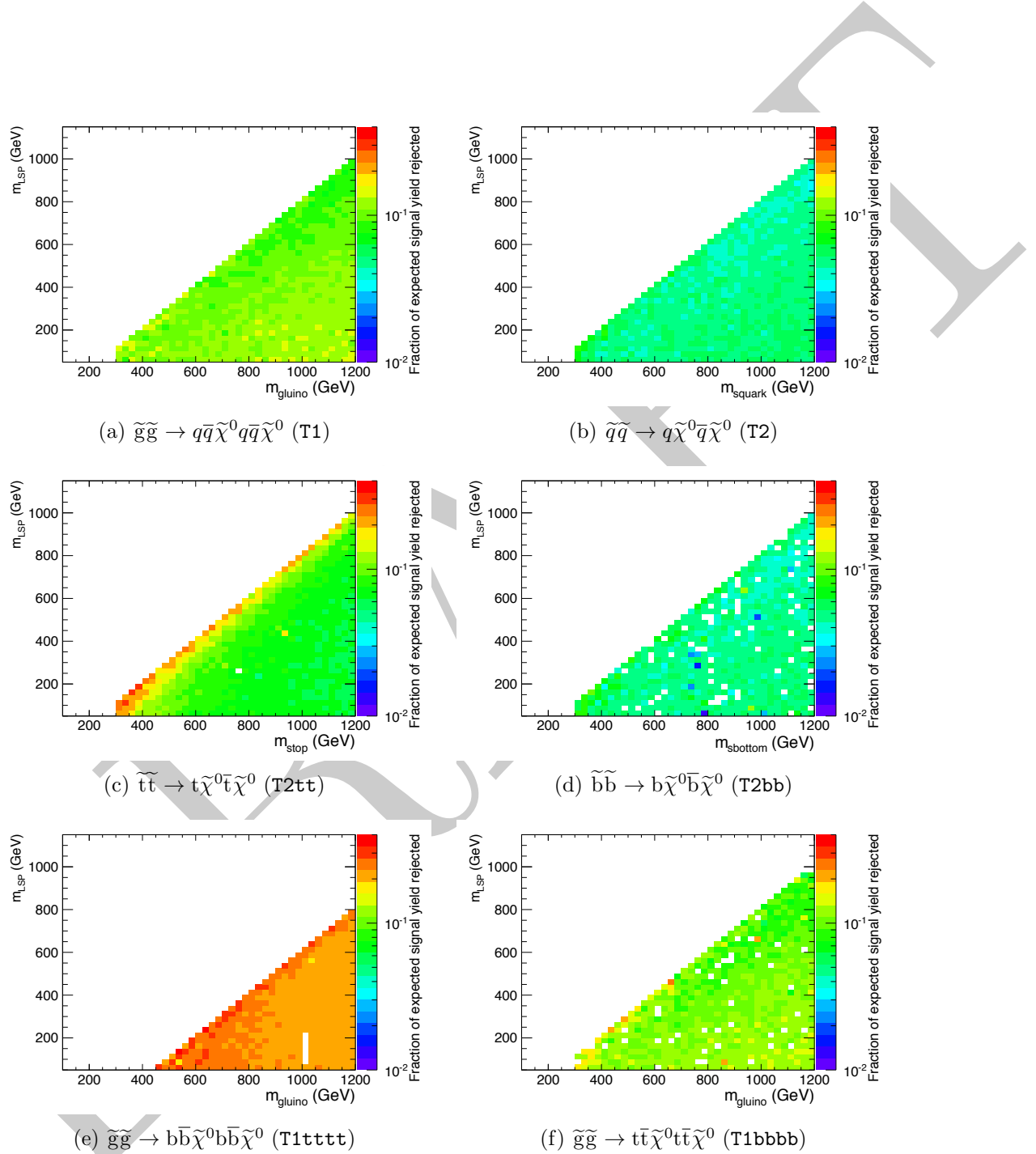


**Figure 29:** The fraction of expected signal yield that is rejected by the dead ECAL cut in the CMSSM plane. No requirement is made on the number of reconstructed b jets.

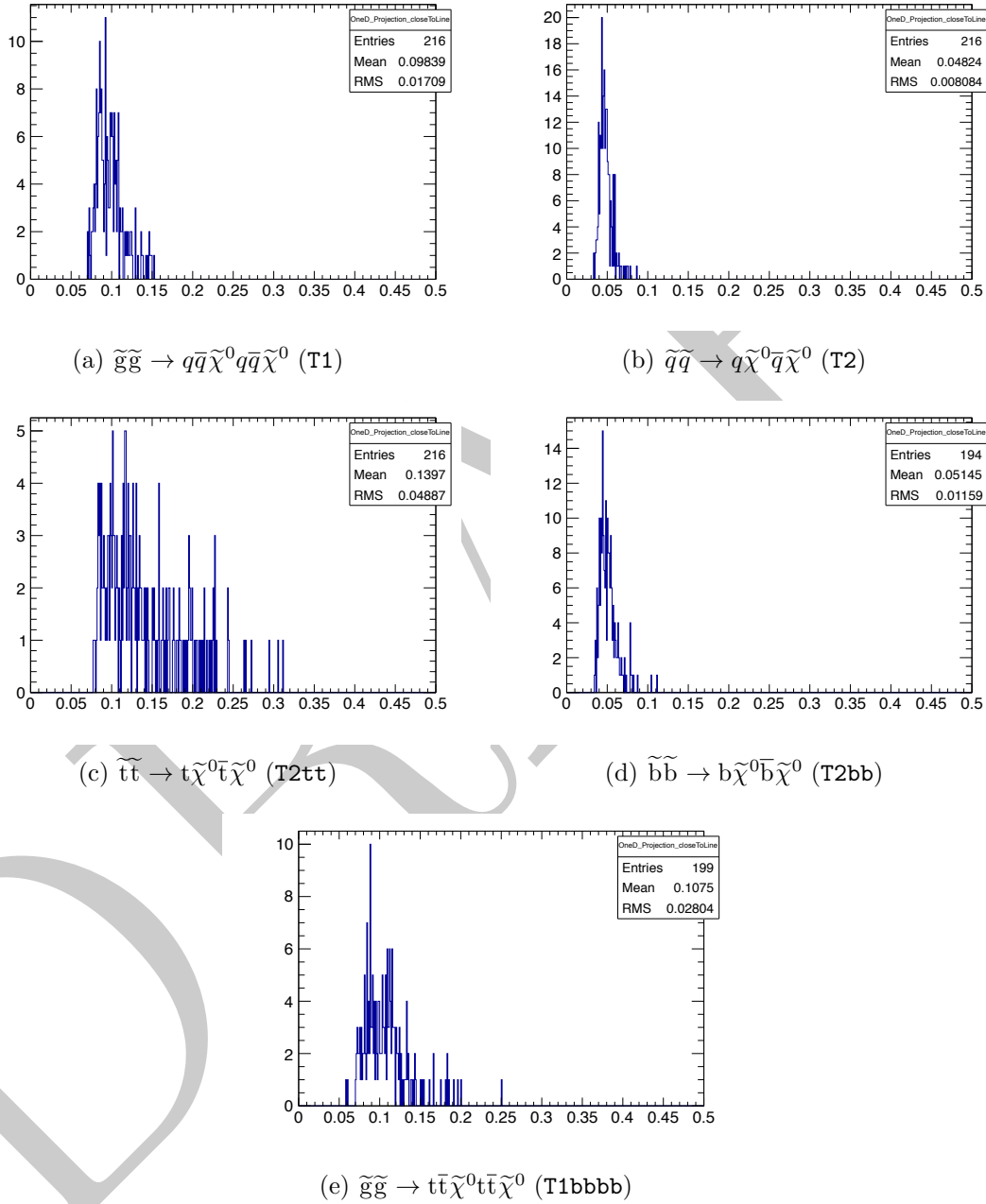
**Table 6:** Conservative estimates of inefficiency (%) for the dead ECAL cut when considering model points in the region near to the diagonal (i.e. small mass splitting and compressed spectra) for various simplified models.

	T1	T2	T2tt	T2bb	T1tttt	T1bbbb
Near	13.3	6.4	23.7	7.5	-	16.4
Far	13.6	5.8	9.4	6.2	27.6	13.9

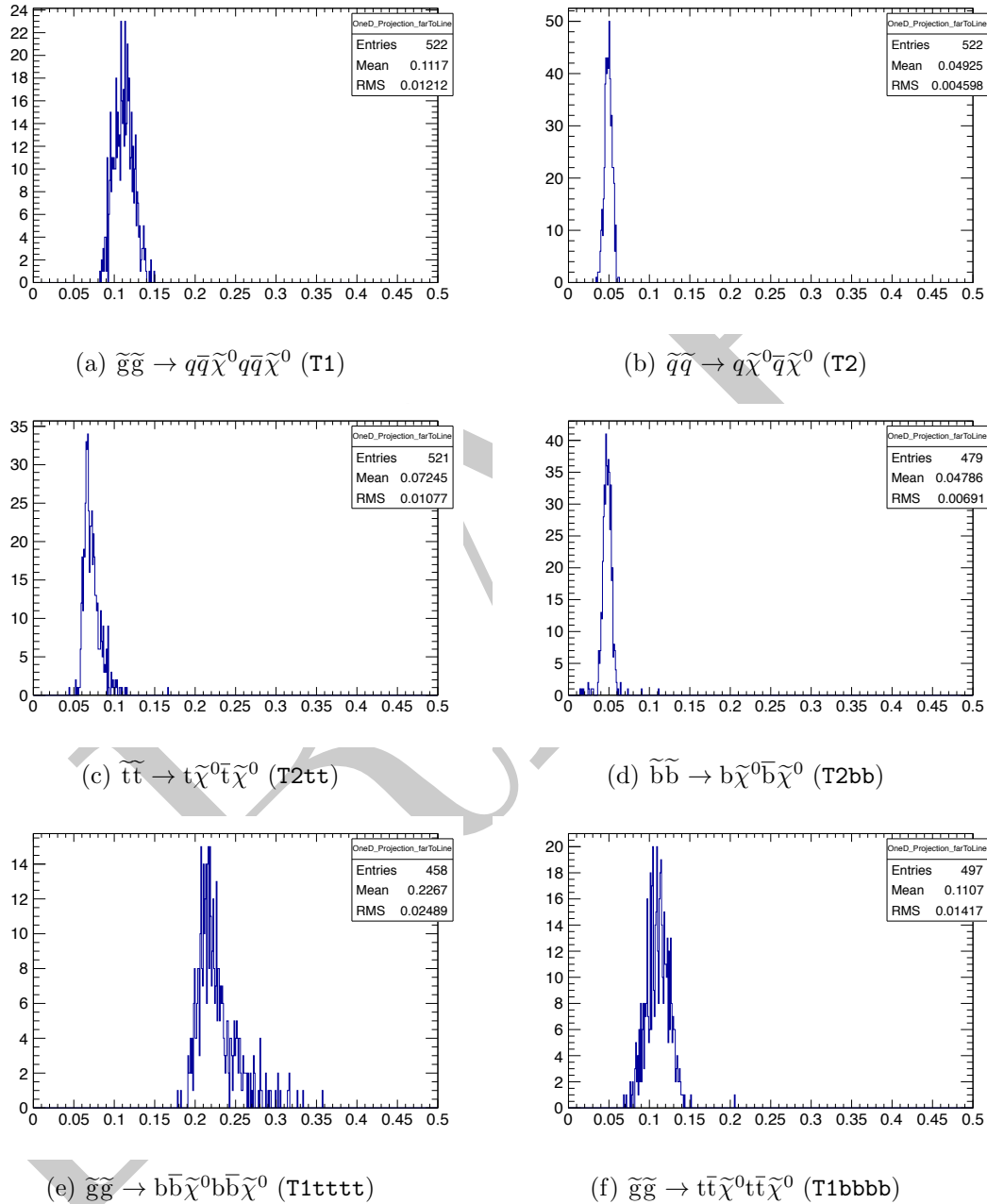
## 5.4 Systematics due to the lepton and photon vetoes



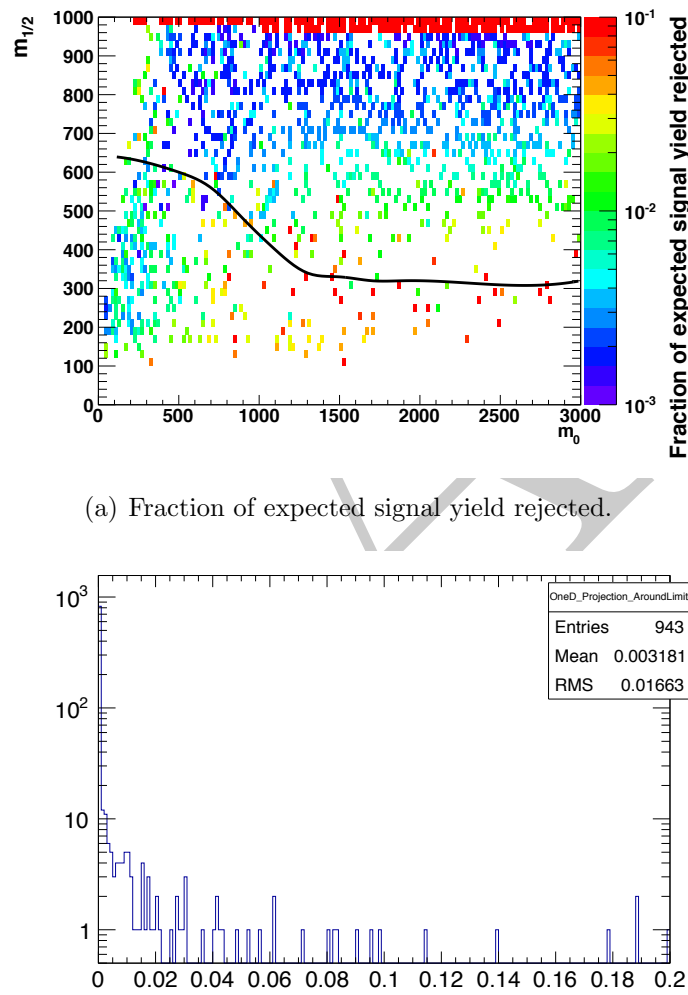
**Figure 30:** The fraction of expected signal yield that is rejected by the dead ECAL cleaning cut, for various topologies. No requirement is made on the number of reconstructed b jets.



**Figure 31:** The fraction of expected signal yield that is rejected by the dead ECAL cleaning cut, near to the diagonal, for various topologies. No requirement is made on the number of reconstructed b jets.

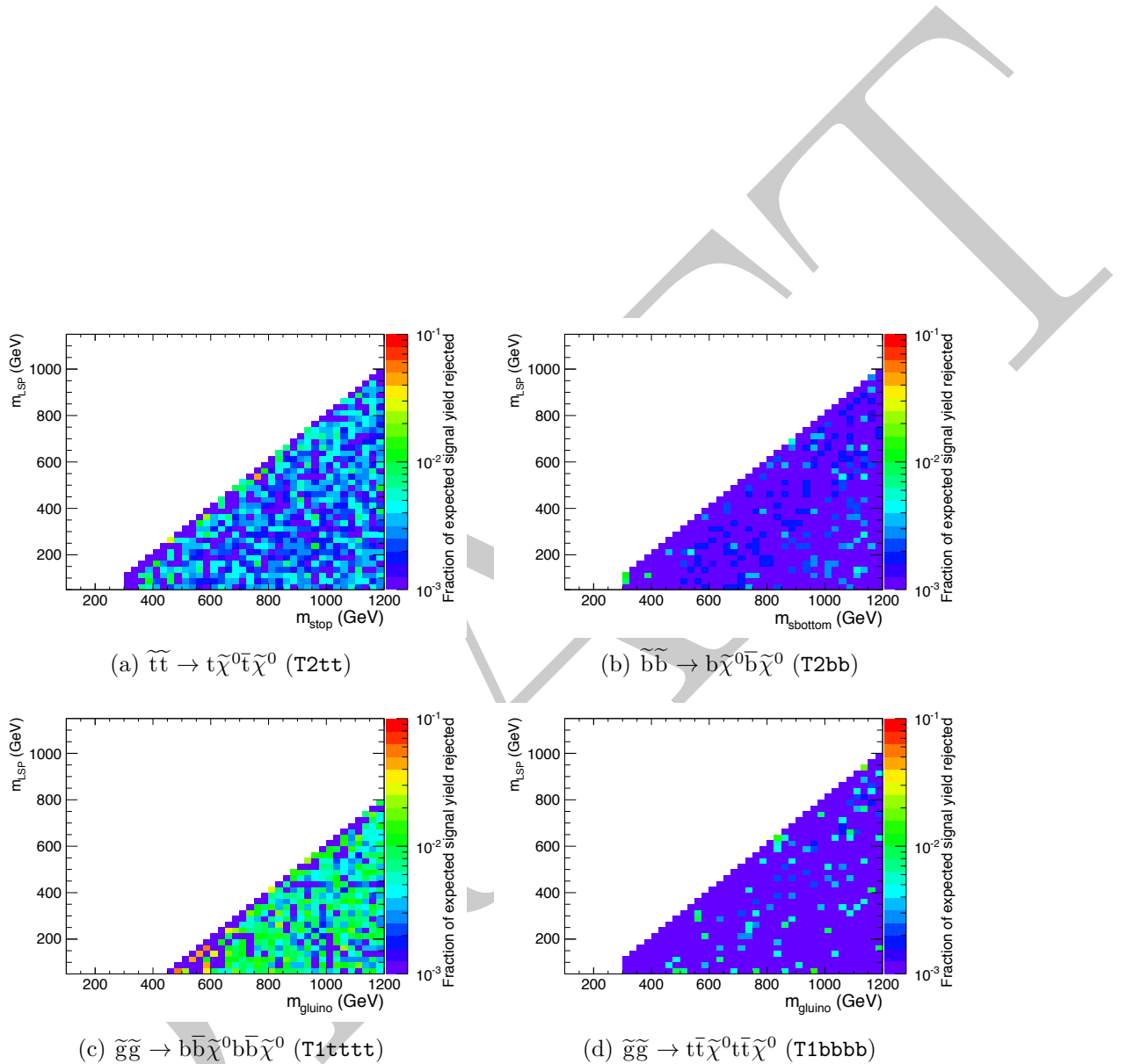


**Figure 32:** The fraction of expected signal yield that is rejected by the dead ECAL cleaning cut, far from the diagonal, for various topologies. No requirement is made on the number of reconstructed b jets.

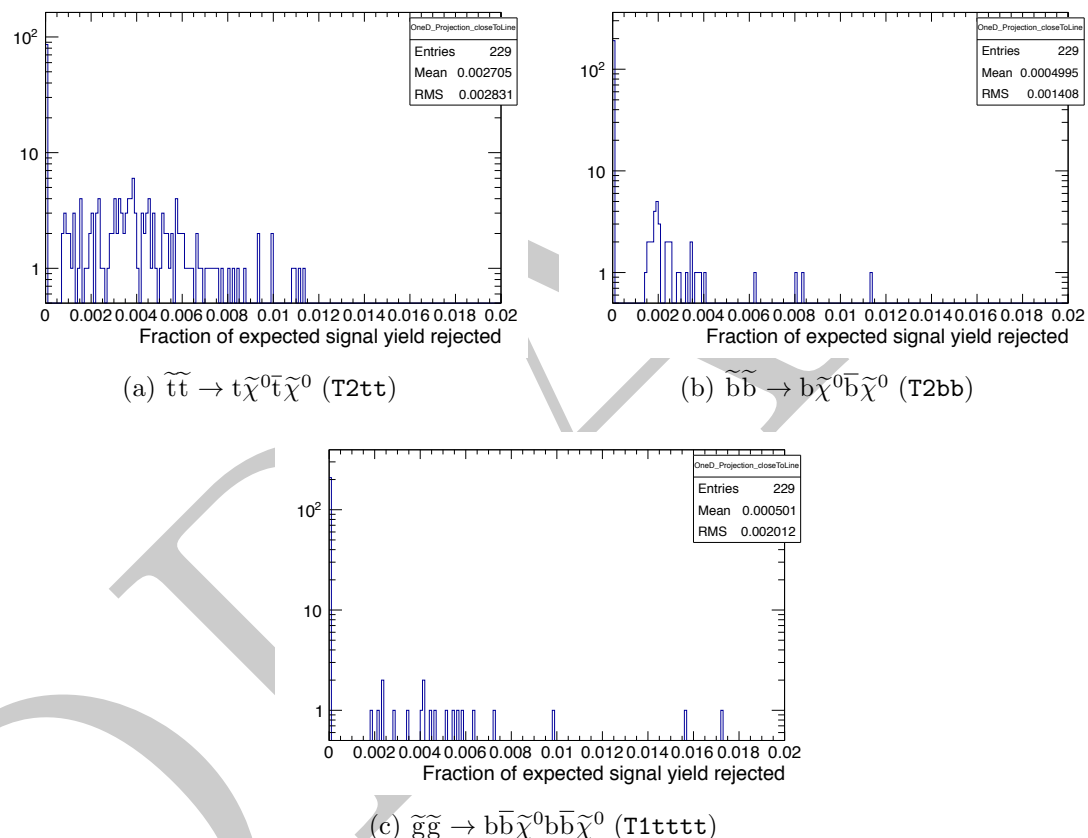


(b) Fraction of expected signal yield rejected in a  $\pm 60$  GeV band around the observed limit.

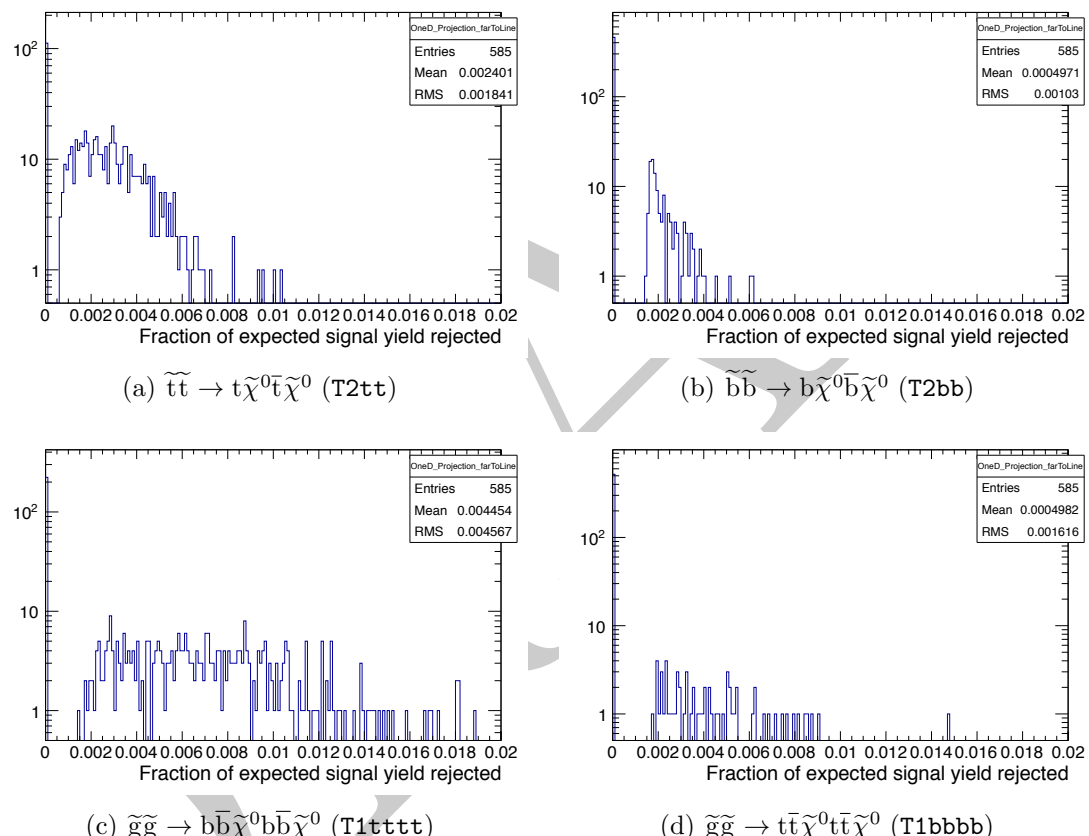
**Figure 33:** The fraction of expected signal yield that is rejected by the dead ECAL cut in the CMSSM plane. No requirement is made on the number of reconstructed b jets.



**Figure 34:** The fraction of expected signal yield that is rejected by the lepton and photon vetoes, for various topologies. No requirement is made on the number of reconstructed b jets.



**Figure 35:** The fraction of expected signal yield that is rejected by the lepton and photon vetoes, near to the diagonal, for various topologies. No requirement is made on the number of reconstructed b jets.



**Figure 36:** The fraction of expected signal yield that is rejected by the lepton and photon vetoes, far from the diagonal, for various topologies. No requirement is made on the number of reconstructed b jets.